NORTHWESTERN UNIVERSITY

Accelerated Cardiovascular MRI using Compressed Sensing and Artificial Intelligence

A DISSERTATION

SUBMITTED TO THE GRADUATE SCHOOL
IN PARTIAL FULFILLMENT OF THE REQUIREMENTS

for the degree

DOCTOR OF PHILOSOPHY

Field of Biomedical Engineering

By

Daming Shen

EVANSTON, ILLINOIS

June, 2021

Abstract

Cardiovascular disease is the leading cause of death in US and non-invasive cardiac imaging has vital importance for early detection and diagnosis of heart disease. Cardiac Magnetic Resonance (CMR) is arguably the most versatile imaging modality and capable of a comprehensive evaluation of heart disease without ionization radiation. Despite the advantages of CMR, it is seldom used (only 1% footprint) due to lack of availability and higher cost, which is mainly caused by the long scan times. Meanwhile, many accelerated CMR acquisition and quantification methods were feasible, but their clinical translation was limited due to long image reconstruction time and long manual processing time (e.g. segmentation). The purpose of this dissertation was to describe the development and validation of accelerated CMR methods using compressed sensing (CS) and deep learning (DL) to overcome current limitations. This dissertation includes the following topics: (i) CS image reconstruction of accelerated coronary quiescent-interval slice-selective (QISS) magnetic resonance angiography (MRA) that enabled single-shot, free-breathing acquisition, (ii) a newly developed high-resolution late gadolinium enhancement (LGE) CMR sequence with novel CS image reconstruction that provides multi-TI image contrast, (iii) rapid image reconstruction of highly undersampled real-time cine using deep learning without significant loss in image quality, visual scores and functional parameters, (iv) automated image segmentation of biventricular tissue phase mapping (TPM) using deep learning.

Acknowledgment

First and foremost, I want to acknowledge my family. My father Bin and mother Lijun, who constantly supported me during my PhD studies. I want to acknowledge my PhD mentor Dr. Kim for his invaluable help, support, and patience in training me to become an effective researcher in the field of Cardiac MRI. He's not only a great mentor that helped me progress in my research, but also a great friend that gave me valuable advice for my future success. I want to also acknowledge my other committee members, Dr. Markl, Dr. Lee, and Dr. Carr. The work presented in this dissertation would not have been possible without each of their support and guidance. I want to also acknowledge my lab mates and co-workers, from whom I learned a lot and got many supports. In addition, this work could not have been completed without the help of the clinicians and technologists at Northwestern who have been very accommodating to include my research. Finally, I want to acknowledge Northwestern Medicine's Radiology Department and Northwestern Biomedical Engineering Department for their critical support, both provided me with world class education and research infrastructures that allows me to fully pursue my passion of developing exciting and cutting-edge technology for the improvement of patient care.

List of Acronyms

ANN: Artificial neural network

A.U.: Arbitrary Units

B-SSFP: Balanced steady-state free precession

BM3D: Block match filtering

CAD: Coronary artery disease

CE-MRA: Contrast-enhanced magnetic resonance angiography

CHD: Congenital heart disease

CKD: Chronic kidney disease

CMR: Cardiac magnetic resonance

CNN: Convolutional neural network

CNR: Contrast to noise ratio

CS: Compressed sensing

CT: Computed tomography

CTA: CT angiography

CV: coefficient of variation

DL: Deep learning

DICOM: Digital Imaging and Communications in Medicine

ECHO: Echocardiography

EDV: End-diastolic volume

EF: Ejection fraction

EMB: Endomyocardial Biopsy

ESV: End systolic volume

FOV: Field-of-view

FID: Free induction decay

GBCA: Gadolinium-based contrast agent

GA: General anesthesia

GAN: Generative Adversarial Network

GPU: graphic processing unit

GRAPPA: Generalized auto-calibrating partially paralleled acquisitions

GRASP: Golden-angle radial sparse parallel MRI

GRE: Gradient echo

HIPAA: Health Insurance Portability and Accountability Act

HTx: Heart Transplantation

ICC: Intra-class correlation coefficient

IO: Independent Observer

LGE: Late gadolinium enhanced

LOA: limits of agreement

LV: Left ventricular

LVEDV: left ventricular end-diastolic volume

LVEF: left ventricular ejection fraction

LVESV: left ventricular end-systolic volume

LVSV: left ventricular stroke volume

MI: Myocardial infarction

MIP: Maximum-intensity-projection

MRA: Magnetic resonance angiography

MRI: Magnetic resonance imaging

MSE: mean squared error

NC-MRA: Non-contrast magnetic resonance angiography

NRMSE: Normalized root mean square error

NUFFT: Non-uniform Fourier transform

PCNN: Perceptual complex neural network

PET: Positron emission tomography

PSF: Point spread functions

QISS: Quiescent-interval slice-selective

R: Acceleration factor

RF: Radio-frequency

ReLU: rectified linear unit

RING: Radial Intersections

SENSE: Sensitivity encoding

SNR: Signal-to-noise ratio

SPECT: Single-photon emission computed tomography

SV: Stroke volume

SVS: Summed visual scores

SSIM: structural similarity index

TGA: Tiny golden angle

TPM: Tissue phase mapping

VGG: Visual Geometry Group

Table of Contents

List of Figures

List of Tables

Chapter 1: Introduction

1.1) Overview

Cardiovascular disease is the leading cause of death in US and non-invasive cardiac imaging has vital importance for early detection and diagnosis of heart disease. Cardiac Magnetic Resonance (CMR) is arguably the most versatile imaging modality and capable of a comprehensive evaluation of heart disease without ionization radiation. Despite the advantages of CMR, it is seldom used (only 1% footprint) due to lack of availability and higher cost, which is mainly caused by the long scan times. Meanwhile, many accelerated CMR acquisition and quantification methods were feasible, but their clinical translation was limited due to: (i) long image reconstruction time and (ii) long manual processing time (e.g. segmentation). This thesis will focus on accelerating CMR imaging by developing and validating (i) image reconstruction of highly undersampled data using compressed sensing (CS), rapid image dealiasing using deep learning (DL) and automated CMR image segmentation using deep learning.

1.2) Non-invasive Cardiac Imaging

Cardiovascular disease is the leading cause of death in US, killing over 655,000 people annually (1). Effective diagnosis and treatment of at-risk patients requires regular clinical monitoring to assess cardiac anatomy and function using non-invasive imaging. Four major non-invasive imaging modalities available for cardiovascular assessment include: nuclear imaging (i.e. SPECT and PET), echocardiography (Echo), Computed Tomography (CT) and Magnetic Resonance Imaging (MRI).

1.2.1) Nuclear Imaging

In nuclear imaging, small amount of radioactive materials (i.e. radiotracers) are typically injected into the bloodstream, inhaled or swallowed. The radiotracer then travels through the area being examined and involves in the biological processes, during which the radioactive elements decay and emit photons. By detecting the photons that come out of patients' body using radiation detector, the biological processes in the targeted regions can be visualized (2, 3). Single photon emission computed tomography (SPECT) and positron emission tomography (PET) are two common clinical variants of nuclear imaging (2), both are commonly used for detecting myocardial viability after ischemic events (4, 5). While SPECT and PET can provide diagnostic information with high sensitivity, the ionizing radiation and low spatial resolutions (i.e. 8-12 mm for SPECT and 6-8 mm for PET) are been concerned.

1.2.2) Echocardiography

Echocardiography (Echo) is the first line of imaging for assessment of heart disease as it is quick and low cost(6). In Echo, a probe called a transducer that generates and receives ultrasound is used. The sound waves move through the imaging medium and reflect back (i.e. echo) to the transducer, which is then converted into pictures(7). By leveraging the frequency changes in detected echoes resulting from Doppler Effect, it is able to quantify tissue and blood speed as well as observe myocardial wall and valve motions (8-10). However, echo suffers from several major drawbacks: limited field of view, user dependence, and difficulty in imaging complex geometries.

1.2.3) Computed Tomography

In Computed Tomography (CT), x-rays are transmitted from a source through an imaging volume and experience attenuation, and received by the detectors. The received x-ray will have

integrated attenuation from all materials in its path. By rotating the x-ray tube, the signals from different angles can be reconstructed using filtered back projection and characterize the spatial variation of the attenuation coefficients. CT provides high resolution 2D or 3D anatomical images and requires less operator expertise, while exposure to ionizing radiation and iodinated contrast agent cause additional risk (11) to patients with heart disease.

1.2.4) Cardiovascular Magnetic Resonance

In MRI, a strong magnetic field (1.5T or 3T in clinic) is used to produce net magnetic moments from protons (^{1}H) that align with the main magnetic field (B_0). The longitudinal (along with B_0 field) magnetization is tipped to the transverse (orthogonal to B_0 field) plane by RF-pulse. The main concept of MRI is to generate, manipulate, and detect the transverse magnetization in the tissues of interest by encoding spatial information and then reconstructing images through Fourier transformation of the detected signals.

CMR is arguably the most versatile imaging modality and capable of a comprehensive evaluation of heart disease, both qualitatively (detect vascular obstructions, myocardial infarction) and quantitatively (measure ejection fraction, scar volume and flow etc.), while not requiring ionizing radiation. Despite the advantages of CMR, it is seldom used (only 1% footprint) due to lack of availability and higher cost(12), which is mainly caused by long processing time (i.e. scan time and image post-processing time). Previous studies(13-17) have addressed that rapid CMR sequences with compressed sensing (CS) (15-18) are able to highly accelerate data acquisition (i.e. shorten scan times) with comparable image quality with clinical standard sequences, while the trade-off is long image reconstruction time that limits its clinic translation.

1.3) Specific Aims

The purpose of this dissertation was to describe the development and validation of acceleration methods designed to increase CMR utilization in clinic and the clinical translation of advanced CMR acquisition/quantification methods by addressing current limitations (i.e. long scan time, long reconstruction time and long quantification time). In particular, this dissertation was focused on: (i) compressed sensing image reconstruction of highly undersampled data without compromising image quality; (ii) rapid de-aliasing of highly undersampled CMR images using deep learning; (iii) automated CMR image segmentation using deep learning. Upon development, these methods were validated in patients with cardiovascular disease and compared with clinical standard methods.

1.4) Organization of the Dissertation

This dissertation is organized into 8 chapters. Chapter 1 provides an overview of cardiac imaging and the clinical justification for the importance of accelerated CMR research presented in this dissertation. Chapter 2 provides the requisite background on MR spin physics and image formulation for understanding the rest of this dissertation, especially, understanding how MR signals are acquired and why MR acquisition is slow. Chapter 3 introduces MR signal sampling methods and acceleration techniques for data acquisition and image reconstruction, specifically, compressed sensing and deep learning, which are used throughout Chapter 4 to Chapter 7. Chapter 4 describes the implementation of compressed sensing to single-shot coronary QISS MRA, which enables single-shot, free-breathing acquisition without losing image quality. Chapter 5 describes the development of multi-TI LGE CMR with compressed sensing. Unlike conventional 2D LGE,

multi-TI LGE provides time-resolved images by explores the sparsity in the time dimension. Chapter 6 describes the application of deep learning in image reconstruction of real-time cine images. A perceptual complex neural network is developed and compared quantitatively with three other networks. CS reconstruction was used as the ground truth for DL training. Chapter 7 describes the implementation of image segmentation with deep learning for myocardial tissue phase mapping. Magnitude plus three dimensional tissue velocity images were used as input and multi-layer masks as reference. Chapter 8 summarizes this dissertation and provides suggestions on future directions.

Chapter 2: Background on MRI

2.1) Overview

Magnetic resonance imaging (MRI) is a non-invasive imaging modality that is commonly used in clinical radiology. It is based on nuclear magnetic resonance (NMR) of nuclei (i.e. ^{1}H proton) in a strong magnetic field. The rotation of nuclei generates magnetic moments that can interact with magnetic fields. We obtain images with various contrast by manipulating and detecting these magnetization in the transverse plane. This chapter provides a brief introduction on the physics and math background of magnetic resonance imaging for better understanding the rest of the dissertation.

2.2) Nuclear Magnetic Resonance

2.2.1) Nuclear Spin

Nuclear induction was first described by Edward Purcell and Felix Bloch in 1946 (19, 20). Nuclei with non-zero spin quantum numbers (i.e. ^{1}H, ^{13}C, ^{19}F, and ^{19}P) have a magnetic dipole moment ($\vec{\boldsymbol{\mu}}$). We can imagine the nucleus as a charged particle with charge on its surface (Figure 2.1). When it rotates with an angular momentum ($\vec{\boldsymbol{J}}$), it generates a magnetic moment ($\vec{\boldsymbol{\mu}}$) along its rotation axis. The relation between angular momentum ($\vec{\boldsymbol{J}}$) and the magnetic dipole moment ($\vec{\boldsymbol{\mu}}$) is expressed as equation 2.1, where γ is the gyromagnetic ratio that is specified by the nuclei ($\gamma/2\pi =$ 42.57 MHz/T for ^{1}H). For this dissertation, we will focus on proton (^{1}H) imaging, because it is the most abundant element in human body and most of the clinical MRI scanners are designed based for it.

$$\vec{\mu} = \gamma \cdot \vec{J} \qquad \textbf{Eq 2.1}$$

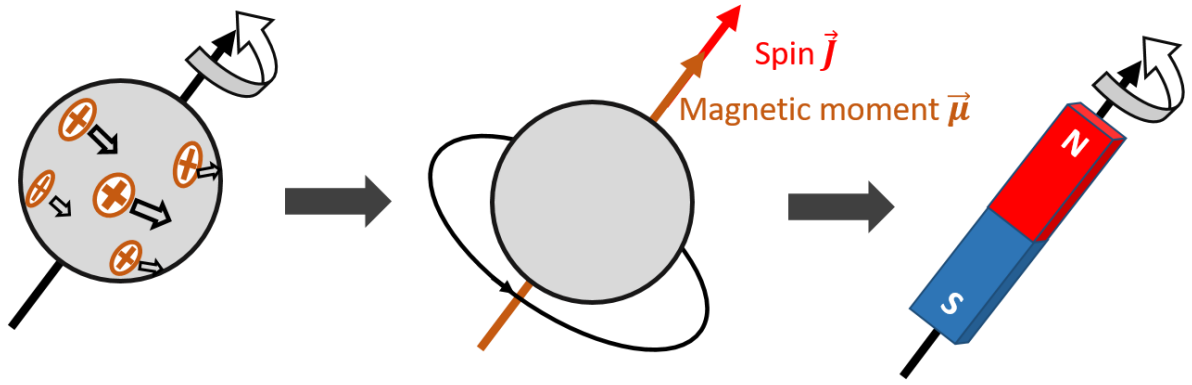

Figure 2.1. The nuclei can be taken as a rotating particle with charges on its surface. When it rotates with angular momentum ($\vec{J}$), it generates a magnetic moment ($\vec{\mu}$) along its rotation axis.

2.2.2) Bulk Magnetization

As shown in figure 2.2, ^{1}H spins are randomly oriented in earth's normal magnetic field due to thermal energy. The net magnetization ($\vec{M}$), which is a vector field representing comprehensive spins $\vec{M} = \sum \vec{\mu}$, is close to zero since the spins cancel out each other. Once the object is placed in a strong magnetic field ($\vec{B_0}$), the ^{1}H spins either orient parallel (↑) or anti-parallel (↓) to the main magnetic field. More spins will orient parallel to the main magnetic field because of the lower energy associated with parallel alignment as defined by equation 2.2, where $\hbar$ is Plank's constant h ($6.6 \times 10^{-34} J \cdot s$) divided by 2π. This in turn produces a net magnetic moment which can be manipulated to produce MR images. In the magnetic field, the spins precess at a resonance frequency (ω_0) known as the Larmor frequency (21, 22), which is defined by equation 2.3.

$$E_{\uparrow} = -\frac{1}{2}\gamma\hbar B_0 \ , \quad E_{\downarrow} = +\frac{1}{2}\gamma\hbar B_0 \qquad \textbf{Eq 2.2}$$

$$\omega_0 = \gamma B_0 \qquad \textbf{Eq 2.3}$$

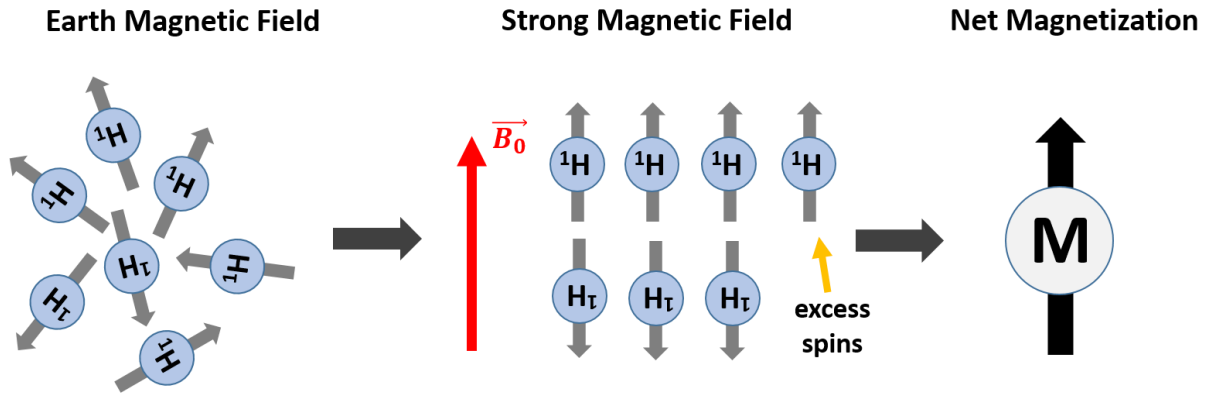

Figure 2.2. ^{1}H spins in the earth magnetic field are randomly oriented due to thermal energy. When they are put in a strong magnetic field ($\overrightarrow{B_0}$), spins either orient parallel or anti-parallel to the field. More spins will orient parallel to the main magnetic field because of the lower energy associated with parallel alignment. This in turn produces a net magnetic moment which can be manipulated to produce MR images.

2.2.3 Radio-Frequency Pulse

To measure the magnetization, it has to be tipped to the transverse plane using a radio-frequency (RF) pulse that generates a rotating RF field ($\overrightarrow{B_1}$). Its frequency is tuned to the resonance frequency of the ^{1}H spins (i.e. $\omega_{rf} = \omega_0$), where $B_1^e(t)$ is a pulse envelope function.

$$\overrightarrow{B_1} = B_1^e(t)e^{-i\omega_{rf}t} \qquad \textbf{Eq 2.4}$$

As shown in Figure 2.3, the magnetization rotates around the $\overrightarrow{B_{eff}}$ when $\overrightarrow{B_1}$ field is rotating at the same time and at the end of this process, the magnetization is tipped to the transverse plane. After that, the magnetization begins to recover back to its thermal equilibrium state, while

precessing at the Larmor frequency around $\overrightarrow{\boldsymbol{B_0}}$ field, which is called free-induction decay (FID). An RF coil is an antenna used for both generate RF pulse to stimulate spins and receiving/detecting MR signals from the excited spins. Particularly, based on Faraday's law of induction (i.e., electromagnetic induction), the recordable MR signals are generated mostly from the transverse magnetization relaxation (M_{xy}) of a FID.

In fact, an RF pulse can tip spins with a certain flip angle (α), which is between 0 to 180 degrees. The flip angle is determined by the duration (τ) and the magnitude of $\overrightarrow{\boldsymbol{B_1}}$:

$$\boldsymbol{\alpha = \int_0^{\tau} \gamma B_1^e(t) dt} \qquad \textbf{Eq 2.5}$$

Right after the RF excitation (t = 0), the longitudinal (M_z) and transversal magnetization (M_{xy}) is defined by equation 2.6:

$$\boldsymbol{M_z = M_0 cos\alpha\,, \qquad M_{xy} = M_0 sin\alpha} \qquad \textbf{Eq 2.6}$$

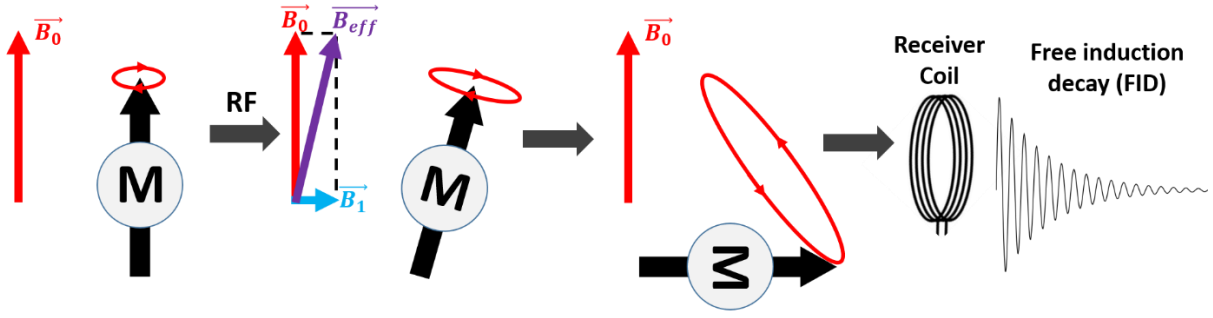

Figure 2.3. RF excitation process. A $\overrightarrow{\boldsymbol{B_1}}$ field is applied perpendicular to the main magnetic field and the magnetization rotates around the $\overrightarrow{\boldsymbol{B_{eff}}}$. At the end of this process, the magnetization is tipped to the transverse plane. It will recover back to its thermal equilibrium state, which is called free-induction decay (FID).

2.2.4) Relaxation

After each change in magnetization caused by an RF pulse, the spins return to their equilibrium state. This dynamic process is called relaxation, which can be described by two independent time constants – longitudinal relaxation time (T_1) and transverse relaxation time (T_2 and T_2^*).

Longitudinal relaxation time (T_1) is a time constant describing the recovery rate of longitudinal magnetization (M_z) back to thermal equilibrium state. This is caused by the energy exchange or dissipation between spins and their surroundings, so it is also called spin-lattice relaxation. Since T_1 is highly associated with the surrounding environment, tissues with different compositions have different T_1 values. The Bloch equation describes the longitudinal relaxation mechanism by equation 2.7. Where M_0 is the equilibrium magnetization and $M_z(0)$ is the longitudinal magnetization at time t=0, which is described by equation 2.6.

$$\frac{\boldsymbol{dM_z}}{\boldsymbol{dt}} = \frac{\boldsymbol{M_0 - M_z}}{\boldsymbol{T_1}}$$

$$\boldsymbol{M_z(t) = M_0\left(1 - e^{-\frac{t}{T_1}}\right) + M_z(0)e^{-\frac{t}{T_1}}} \qquad \textbf{Eq 2.7}$$

For example, if the flip angle α equals 90°, after one time constant T_1, M_z recovers to 63% of the thermal equilibrium state M_0.

Transverse relaxation time (T_2) is a time constant describing the decay rate of transverse magnetization (M_{xy}). This is caused by the spin-spin interactions, i.e. the nuclei or molecules have their own small magnetic fields that interact with each other. As spins are tipped to the transverse plane, they precess at different rate due to random spin-spin interactions, which causes the

dephasing of spins. The amplitude of transverse magnetization depends on the degree of coherence of the spins, which means it decreases as the spins dephase. Note that this T_2 decay effect is irreversible since the spin-spin interaction is random, it can't be reversed using a 180° pulse. The Bloch equation describes the transverse relaxation mechanism by equation 2.8.

$$\frac{dM_{xy}}{dt} = -\frac{M_{xy}}{T_2}$$

$$M_{xy}(t) = M_{xy}(0)e^{-\frac{t}{T_2}} \qquad \textbf{Eq 2.8}$$

After one time constant T_2, M_{xy} decays to 37% of initial state $M_{xy}(0)$. Both T_1 recovery and T_2 decay are intrinsic property of the spins, they are largely independent of the field strength B_0.

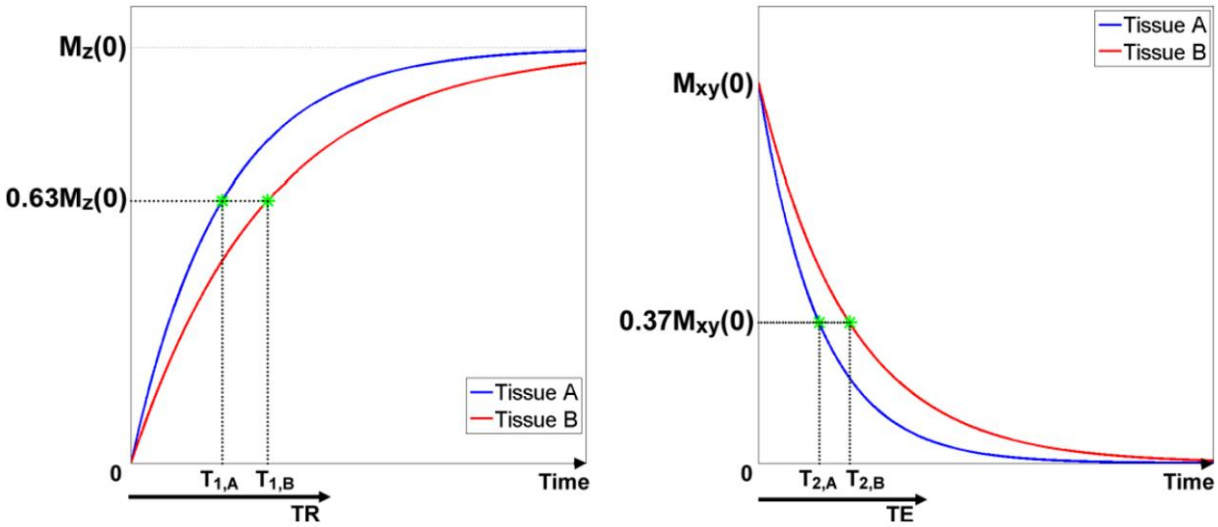

Figure 2.4. (Left) Longitudinal relaxation or T_1 recovery (90° RF case); (Right) transverse relaxation or T_2 decay. Blue and red curves represent two different tissues. TR: repetition time; TE: echo time.

In reality, due to magnetic field inhomogeneity and susceptibility effects, the transverse magnetization dephases faster than what described by T_2. The "true" transverse relaxation T_2^* is

affected by spin-spin interactions (T_2) and field inhomogeneity (T_2'), which is described by the following equation 2.9. Note T_2' can be reversed by a 180° pulse.

$$\frac{\mathbf{1}}{\boldsymbol{T_2^*}} = \frac{\mathbf{1}}{\boldsymbol{T_2}} + \frac{\mathbf{1}}{\boldsymbol{T_2'}} \qquad \textbf{Eq 2.9}$$

2.3) MR Imaging

Utilizing the fundamental properties of NMR phenomena, MR signals can be non-invasively detected from the inside of a living subject in a strong magnetic field. However, there is no localizing information in the main magnetic field, i.e. the detected MR signals have the same resonance frequency and we can't distinguish where the signals came from. Here we introduce slice selection, frequency encoding and phase encoding methods to localize the MR signals.

2.3.1) Slice Selection

To tip magnetization onto the transverse plane, the RF pulse must match the Larmor frequency of the spins. This can be utilized to only excite spins in the slice/volume of interest by slightly varying the magnetic field strength along z direction using a slice-selective gradient (G_z). Desired slice profiles are selected by using a slice-selective gradient to regionally alter the Larmor frequency of spins while simultaneously applying an excitation RF pulse with matching bandwidth. The slice thickness Δz is linearly proportional to the bandwidth (BW) of the RF-excitation pulse. The relationship between Larmor frequency and slice-selective gradient is described by equation 2.10, where $\omega_{Larmor}(z)$ is the Lamor frequency at positon z along the slice direction, and G_z is the slice-selective gradient.

$$\boldsymbol{\omega_{Larmor}(z) = \gamma(B_0 + G_z z)}$$

$$\boldsymbol{BW = \omega(z_1) - \omega(z_1) = \Delta\omega_{Larmor} = \gamma G_z \Delta z} \qquad \textbf{Eq 2.10}$$

2.3.2) Frequency and Phase Encoding

Frequency (G_x) and phase (G_y) encoding enable the localization of 2-dimensional (2D) information in the slice selected by the z-gradient. For 3D imaging, an additional partition encoding gradient (G_s) is required to control the Larmor frequency in the partition direction (z).The Larmor frequency for a given spatial position (x, y) in 2D and (x, y, z) in 3D is described by equation 2.11.

$$\boldsymbol{\omega_{Larmor}(x, y) = \gamma(B_0 + G_x x + G_y y)}$$

$$\boldsymbol{\omega_{Larmor}(x, y, z) = \gamma(B_0 + G_x x + G_y y + G_s z)} \qquad \textbf{Eq 2.11}$$

As shown in Figure 2.5, the main magnet generates main magnetic field (B_0), the gradient coils generate spatial encoding gradients and the RF coils are used to generate and receive MR signals.

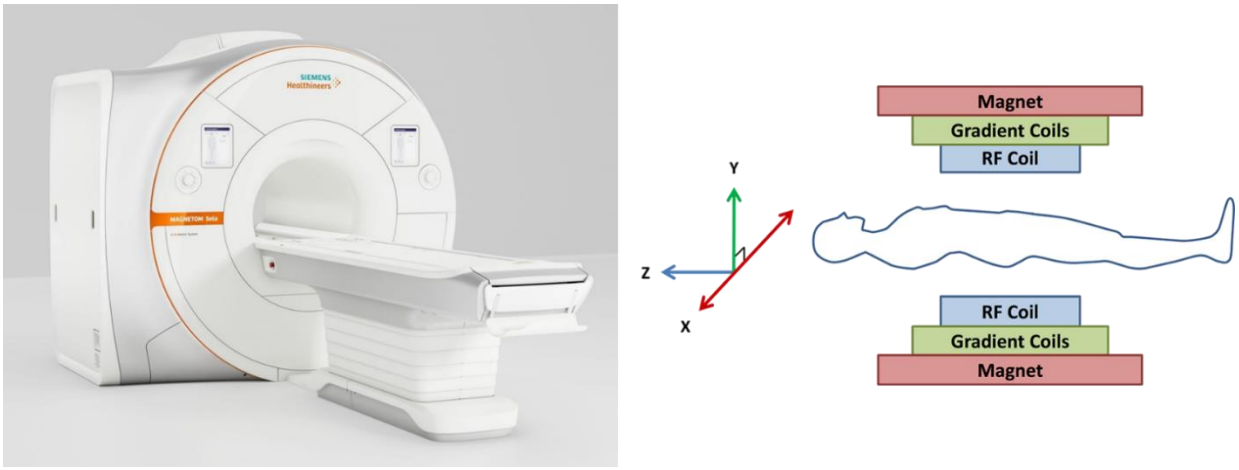

Figure 2.5. Simplified MRI system and location of coils.

2.3.3) K-space Formulation

With the principles introduced above, the transverse magnetization and its dependence on the spatial varying Larmor frequency can be described with equation 2.12 in 2D case.

$$\boldsymbol{M_{xy}(t) = M_{xy}(0) \cdot e^{-\frac{t}{T_2}} \cdot e^{i\int_0^t \omega_{Larmor}(x,y)d\tau}}$$

$$\boldsymbol{M_{xy}(t) = M_{xy}(0) \cdot e^{-\frac{t}{T_2}} \cdot e^{i\int_0^t \gamma(B_0+G_x x+G_y y)d\tau}} \qquad \textbf{Eq 2.12}$$

Substituting in:

$$\boldsymbol{k_x = \frac{\gamma}{2\pi}\int_0^t G_x(t)\,d\tau,\ k_y = \frac{\gamma}{2\pi}\int_0^t G_y(t)d\tau,\ \omega_0 = \gamma B_0}$$

Yields:

$$\boldsymbol{M_{xy}(t) = M_{xy}(0) \cdot e^{-\frac{t}{T_2}} \cdot e^{i\omega_0 t} \cdot e^{i2\pi(k_x x + k_y y)}} \qquad \textbf{Eq 2.13}$$

When the receiver coils acquire the data in frequency domain, the signal $\boldsymbol{S(t)}$ is proportional to the spatial summation of the transverse magnetization (Equation 2.14).

$$S(t) = c \cdot e^{i\omega_0 t} \iint_{-\infty}^{\infty} M_0(x,y) \cdot e^{\frac{-t}{T_2}} \cdot e^{i2\pi(k_x x + k_y y)}\, dxdy \qquad \textbf{Eq 2.14}$$

This indicates the MR signal we measured in k-space $S(k_x, k_y)$, and the underlying image $M_0(x,y) \cdot e^{\frac{-t}{T_2}}$ (denote as $I(x,y)$) are Fourier Transform pair. In other words, the inverse Fourier transform of $S(k_x, k_y)$ yields the image $I(x,y)$ encoded by the MRI pulse sequence.

2.3.4) Imaging Parameters

The connection between k-space and image space can be further explored for creating the optimal MR images. MR image characteristics such as field-of-view (FOV), image spatial resolution, the readout bandwidth, and image SNR are controlled by the gradient amplitudes, gradient durations, and the total number lines acquired.

The relationship between imaging FOV and sampling rate is described in equation 2.15, where Δk_x is the distance between sampling points in k-space along x direction.

$$FOV_x = \frac{1}{\Delta k_x} \qquad \textbf{Eq 2.15}$$

Equation 2.16 describes the spatial resolution of an acquired MR image, where N_{read} is the number of readout points along x direction and $\Delta\tau_x$ is the time duration for each readout sample.

$$\Delta x = \frac{FOV_x}{N_{read}} = \frac{1}{N_{read} \cdot \Delta k_x} = \frac{1}{2k_{x,max}} = \frac{1}{\frac{\gamma}{2\pi} G_x \tau_x} \qquad \textbf{Eq 2.16}$$

The readout bandwidth (BW) is defined by the sampling rate for the ADC (equation 2.17).

$$BW_{read} = \frac{1}{\Delta\tau} = \frac{1}{\frac{\gamma}{2\pi} G_x FOV_x} \qquad \textbf{Eq 2.17}$$

Finally, the image signal-to-noise ratio (SNR) represents the ability for the true signal of the MR image to be displayed in comparison with the underlying noise. SNR is proportional to voxel size and inversely proportional to the bandwidth.

$$SNR \propto \Delta x \Delta y \Delta z \sqrt{\frac{1}{BW_{read}}} \quad \textbf{Eq 2.18}$$

2.4) Pulse Sequence

Pulse sequences are used to acquire images with desired image contrast by controlling the RF pulse, spatial encoding gradients, ADC and etc. Three common pulse sequence types in MRI are spin echo (Figure 2.6), gradient echo (GRE) (Figure 2.7A and B), and balanced steady-state free precession (b-SSFP) (Figure 2.7C).

2.4.1) Spin Echo

During spin-echo, a 90° excitation RF pulse is combined with 180° RF pulse to produce a detectible echo (Figure 2.6). The use of 180° RF refocusing of transverse magnetization makes spin echo sequences resistant to artifact due to inhomogeneity in the magnetic fields. As such, spin echo sequences are used for T_2 weighted imaging.

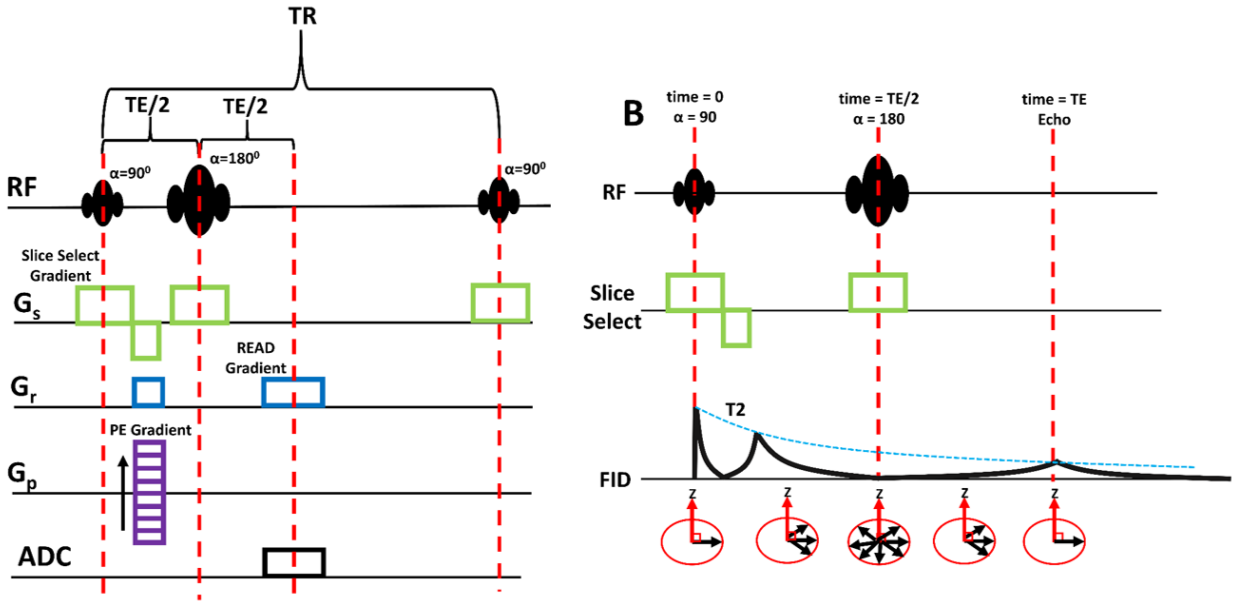

Figure 2.6. A) Pulse sequence diagram for spin echo acquisition. B) A 90° RF pulse excites spins onto transverse plane, while a subsequent 180° RF pulse produces a detectible echo by refocusing transverse magnetization dephasing due to inhomogeneity in magnetic field. Spin echo is inherently resistant to field inhomogeneity, making it an ideal tool for T_2 weighted imaging.

2.4.2) Gradient Echo

As shown in figure 2.7B, GRE sequences rely on pre-phasing gradient lobe for frequency encoding and inducing a detectible echo at TE. In GRE, transverse magnetization is spoiled after every TR using RF and/or gradient spoiling to prevent any residual transverse magnetization from undergoing additional RF excitations. Spoiled GRE with short TE and short TR are used for T_1 weighted imaging.

2.4.3) Balanced Steady-State Free Precession

The standard GRE sequence can be altered to produce b-SSFP imaging by balancing all gradient within every TR. Unlike spoiled gradient echo, b-SSFP does not utilize spoiler gradients,

but rather allows for transverse magnetization from previous RF excitations to undergo addition RF pulses to produce T_2/T_1 contrast. T_2/T_1 contrast is especially desirable in creating high contrast to noise ratio (CNR) for blood and myocardium. In b-SSFP imaging, TE and TR are minimized to reduce off-resonance, susceptibility, and inhomogeneity artifacts.

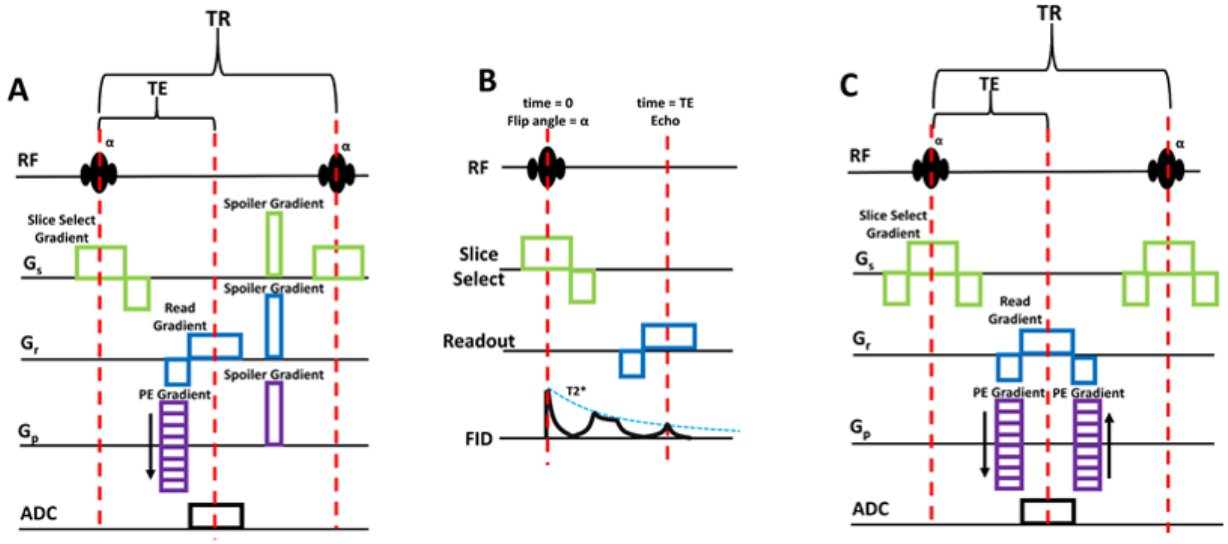

Figure 2.7. A) A pulse sequence diagram for GRE. Short TE and short TR spoiled GRE sequences are used for T_1 weighted imaging. B) Pre-phasing gradients are used to produce detectible echo, resulting in signal sensitivity to T_2^* transverse relaxation and inhomogeneity in the magnetic field. C) A pulse sequence diagram for a b-SSFP. B-SSFP imaging is a GRE acquisition for which all gradients are balanced within a TR resulting in T_2/T_1 contrast.

2.4.4) CMR Clinic Usage

GRE and b-SSFP are the most popular CMR clinical pulse sequences. The need for both an excitation and refocusing pulse in spin-echo makes these sequences undesirably slow for cardiac MR imaging, except for T_2 mapping in which edema is visualized (23). In contrast, the short TE and TR characteristic of GRE and b-SSFP have made these sequences the staple of CMR.

GRE is regularly used for cardiac viability, scar quantification, and hemodynamic assessment. B-SSFP is regularly used for cardiac function and angiographic assessment.

Chapter 3: Acceleration Techniques for CMR

3.1) Overview

From chapter 2, MR data acquisition is done in k-space and line-by-line. Each k-space line requires specific spatial encoding, which makes this technique relatively slow compared to other imaging modalities. For a single MR image, we are assuming the object is "frozen" during data acquisition (i.e. like taking a snapshot), otherwise, it will be subjected to motion artifacts. This fundamental assumption has made cardiac MR even more challenging than imaging other organs due to cardiac motion and respiratory motion. Therefore, one of the main areas of research to improve CMR is to accelerate the scan, thus reduce its cost and increase CMR utility. Significant amount of research has been done to overcome this limitation. This section will introduce several acceleration techniques such as radial k-space sampling, parallel imaging, compressed sensing, and deep learning.

3.2) K-space Sampling

Nyquist-Shannon sampling theorem states that to accurately measure a signal, the digital sampling rate must be greater than twice its maximum frequency contained within that signal (24). However, the data acquisition time will be too long to meet Nyquist with reasonable spatial resolution. If we want to accelerate data acquisition by undersampling the k-space, there will be aliasing artifacts related to sampling patterns, i.e. wrapping around artifacts with Cartesian sampling, streaking artifacts with radial sampling and rotating artifacts with spiral sampling (Figure 3.1). The main directions to overcome this is to: 1) design the sampling pattern wisely to

reduce the impact of undersampling aliasing artifacts; 2) use dealiasing methods to remove the aliasing and bring back the clean images.

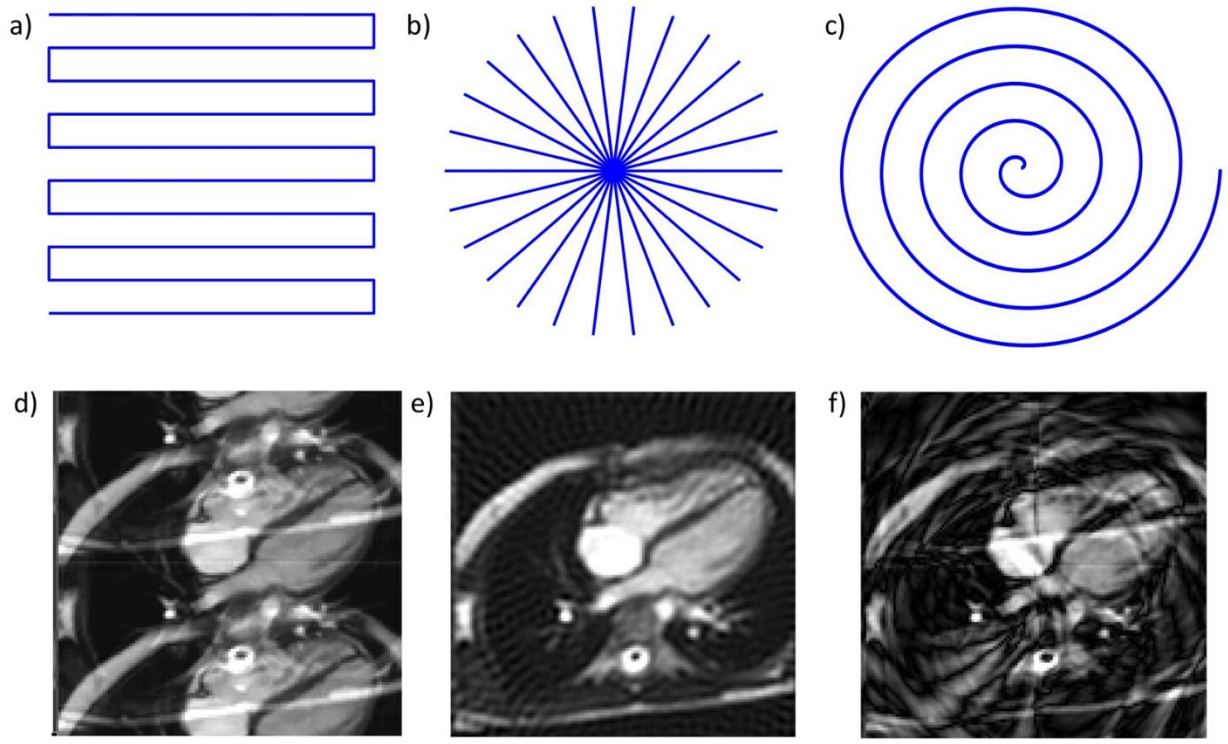

Figure 3.1. Undersampling aliasing artifacts. A), b) and c) are Cartesian, radial and spiral k-space sampling patterns that are below Nyquist sampling rate. D), e) and f) are the corresponding images with aliasing artifacts.

Cartesian k-space acquisition is the most popular sampling pattern in the clinic (25). In Cartesian sampling, individual readouts are acquired at multiple phase encoding locations by sweeping along the phase encoding (PE) direction in a sequential manner on a rectangular grid. Fourier transform can be directly applied to the Cartesian k-space to produce reconstructed images. In Cartesian acquisition, the center of k-space is acquired only once by the center line, which

results in sensitivity to motion artifact (26). Regular undersampling strategies for Cartesian sampling results in coherent aliasing along the PE direction (Figure 3.1d).

Radial k-space acquisition is another popular k-space sampling scheme. In radial sampling, projections are acquired in a star like pattern during which the center of k-space is sampled every line. Since the readout points don't exactly fall on Cartesian grid, a non-uniform Fourier transform (NUFFT) is used to grid the polar data onto a Cartesian gird (27). Radial sampling has multiple advantages over Cartesian k-space sampling such as lower sensitivity to undersampling aliasing artifact and motion artifacts. The aliasing artifact is more benign, i.e. the main structure/contrast of the object can still be recognized, because it always oversample the center k-space. This property combined with advanced image reconstruction techniques can achieve high acceleration factor and make undersampled radial imaging very fast. However, radial sampling suffers from multiple disadvantages compared to Cartesian sampling including: slow NUFFT gridding, lower SNR (28), sensitivity to trajectory errors (29), and sensitivity to eddy currents (30).

Spiral k-space acquisition is not used very often in clinic. In spiral sampling, it can cover the entire k-space in a single shot, but can also be used with a large number of interleaves for high resolution scans. While it has great potential for fast imaging, it's more sensitive to trajectory errors caused by hardware imperfections. Therefore, it is typically desirable to perform a one-time calibration for gradient delays and eddy currents for spiral imaging (31-33).

3.3) Parallel Imaging

There are many approaches to overcome the Nyquist limit. Parallel imaging is the hardware approach that has been applied on all clinical MRI scanners. Instead of having one big receiver

coil, independent coil arrays are used to receive MR signals in parallel. Each coil is sensitive to local spatial regions near its location (34), and data acquired from each individual coil are combined with specially designed reconstruction algorithms to removing aliasing artifact. The two most popular parallel imaging algorithms are sensitivity encoding (SENSE) (35), and generalized auto-calibrating partially paralleled acquisitions (GRAPPA) (36).

As shown in Figure 3.2, for an MR signal arising from point A in the patient, the sensitivities of Coils 1 and 2 for detecting that signal will be denoted S_{1A} and S_{2A} respectively. Similarly, the coil sensitivities for any other point B are also known and will be denoted S_{1B} and S_{2B}. When the data from each coil are reconstructed into images, significant wrap-around aliasing artifact is present. Each pixel (P) in the ½ FOV images has a signal that is the sum of contributions from two points (A and B) in the patient. The pixel values from Coils 1 and 2 (P_1 and P_2) are defined by equation 3.1.

$$\boldsymbol{P_1 = A \bullet S_{1A} + B \bullet S_{1B}}$$

$$\boldsymbol{P_2 = A \bullet S_{2A} + B \bullet S_{2B}} \qquad \textbf{Eq 3.1}$$

Since the P_i's and S_i's are all known, the true signals (A and B) can be calculated by simple algebraic methods for solving 2 simultaneous equations with 2 unknowns.

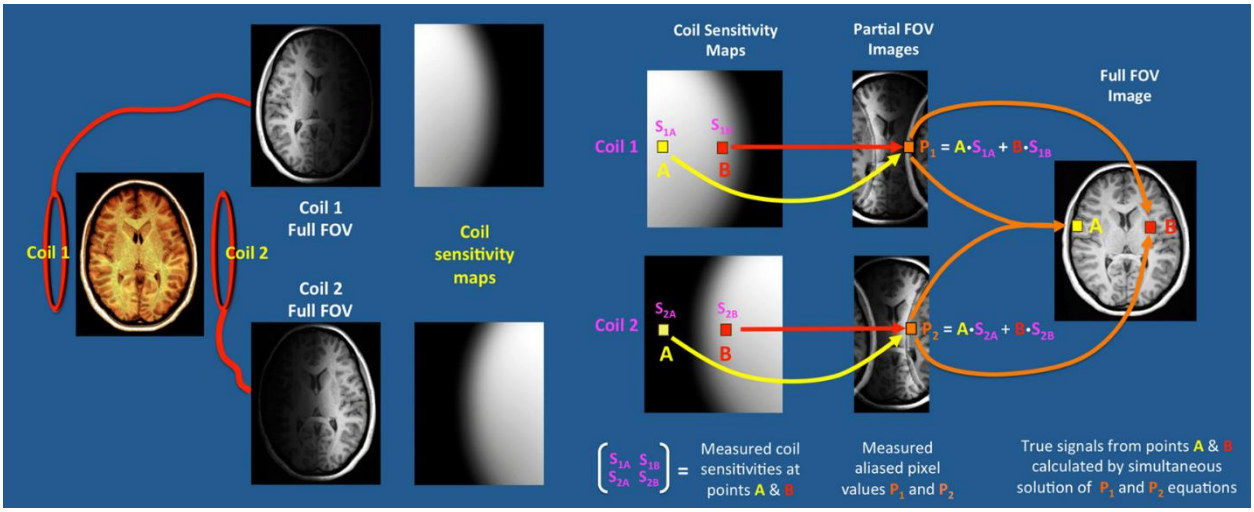

Figure 3.2. In SENSE, coil sensitivity profiles combined with undersampled images from each coil are used to solve for the ground truth image.

In GRAPPA, auto-calibration signal (ACS) obtained from additional k-space lines obtained during the MR scan are used to fill in the missing of k-space data. The GRAPPA algorithm utilizes GRAPPA kernel to find the GRAPPA weights which can provide the mathematical relationship between local multi-coil k-space data (source) to the Nyquist sampled k-space (target) (34). The kernel is slid across the k-space data to regions of undersampling, and the resulting weights obtained from ACS are used to fill in unknown k-space information. Like SENSE, GRAPPA reconstruction will exhibit greater degree of residual artifact at higher acceleration factors. One advantage of using GRAPPA over SENSE is that GRAPPA does not need sensitivity profiles.

3.4) Compressed Sensing

Nyquist sampling theorem indicates that by undersampling the signal, the resolved signal from the samples is no longer unique. In other words, the unknowns we have are more than the equations, which makes the solution to our problem no longer unique and that is where the aliasing comes from, i.e. because we cannot tell whether it is artifact or true signal by only calculating from our sampled data. But in most cases, we can tell the difference between aliasing and true signal from our experience, i.e. human brain is not overlapped. We are using our previous knowledge about the data to do so.

With the same principle, if we know the ground truth signals are sparse in certain transform domains, we can force the sparsity in the sampled signal to remove the aliasing, which is so called compressed sensing (CS). Shown in Figure 3.3, compressed sensing theory asserts that signals can be reconstructed using sampling rates much lower than the Nyquist if two conditions are met: 1) the signal is compressible allowing for sparse representation in a known transform domain, and 2) the signal frequency information was randomly sampled (37). Once these two conditions are met, aliasing artifact appears as noise-like artifact in the transform domain and can be removed using de-noising algorithms.

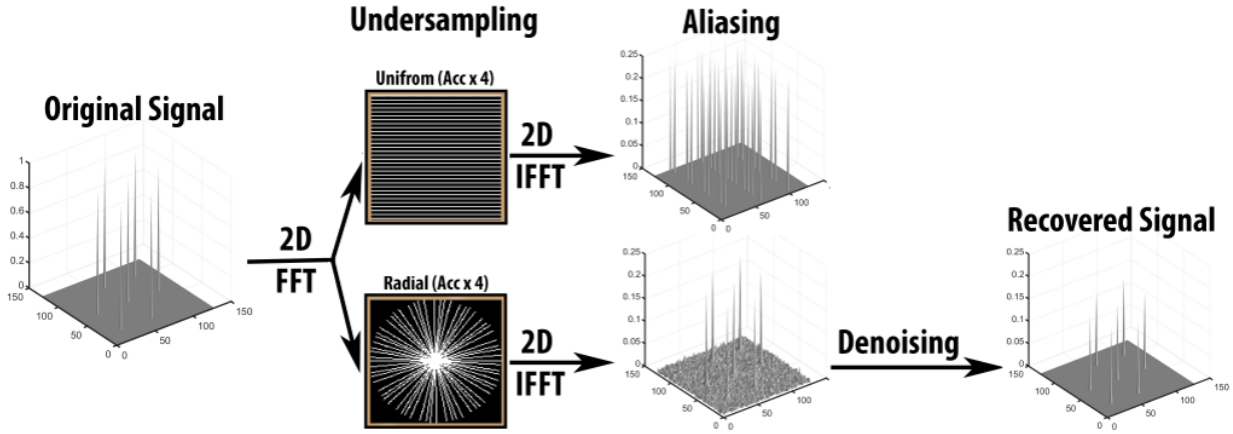

Figure 3.3. Diagram for compressed sensing. A sparse signal is undersampled by a factor of 4. Uniform Cartesian undersampling results in coherent aliasing artifact that cannot be recovered. Pseudorandom radial k-space sampling produces noise like incoherent aliasing artifact that can be removed using de-noising algorithm allowing for the recovery of the original signal.

Compressed sensing is typically combined with SENSE, when a MR image (m) can be represented sparsely in a known transform domain W (sparsifying transform), it can be recovered from undetermined system of equation by solving the L_1 norm minimization problem as shown by equation 3.2.

$$\min_{\boldsymbol{m}} \|\boldsymbol{Em} - \boldsymbol{y}\|_2^2 + \boldsymbol{\lambda}\|\boldsymbol{Wm}\|_1 \qquad \textbf{Eq 3.2}$$

Where E represents the multi-coil sampling operator, y is the acquired multi-coil undersampled data, and λ is the Laplacian weight which controls the trade-off between signal sparsity and data fidelity ($\|Em - y\|_2^2$). Note, if λ is set to 0, then the optimization problem reverts to iterative SENSE parallel imaging framework as previously described.

Finding the appropriate sparsifying transform for a given application is an important aspect of CS reconstruction, and currently an active area of research. For instance, Wavelet (37, 38) and

spatial temporal variation (39) transformation have been used to reconstruct undersampled 2D MR acquisition. Temporal finite difference (40, 41), temporal Fourier transform (42), and temporal principal component analysis (16) have been used for reconstruction of dynamic MR imaging. Both spatial and temporal sparsifying transform have been combined to improve CS images (41).

The introduction of CS to MRI has revolutionized cardiovascular MRI with unprecedented imaging speed that enables real-time, free-breathing scans. However, its clinic translation has been limited due to the increased reconstruction time for iterative optimization, which can't give the results immediately after each scan. To overcome the long reconstruction time, the most effective way is to use deep learning (DL).

3.5) Deep Learning

Deep learning is a subfield of machine learning concerned with algorithms inspired by the structure and function of the brain called artificial neural networks (ANNs). The learning can be supervised, semi-supervised or unsupervised (43-45) and it has been applied to fields including computer vision, speech recognition, natural language processing, audio recognition, social network filtering, machine translation, medical image analysis, etc. It has also been successfully applied to a wide variety of MRI related problems such as segmentation (46), classification (47), and image reconstruction (48-50). This dissertation will only focus on supervised learning using convolutional neural networks (CNNs) for MR image reconstruction and segmentation.

3.5.1) Multilayer Perceptron

The concept of neural network comes from multilayer perceptron (MLP). As shown in Figure 3.4, multilayer perceptron usually consists of input layer, hidden layer and output layer that

are fully connected to each other. Each node is a neuron that uses a nonlinear activation function, such as rectified linear unit (ReLU), to model the frequency of action potentials of biological neurons. This can be taken as solving the weights of a bunch of linear equations with known input/output pairs. In theory, the equations can be solved with enough input/output pairs using backpropagation, while the fully-connectedness of the networks makes them prone to overfitting and requires large GPU RAM when the data becomes large (i.e. images with millions of pixels).

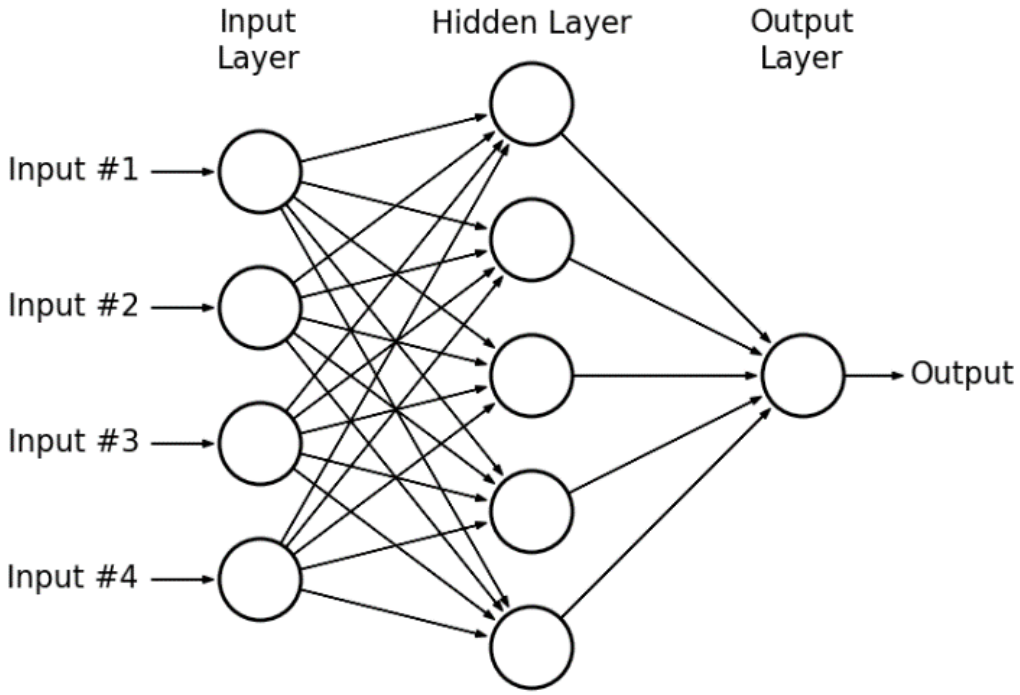

Figure 3.4. Multilayer perceptron usually consists of input layer, hidden layer and output layer that are fully connected to each other.

3.5.2) Convolutional Neural Network

Convolutional neural networks are regularized version of multilayer perceptrons. Instead of fully connected, CNNs take advantage of the hierarchical pattern in data and assemble more

complex patterns using smaller and simpler patterns. Convolutional kernels (i.e. 3x3 matrix for 2D, 3x3x3 for 3D) are used to convolve with input images to detect certain image features such as edges and corners. These features are learning during the training process that best represent the processing from input data to output data. Using convolutional kernels is advantageous because of its ability to learn local correlations in a shift invariant way, and because it reduces the number of weights in a network (51). CNNs also utilize non-linear activation (i.e. ReLU) to determine the information retained from outputted feature maps.

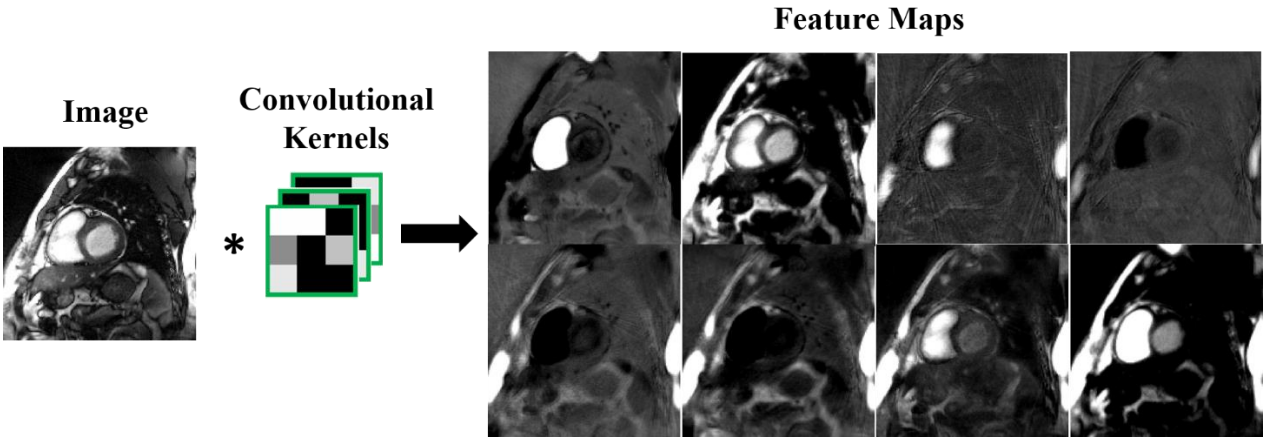

Figure 3.5. An example for convolution operations. An image is convolved with multiple 3x3 convolutional kernels to get feature maps.

In addition to convolutional layer, there are other layers such as pooling layer and batch normalization layer. Pooling layers are used to down sample an image, which allows the network learn high level patterns of the image. It is extremely important for image segmentation, where the relative spatial location is very important. These different layers/operations consist of a CNN architecture, such as U-Net(52), Generative Adversarial Network (GAN)(53), Cascade CNN(54), etc. As shown in Figure 3.6, the input/output pairs are fed into a U-Net to train the weights in the

network. Gradient optimization algorithms such as stochastic gradient descent, or ADAM optimizer are used to update network kernel weights by back-propagation. While the iterative training process may take hours to days to finish, the testing process is very fast (on the order of seconds per case). With deep learning, clinic translation is possible for highly accelerated acquisition methods.

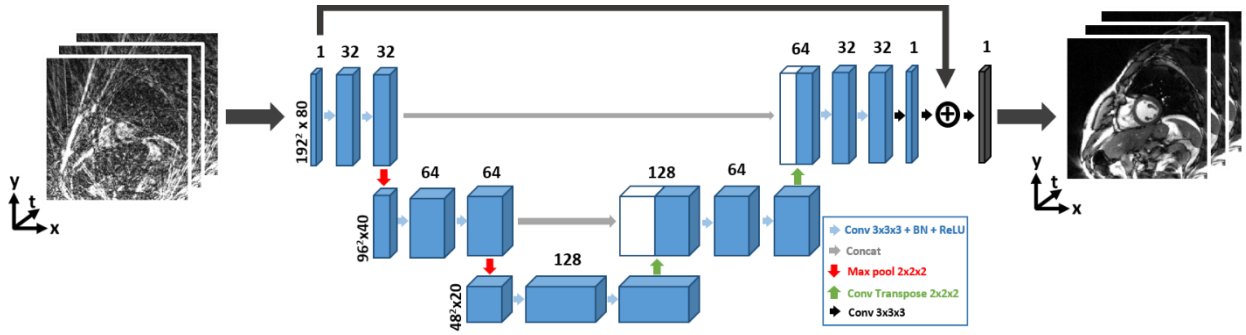

Figure 3.6. 3D U-Net for 2D + time image reconstruction. The undersampled aliasing images are used as inputs and the CS reconstructed clean images as reference. The network will learn the dealiasing process during iterative training. For testing, the trained network is applied to testing inputs and making it significantly faster than CS.

3.6) Discussion

Cartesian k-space acquisition is the most widely used k-space sampling pattern in clinic but suffer from coherent aliasing when undersampled. Cartesian k-space sampling is also sensitive to arrhythmia and respiratory motion. Radial sampling pattern is more robust with respect to motion artifact and aliasing, but suffers from lower SNR, sensitivity to eddy currents, and sensitivity to gradient delay. Radial undersampling resistance to aliasing artifact makes it an ideal candidate for accelerated acquisition but requires additional processing (i.e. parallel imaging, CS, and DL) for best performance.

As stated previously, three major reconstruction methods for accelerated MRI acquisitions are parallel imaging, CS, and DL. One limitation of parallel imaging is the relatively low achievable acceleration rates R=2-3 (55) compared to CS (R = 3 static imaging (56), R > 6 dynamic imaging (49, 57-59)). One advantage of using parallel imaging is that both SENSE and GRAPPA reconstruction are fast, allowing for inline reconstruction. While CS can achieve higher acceleration factor, the major disadvantage of CS is the relatively long reconstruction times. For instance, CPU based CS can require hours (42) and GPU based CS can require minutes to reconstruct MR images (49, 60). DL can accelerate MR imaging at similar or greater acceleration factors compared to CS (54, 61, 62), but at a much faster rate (on the order of seconds). The main disadvantage of DL is the need for large training data sets for training. Acquiring training data, especially high quality reference data, can be challenging given the dearth of available MR raw data.

Chapter 4: Single-Shot Coronary QISS MRA using Compressed Sensing

4.1) Introduction

Congenital heart disease (CHD) is the most common type of birth defect, accounting for nearly 1% of live births in the US (63, 64). Non-invasive assessment of coronary origins is critical for planning surgical intervention and cardiac catheterization in patients with CHD. For example, coronary imaging is necessary for patients who undergo an arterial switch operation for transposition of the great arteries along with coronary arteries (65, 66). While echocardiography is the first line imaging test for evaluation of coronary origins, its accuracy worsens as the pediatric patients grow in size (67). Computed tomography (CT) and magnetic resonance imaging (MRI) are two available non-invasive imaging tests for coronary angiography. Compared with adults, children have smaller hearts and faster heart rates, both posing greater challenges for producing diagnostically acceptable image quality.

Cardiac CT examination involves ionizing radiation and iodinated contrast agent administration, both of which are concerning for pediatric patients (68, 69). While pediatric cardiovascular magnetic resonance angiography (MRA) does not involve radiation, it typically involves gadolinium-based contrast agent (GBCA)(69). Gadolinium has been reported to be deposited in the brain even in the setting of normal renal function (70-74), including in children (75, 76). Despite the lack of evidence linking adverse side effects to the gadolinium deposition in the brain (77), is nevertheless concerning. In addition, MRA examinations may require general anesthesia in young children to obtain high-quality images. Mounting evidence from animal and

human studies suggest that general anesthetics may cause neurotoxic changes in the developing brain that lead to adverse neurodevelopmental outcomes later in life. Thus, there is a clinical need to develop pediatric cardiovascular MRA methods that do not require GBCA or anesthesia.

Non-contrast MRA is an alternative test for coronary angiography without requiring administration of GBCA. Among a family of non-contrast MRA methods (78), navigator-gated, T2-prepared balanced steady state free precession (b-SSFP) MRA (79) is the most commonly used method in adults. This 3D coronary MRA pulse sequence has been shown to produce clinically acceptable image quality in adults with a scan time on order of 10 min (80-82), whereas a breath-hold version is less likely to produce clinically acceptable image quality because of high data acceleration (83). Because a 3D cardiovascular MRA pulse sequence with high spatial resolution generally requires long scan time, it is ill-suited to relax the need for anesthesia during pediatric cardiovascular MRI. This study seeks to test the feasibility of single-shot coronary MRA without requiring GBCA or anesthesia for future use in pediatric patients.

One potential solution for real-time MRA is the recently developed coronary Quiescent-Interval Slice-Selective (QISS) MRA (84) based on radial k-space sampling. The original implementation was evaluated in adults as a breath-hold version, where 10 continguous 2D images were acquired in a single breath-hold of 20 heart beats (i.e., 2-shots spread over 2 heart beats per image). To date, coronary QISS MRA has not been evaluated in patients with CHD, and single-shot coronary QISS MRA has not been evaluated in any cohort. Compared with previously described 2-shot coronary QISS MRA, advantages of real-time coronary QISS MRA include capability of relaxing the need for anesthesia during pediatric caridiovascular MRI and being less sensitive to irregular heart rhtyhm or motion. In this study, we sought to test whether it is feasible

to visualize the coronary origins in patients with CHD using single-shot coronary MRA with compressed sensing (CS)(85). Success of this study will serve as an important step towards clinical translation of real-time coronary QISS MRA in pediatric patients.

4.2) Methods

4.2.1) Patients Demographics

This is a retrospective study involving 14 patients with CHD (mean age = 17.0 ± 8.6 years; 8 males; 6 females; see Table 4.1 for relevant clinical profiles). This study leveraged a parent study which was aimed to comparing previously described breath-hold coronary QISS MRA and clinical standard contrast-enhanced (CE) MRA. From this point forward, previously described coronary QISS MRA will be referred to as 2-shot QISS MRA and accelerated coronary QISS MRA with CS will be referred to as single-shot QISS MRA. The study was approved by the local ethics board, and informed consent was obtained from all participants (or parents) for QISS MRA. We evaluated the feasibility of single-shot coronary QISS MRA by retrospectively undersampling the raw data of 2-shot coronary QISS MRA, performing CS reconstruction, and comparing the retrospectively derived single-shot QISS MRA to 2-shot coronary QISS MRA and clinical CE MRA. Both general anesthesia and GBCA (0.12 ml/kg of gadofosveset trisodium or ABLAVAR, Lantheus Medical Imaging, MA, USA) were administered using clinical standard protocols, and this research study had no bearing on these clinical protocols.

As a secondary evaluation, we prospectively scanned three adult patients (3 male, mean age = 58.7 ± 6.5 years) who underwent clinical cardiovascular MRI and performed breath-hold, 2-

shot QISS MRA (reference) and free-breathing, single-shot coronary QISS MRA with otherwise identical imaging parameters.

Characteristic	
Age	17.0 ± 8.6 years
Females	6/14 (42.9%)
Heart Rate	80.8 ± 19.7 bpm
RV dilatation	5/14 (36%)
Aortic root dilatation	4/14 (29%)
BAV	2/14 (14%)
Pulmonary atresia	2/14 (14%)
VSD	2/14 (14%)
TOF	2/14 (14%)
Ascending Aorta dilatation	2/14 (14%)
RPA abnormality	2/14 (14%)
LV hypoplasia	2/14 (14%)
Pulmonary regurgitation	2/14 (14%)
Aortic coartctation	2/14 (14%)
Tricuspid valve hypoplasia	1/14 (7%)
Right ventricular outflow tract obstruction	1/14 (7%)
Marfan	1/14 (7%)
Thoracolumbar scoliosis	1/14 (7%)
Pectus excavatum	1/14 (7%)
DORV	1/14 (7%)
Mitral valve atresia	1/14 (7%)
Myocardial hypertrophy	1/14 (7%)
Tricuspid valve prolapse	1/14 (7%)
LPA dilatation	1/14 (7%)

Mitral valve prolapse	1/14 (7%)
Double Outlet Left Ventricle	1/14 (7%)

Table 4.1. Pertinent clinical profiles of 14 patients enrolled in this study. BAV: Bicuspid aortic valve; VSD: Ventricular septal defect; TOF: tetralogy of Fallot; DOVR: Double outlet right ventricle.

4.2.2) Hardware

A prototype two-shot coronary QISS MRA pulse sequence was implemented on a whole-body 1.5T scanner (MAGNETOM Aera, Siemens Healthineers, Erlangen, Germany). This scanner was equipped with a gradient system capable of achieving a maximum gradient strength of 45 mT/m and a slew rate of 200 T/m/s. The RF excitation was performed using the body coil. Standard multi-coil arrays (anterior and spine elements, typically 36 elements total) were employed for signal reception.

4.2.3) Pulse Sequence

Relevant imaging parameters of coronary QISS included: field of view (FOV) = 180 mm × 180mm, image acquisition matrix size = 128 × 128, spatial resolution = 1.4 mm x 1.4 mm, slice thickness = 2.1 mm, cardiac triggering, 96 rays per 2D image (or 48 rays per heart beat), 2 heart beats per 2D image, 13.123° angular increments between successive rays, flip angle 140°, TE = 1.9 ms, TR = 3.7 ms, receiver bandwidth = 1,000 Hz/pixel, fat suppression, and α/2 flip-back pulse immediately before b-SSFP readout, number of slices = 10, inversion time (TI) = 650 ms following in-plane frequency offset corrected inversion (FOCI) pulse (86). Using scout images displaying the left ventricular outflow tract, QISS MRA was prescribed perpendicular to the

outflow tract and parallel to the aortic valve plane in order to sample the coronary origins. Coronary QISS MRA was always performed before GBCA was administered.

Navigator-gated, CE 3D MRA based on inversion recovery with gradient echo readout was performed using the following imaging parameters: FOV = 340 mm x 319 mm, image acquisition matrix = 224 x 210, spatial resolution = 1.5 mm x 1.5 mm, slice thickness = 2.4 mm (interpolated to 1.5 mm as per clinical protocol), slices = 104 (23.1% oversampling), cardiac triggering, GRAPPA parallel imaging factor = 1.9, receiver bandwidth = 485 Hz/pixel, TI = 260 ms, flip angle = 18 °, TE = 1.35 ms, TR = 3.3 ms, scan time on the order of 5-15 min (depended on patient's breathing pattern), and centric k-space ordering. CE-MRA was prescribed in a coronal plane. Standard dose (0.12 ml/kg) of gadofosveset trisodium was administered using a power injector at 2-3 ml/s. Note that inversion-recovery 3D MRA was performed following time-resolved MRA.

4.2.4) Image Reconstruction

Figure 4.1 illustrates the overall flow chart of image reconstruction. Two-shot QISS data were retrospectively undersampled in k-space by a factor of two and then reconstructed using CS. We used nonuniform Fast Fourier transform (NUFFT)(87) because it produces less blurring than the conventional two-step process with gridding and fast Fourier transform. Coil sensitivities were self-calibrated from the low resolution, zero-padded reconstruction using the method described in reference (88, 89).

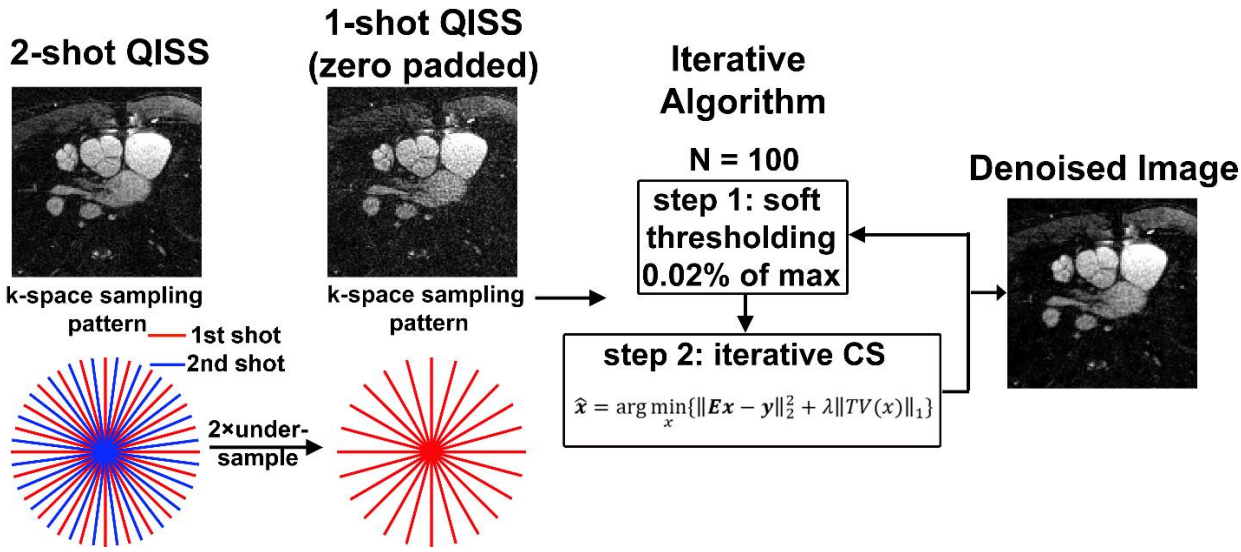

Figure 4.1. A schematic flowchart illustrating the image reconstruction pipeline. Step 1: Two-shot radial QISS data were undersampled in k-space by a factor of 2. Step 2: an iterative CS algorithm was used to reconstruct the results, where spatial TV was used as the sparsifying transform. Soft thresholding was used as a pre-step to improve artifact suppression. Radial k-space sampling patterns are displayed after down sampling by a factor of 4 for better visualization with less clumping.

We performed two pre-processing steps prior to CS reconstruction. In the first step, we performed gradient trajectory correction during post-processing while assuming identical gradient shifts around 360° (see Figure 4.2). In the second step, we performed density compensation based on the sampling pattern and NUFFT to ensure a fair comparison of intensity between 2-shot and 1-shot QISS results.

To remove image artifacts associated with gradient trajectory errors in k-space, we performed trajectory correction during post-processing while assuming identical gradient shifts around 360°. We identified a single shift factor using 6 pilot cases by shifting the rays in k-space from -1 to 1 k-space point (0.1 k-space point steps) and identifying the shift that produced the lowest artifact in signal-free background. This post-processing correction method was deemed reasonable since all data were acquired from a single 1.5T MRI scanner. As shown in Figure 4.2,

our analysis showed that -0.3 k-space shift produces the least amount of artifacts from the aforementioned range (see plot on right) and consistently showed incremental improvement in artifact suppression than without phase correction.

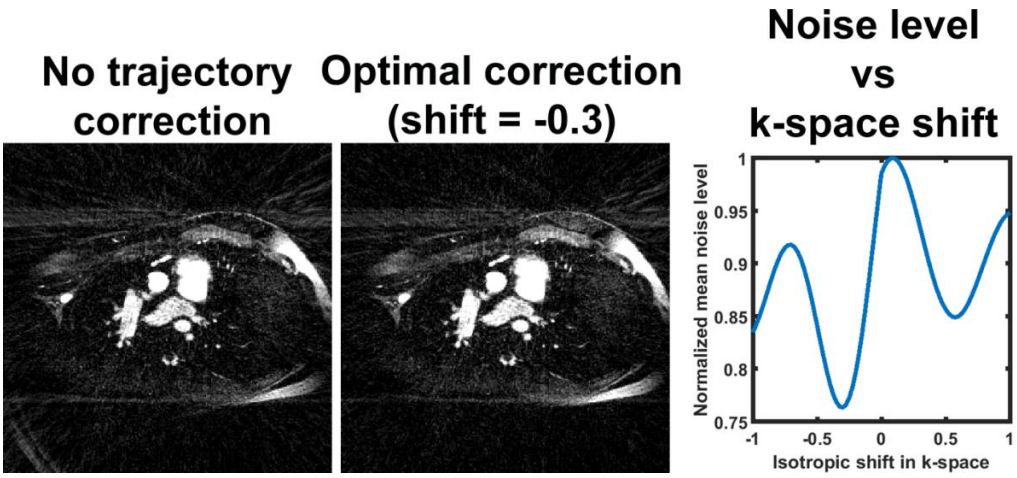

Figure 4.2. Representative QISS images without (default, left column) and with (middle column) gradient trajectory correction. (Right column) Mean normalized signal from background (i.e., signal-free region) plotted as a function of isotropic shift in k-space. This plot represents result from 6 pilot data from the same MRI system. This post-processing approach was used because the prototype QISS MRA acquisition did not separately acquire calibration data for gradient trajectory correction.

For the iterative CS image reconstruction, an L1-norm optimization was used with spatial total optimization (TV) as the sparsifying transform, where the normalized regularization weight was 0.000025 relative to the maximum signal. This value was determined empirically based on visual analysis of data agreement between 2-shot and 1-shot training data, using a similar approach described previously (15, 16). We varied the reconstruction pipeline to determine whether adding soft thresholding (@ 0.02% of maximum intensity) as a pre-step filters more residual aliasing artifacts than otherwise. All image reconstructions were done offline in MATLAB R2016a

software (Natick, MA, USA) on a standard computer with Windows 7. Image reconstruction time was recorded to determine clinical feasibility.

4.2.5) Image Analysis

We performed both qualitative and quantitative analyses to evaluate results. For quantitative analyses, comparison between 2-shot and 1-shot QISS MRA, we calculated the structural similarity index (SSIM)(90), normalized root mean square error (NRMSE), and edge sharpness to infer data fidelity. Because both 2-shot and 1-shot results share the same data, it was possible to compute SSIM and NRMSE over the entire image. For SSIM and NRMSE calculations, we generated a mask based on thresholding to exclude signal-free pixels. This step was necessary to ensure that these metrics do not include spurious data points from signal-free regions. For edge sharpness estimation, we measured intensity profiles through an aorta or atrium to background. To increase precision in calculating edge profiles, we interpolated each profile by a factor of 20 and measured the spatial distance between 25 percentiles and 75 percentiles of peak intensity value. For each of three metrics, the two groups (2-shot vs. 1-shot QISS) were compared using a paired (two-tail) t-test, where $P < 0.05$ was considered statistically significant. We calculated the apparent signal-to-noise ratio (SNR) as the mean signal of several regions of interest (ROIs) within cardiovascular structures (yellow ROIs in Fig. 4.3) divided by standard deviation of signal free background (cyan rectangle in Fig. 4.3), as previously described (91).

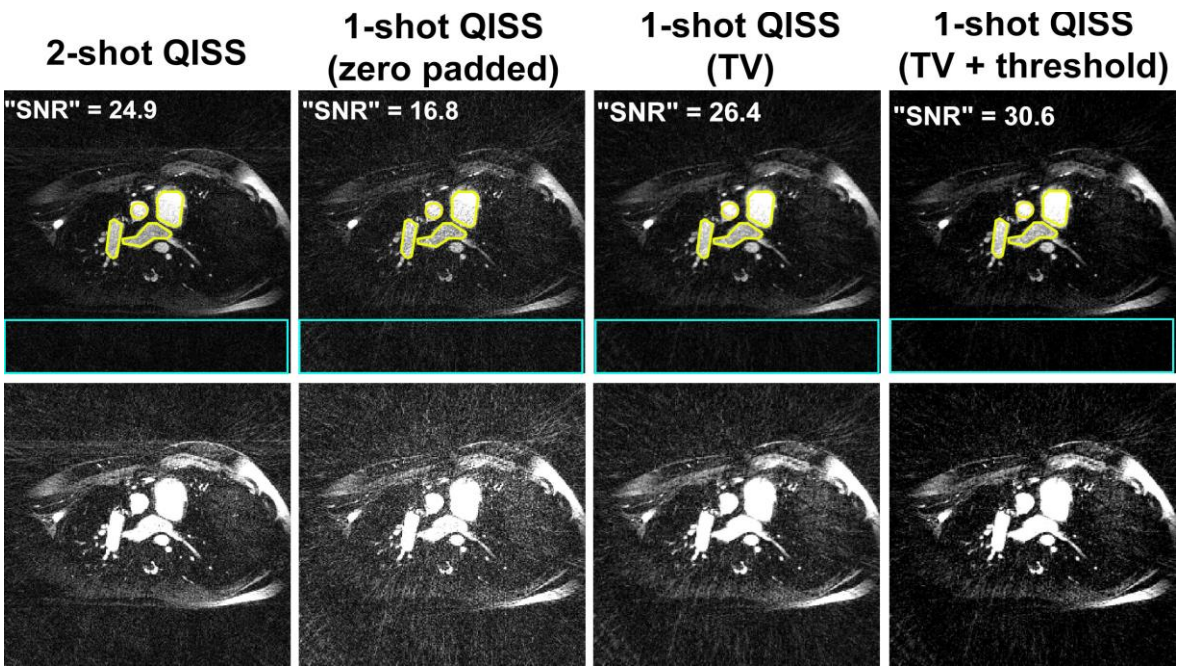

Figure 4.3. (Top Row) Representative images of 2-shot QISS (first column), single-shot QISS with zero padding (second column), single-shot QISS with spatial TV denoising (third column), and single-shot QISS with spatial TV denoising plus soft thresholding (fourth column). Superimposed yellow ROIs represent areas used to calculate mean signal. Superimposed cyan rectangle represents a background region used to calculate noise. (Bottom Row) Corresponding images displayed with a narrow grayscale to bring out background signal.

A total of 39 MRA data sets were randomized and de-identified for visual analysis. One pediatric cardiovascular radiologist (CKR) with 17 years of experience and one pediatric cardiologist (JDR) with 9 years of clinical experience, respectively, graded the conspicuity of coronary origins on a 5-point Likert scale (1 = nondiagnostic, 2 = poor, 3 = clinically acceptable, 4 = good, 5 = excellent). The two readers were given training data sets with varying image quality to calibrate their scores together prior to actual grading. Following training, each reader was blinded to image acquisition type (2-shot QISS, 1-shot QISS, contrast-enhanced MRA), each other, and clinical history. For fairness, CE MRA data were reformatted using a 3D viewing tool

(Leonardo Workstation, Siemens) to match the FOV, orientation, and spatial coverage as QISS MRA. Note that each case (1-shot QISS, 2-shot QISS, CE MRA) was displayed and evaluated separately. The mean image quality scores for each side (left and right origins) were compared between the three groups (2-shot QISS, 1-shot QISS, CE-MRA) using the Kruskal-Wallis test, where Fisher's least significant difference was used to compare each pair. The Bland-Altman analysis was used to compute reader agreement.

4.3) Results

All 14 cases included coronary origins, except for 1 case where the origins were missed due to scanning operator mistake. This one case with limited spatial coverage was excluded for qualitative evaluation of image quality of coronary origins but included for quantitative evaluation of image quality.

Figure 4.3 shows representative images comparing 2-shot QISS, 1-shot QISS with zero padding (i.e., without CS), 1-shot CS with TV alone, and 1-shot QISS with TV plus soft thresholding. As shown in Fig. 4.3, the mean apparent SNR was 24.9, 16.8, 26.4, and 30.6 for 2-shot QISS, 1-shot QISS with zero padding, 1-shot QISS with TV, and 1-shot QISS with TV plus soft thresholding, respectively. Note that an increase in apparent SNR with CS is due to noise filtering and is not to be confused with intrinsic SNR. Starting from this point, the remaining 1-shot QISS results correspond to CS with spatial TV plus soft thresholding.

Figure 4.4 shows representative edge profiles through blood and background from another subject. These profiles show that the results are comparable. Summarizing the results over 14 patients with CHD, the mean edge sharpness values were not significantly different ($P > 0.6$)

between 2-shot QISS (1.2 ± 0.3 mm) and 1-shot QISS (1.3 ± 0.3 mm). Compared with 2-shot QISS, 1-shot QISS produced NRMSE of 5.8 ± 0.8 % and SSIM of 95.4 ± 1.6 %, suggesting high data fidelity produced by CS reconstruction. Compared with 2-shot QISS (offline reconstruction time = 16.0 ± 0.1 s per 2D image accounting for pre-processing steps and multi-coil NUFFT), 1-shot QISS required significantly ($P < 0.05$) longer offline reconstruction time (77.4 ± 0.7 s per 2D image accounting for pre-processing steps, multi-coil NUFFT, and CS).

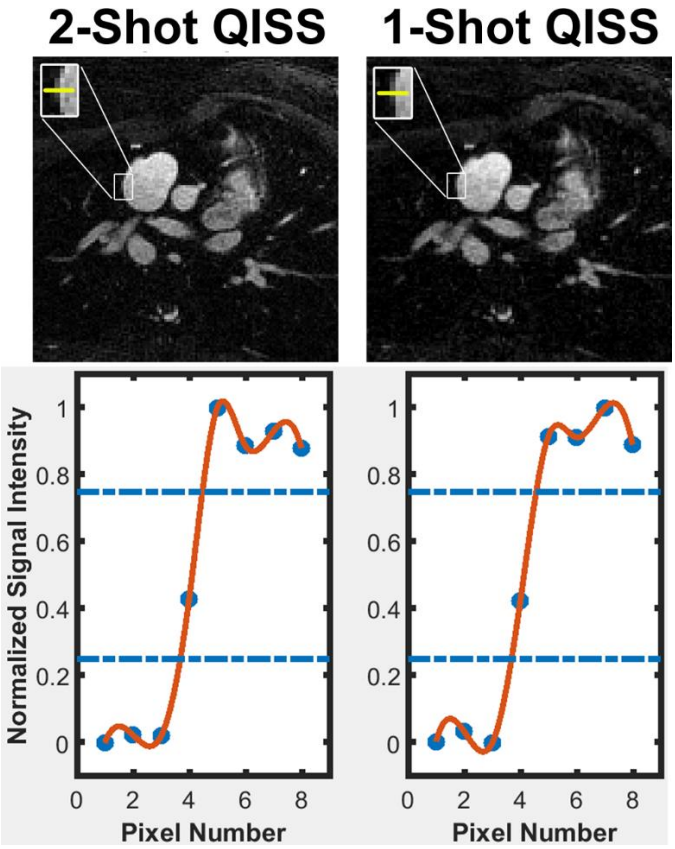

Figure 4.4. Spatial intensity profiles (yellow lines) through blood and background to represent edge sharpness: 2-shot QISS (left column) and single-shot QISS with spatial TV plus soft thresholding (right column). Edge sharpness was defined as the distance between 25 and 75 percentiles of peak intensity value.

Figure 4.5 shows representative QISS and CE MRA maximum-intensity-projections (MIP) in the same orientation and FOV, where both coronary origins are visible. Summarizing the results over 13 patients (Table 4.2), compared with visual scores for clinical CE-MRA (4.2 ± 0.5 and 4.1 ± 0.6 for right and left coronary origins, respectively), the mean reader scores were not significantly different ($P > 0.3$) for 2-shot QISS (4.4 ± 0.9 and 4.2 ± 1.1, respectively) and single-shot QISS (4.3 ± 1.1 and 3.8 ± 1.3, respectively) and deemed clinically acceptable to good (scores ≥ 3.0). The reader agreement was similar between CE-MRA and coronary QISS MRA (Table 4.3).

Figure 4.6 shows representative breath-hold, 2-shot QISS (reference) and prospectively acquired free-breathing 1-shot QISS MRA obtained from three adult patients. In patient 3 who had intermittent arrhythmia during MRI, single-shot QISS produced better image quality than 2-shot QISS. Consistent with retrospective results from pediatric patients, these prospective examples in adults suggest that it is feasible to produce diagnostically acceptable image quality with real-time coronary QISS MRA.

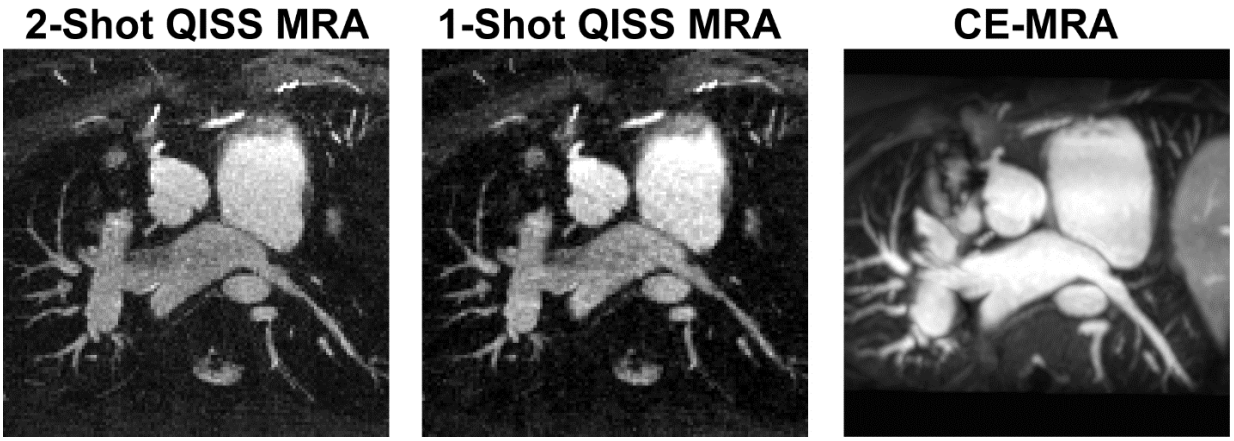

Figure 4.5. Representative maximum-intensity-projections (MIPs) displaying the coronary origins: 2-shot QISS (left column), single-shot QISS with spatial TV plus soft thresholding (middle column), and CE MRA reformatted to match the orientation of QISS MRA (right column). Yellow arrows point to the coronary origins.

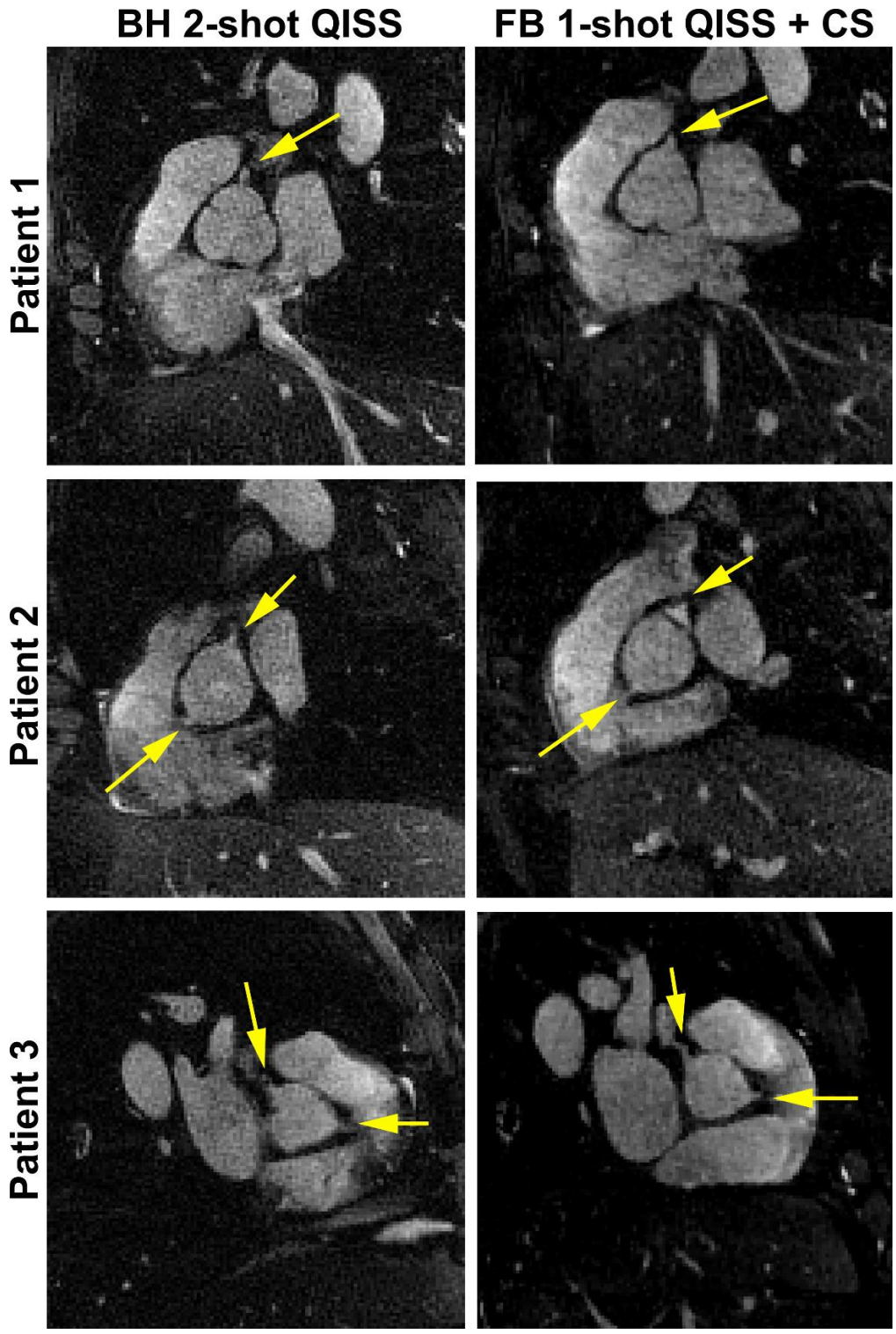

Figure 4.6. Images comparing prospectively acquired free-breathing, 1-shot coronary QISS (right column) to breath-hold, 2-shot QISS (left column) obtained from three adult patients. Yellow

arrows point to the coronary origins. The hearts were in different positions between breath-hold and free-breathing acquisitions as shown.

Region	Category	Reader 1	Reader 2
Origin of RCA	**2-Shot QISS**	4.5 ± 0.8	4.3 ± 1.2
	1-Shot QISS CS	4.4 ± 1.0	4.2 ± 1.2
	CE-MRA	4.2 ± 0.8	4.3 ± 0.5
Origin of LMCA	**2-Shot QISS**	4.2 ± 1.2	4.2 ± 1.1
	1-Shot QISS CS	3.8 ± 1.2	3.8 ± 1.4
	CE-MRA	4.0 ± 0.9	4.2 ± 0.6

Table 4.2. A summary of reader scores from 13 patients with CHD. According to the Kruskal-Wallis test, the three groups (2-shot QISS, 1-shot QISS, and CE-MRA) were not significantly different ($P > 0.2$) for each coronary origin per reader, as well as combined. The reported values represent mean ± standard deviation. RCA: right coronary artery; LMCA: left main coronary artery. A 5-point Likert scale (1 = nondiagnostic, 2 = poor, 3 = clinically acceptable, 4 = good, 5 = excellent).

Region	***Parameter***	***Mean***	***Mean Difference***	***Lower 95% Limit***	***Upper 95% Limit***
Origin of RCA	***2-Shot QISS***	4.4	-0.2	-1.5	1.2
	1-Shot QISS CS	4.3	-0.2	-0.9	0.6
	CE-MRA	4.3	0.2	-1.4	1.7
Origin of LMCA	***2-Shot QISS***	4.2	0.0	-0.8	0.8
	1-Shot QISS CS	3.8	0.0	-1.1	1.1
	CE-MRA	4.1	0.2	-1.6	2.0

Table 4.3. A summary of reader agreement as per Bland-Altman analysis. The reader scores were in good agreement (i.e., low bias) with similar confidence intervals between 2-shot QISS, 1-shot QISS, and CE-MRA.

4.4) Discussion

This retrospective study shows that it is feasible to visualize the coronary origins in patients with CHD with clinically acceptable to good image quality using single-shot, coronary QISS MRA with CS. Compared with 2-shot QISS and clinical CE-MRA images, single-shot, QISS images obtained with CS reconstruction produced reader scores that were not significantly different. Clinically acceptable to good image quality scores are supported by quantitative image metrics such as SSIM, NRMSE, and edge sharpness.

This study warrants several discussion points. First, SNR measurements need to be interpreted with caution because CS filters noise and changes the noise distribution. As such, SNR values reported in this study should not be confused with intrinsic SNR. Second, we did not explore an optimal radial angle for CS reconstruction, because this study was designed as a sub-study of a parent study, and we did not have access to the source codes to modify the pulse sequence. Additional analysis is needed to determine which radial angle optimally balances signal homogeneity and artifacts arising from eddy currents in b-SSFP readout. Third, for clinical translation, it is important to consider image reconstruction time with CS. Strategies to reduce the reconstruction time in future work may include leveraging graphics processing unit (GPU) computing, software coil compression (92), and Split Bregman methods to efficiently solve the L-1 norm (93). Rapid CS reconstruction is an active area of research within the MRI community,

and MR vendors are beginning to advertise CS as a future product. Thus, it is likely that a rapid image reconstruction pipeline could become commercially available. Fourth, this study used spatial TV and soft thresholding to de-noise undersampled QISS data. It may be possible to increase the accelerate rate with other constraints such as non-local-means (94-96), at the expense of increased computational demand. Another study is warranted to explore the trade-offs between data fidelity and computational demand using different sparsifying transforms. Fifth, advantages of single-shot coronary QISS MRA over 2-shot coronary MRA include capability to relax the need for anesthesia during pediatric cardiovascular MRI and insensitivity to arrhythmia or motion.

A rapid NC-MRA method that does not require general anesthesia or GBCA has important clinical implications for pediatric cardiovascular MRI. First, it reduces cost by eliminating MR-compatible anesthesia equipment, specialized personnel, anesthetics, and GBCA. Second, it reduces risk. As animal and human studies show that general anesthetics may cause neurotoxic changes in the developing brain that lead to adverse neurodevelopmental outcomes later in life. Indeed, in 2012, the FDA, SmartTots, and the American Academy of Pediatrics released a consensus statement recommending no anesthetics in patients under 3 years for elective procedures (97). Gadolinium has been reported to be deposited in the brain even in the setting of normal renal function (70-74), including in children (75, 76). In July 2015, the FDA issued a Safety Communication, stating "**...**health care professionals should consider limiting GBCA use to clinical circumstances in which the additional information provided by the contrast is necessary and …Health care professionals are urged to reassess the necessity of repetitive GBCA in established treatment protocols" (98).

This study also includes several limitations. First, the primary analysis included only 14 patients with CHD. Additional investigation in a larger cohort of patients is needed to evaluate the clinical utility of single-shot, coronary QISS MRA. Second, in this study, we performed gradient trajectory correction using a simple empirical approach, because we had no access to the source codes for implementing a pre- or post-scan calibration scan. This study did not explore recently published self-calibration methods (99, 100), since they are beyond the scope of this study. Another study is warranted to evaluate the advantages (possibly better artifact suppression) and disadvantages (additional scan time) of different phase correction strategies. Third, the primary data analysis was performed on retrospective reconstruction of breath-hold, 2-shot coronary QISS MRA in patients with CHD. While this restriction is a limitation, it is worth noting that a retrospective analysis also made it possible to compute quantitative metrics such as SSIM and NRMSE because the 2-shot and single-shot data sets are inherently registered. Our secondary evaluation in three adult patients suggests that it is feasible to visualize coronary origins using free-breathing, single-shot coronary QISS MRA. A future study is warranted to confirm this finding in patients with CHD. Fourth, this study did not evaluate the sharpness of coronary vessels using advanced visualization tools such as “Soap-Bubble” (101), because coronary origins in patients with CHD are small. Developing another visualization tool is beyond the scope of this study.

In conclusion, it is feasible to visualize the coronary origins in patients with CHD with clinically acceptable to good image quality using single-shot coronary QISS MRA with CS.

Chapter 5: Multi-TI Late Gadolinium Enhancement MRI with Compressed Sensing

5.1) Introduction

Late gadolinium enhanced (LGE) (102-104) MRI is considered the gold standard test for assessment of myocardial scarring. For 2D LGE, there are two different approaches in clinical routine: 1) segmented, breath-held (BH) acquisition with gradient echo readout and relatively high spatial resolution (~1.5 mm x 1.5 mm); 2) single-shot, free-breathing acquisition with balanced steady-state free precession (b-SSFP) readout and relatively low spatial resolution (~2 mm x 3 mm). While breath-held LGE provides higher spatial resolution than single-shot LGE, it requires considerably longer scan time and is more sensitive to arrhythmia and inconsistent breath-holding. While single-shot LGE MRI is the preferred method for patients with arrhythmia and/or dyspnea, its relatively low spatial resolution (~2 mm x 3 mm) may reduce accuracy for visualizing small, subendocardial infarcts, quantifying myocardial scar volume, microvascular obstruction, or identifying peri-infarct zones. Thus, there is a need to develop high spatial resolution single-shot LGE MRI for patients with arrhythmia and/or dyspnea.

One approach to achieve higher spatial resolution is to perform free-breathing single-shot LGE that averages repeated acquisitions with motion correction (MOCO)(105). This approach, however, necessitates longer repeated acquisitions and is sensitive to arrhythmia and/or bulk motion. Another approach is to accelerate single-shot LGE using compressed sensing (CS)(37). But, to our knowledge, there are no published papers describing CS-accelerated single-shot LGE. We speculate that it may be due to the difficulty in accelerating a single-shot LGE image beyond

acceleration factor (R) three, thereby limiting how far CS can increase the spatial resolution of a 2D LGE image while producing clinically acceptable image quality. In this study, we sought to achieve a high acceleration factor (R=20) by rebinning a lengthy single-shot LGE k-space data into multiple timeframes and exploiting temporal sparsity. With the time-resolved reconstruction approach, we not only achieve high temporal resolution (34.1 ms per time frame), but also obtain extra information about signal change over time that could potentially improve diagnostic confidence, detect other abnormalities (e.g. thrombus, microvascular obstruction), and/or assist in segmenting scar boundaries.

The purpose of this study was to develop a 20-fold accelerated multi-frame, single-shot LGE pulse sequence with high nominal spatial resolution (1.3 mm x 1.3 mm) using radial k-space sampling, k-space weighted image contrast (KWIC)(106), and CS reconstruction enforcing temporal sparsity (107) and evaluate its performance against clinical standard single-shot LGE (2.2 mm x 2.7 mm) in patients undergoing routine clinical cardiovascular MRI.

5.2) Materials and Methods

5.2.1) Patients Demographics & Clinical CMR Protocol

This study was conducted in accordance with protocols approved by our institutional review board and was Health Insurance Portability and Accountability Act (HIPAA) compliant. All subjects provided informed consent in writing. We prospectively enrolled 20 patients (mean age = 63.6 ± 17.1 years; 14 males; 6 females) undergoing a clinical cardiovascular MRI. See Table 5.1 for patient characteristics that are relevant for this study.

As recommended by the Society of Cardiovascular Magnetic Resonance consensus statement (108), each patient received either 0.15 or 0.20 mmol/kg of gadobutrol (Gadavist, Bayer HealthCare Whippany, USA), depending on whether the estimated glomerular filtrate rate (eGFR) was 45-59 mL/min per 1.73 m^2 or $\geq$ 60 mL/min per 1.73 m^2, respectively, and LGE was performed approximately 10-15 min after administration of contrast agent. In all patients, our research LGE scan was performed immediately after the clinical single-shot LGE scan. This order was unavoidable due to higher priority given to clinical LGE.

Characteristics	ALL (N = 20)
Age	63.6 ± 17.1 yrs
Male	14/20 (70%)
Heart Rate	64.8 ± 13.6 BPM
BMI	25.6 ± 3.9 kg/m^2
LVEF	53 ± 14 %
LGE Positive	8/20 (40%)
Diabetes	6/20 (30%)
Hypertension	9/20 (45%)
Smoking	8/20 (40%)
Heart Failure	11/20 (55%)
Prior History of CAD	9/20 (45%)

Table 5.1. Summary of patient characteristics relevant for this study. BMI: body mass index; LVEF: left ventricle ejection fraction; CAD: coronary artery disease.

5.2.2) MRI Hardware

LGE MRI scans were conducted on a 1.5T whole-body MRI scanner (MAGNETOM Avanto, Siemens Healthineers, Erlangen, Germany), equipped with a gradient system capable of

achieving a maximum gradient strength of 45 mT/m and maximum slew rate of 200 T/m/s. Body coil was used for radio-frequency excitation. Both body matrix and spine coil arrays (15-18 elements) were used for signal reception.

5.2.3) Pulse Sequence

As part of the routine clinical cardiovascular MRI, single-shot, b-SSFP LGE with Cartesian k-space sampling was performed using the following relevant imaging parameters, including: field of view (FOV) = 380 mm x 345 mm, image acquisition matrix size = 176 x 128, spatial resolution = 2.2 mm x 2.7 mm, slice thickness = 6 mm, TR = 2.4 ms, TE = 1.0 ms, flip angle = 40º, GRAPPA (36) R = 1.8, k-space lines per image = 76, readout duration (without inversion recovery time) = 182 ms, and inversion time (TI) ranged from 275 to 330 ms.

As shown in Figure 5.1, we modified an inversion-recovery, single-shot b-SSFP pulse sequence with radial k-space sampling to acquire data continuously during free breathing after the inversion pulse at mid diastole in the first heartbeat through early systole of the next (second) heartbeat. This unit with two heartbeats per slice is repeated for all slices thereafter. Thus, the proposed multi-frame, single-shot LGE has the same data acquisition efficiency as conventional single-shot LGE, since the latter employs electrocardiogram (ECG) triggering every other heartbeat. The relevant imaging parameters of our pulse sequence included: FOV = 300 x 300 mm, matrix size = 224 x 224, nominal spatial resolution = 1.3 mm x 1.3 mm, slice thickness = 8 mm, TR = 3.1 ms, TE = 1.6 ms, 11 k-space rays per frame, readout duration per frame = 34.1 ms, 32.038º angular increments (= 5^{th} Fibonacci sequence of golden angles (109)), 20 time frames with a total readout duration = 694 ms, flip angle = 45º, ramp-up radio-frequency (RF) pulses = 20, inversion recovery time before readout = 62 ms, effective TI range = 85 ms to 733 ms, and effective

ECG triggering every other heartbeat. The free inversion-recovery time of 62 ms is short enough to guarantee that the magnetization in the remote myocardium relative to equilibrium magnetization is below zero prior to readout.

Our proposed cine LGE acquisition guarantees sampling the negative and positive points along longitudinal magnetization (M_z) recovery curve for the remote myocardium. This is important, since we do not want to miss the nulling point for the remote myocardium. The Bloch equation describing the relaxation of M_z following an inversion pulse with perfect efficiency can be described as:

$$M_z(t) = M_0 - [M_0 - M_z(0)]e^{-t/T_1} = M_0(1 - 2e^{-t/T_1}) \quad \textbf{Eq. 5.1}$$

Where M_0 is equilibrium magnetization. For convenience, we can normalize M_z by M_0, such that $M_z/M_0 = \left(1 - 2e^{-t/T_1}\right)$. Post-contrast T_1 of normal myocardium depends on several factors, including field strength, contrast agent type and dose, renal function, and delayed imaging time. If we assume post-contrast T_1 of normal myocardium is 400 ms (110), then the inversion time (TI) needed to null remote myocardium would be 277 ms, which is 4.5 times longer than the free magnetization recovery period of 62 ms (i.e. between the inversion pulse and readout module). Alternatively, we can calculate M_z/M_0 at t = 62 ms, which turns out to be -0.7. This confirms that the M_z/M_0 of remote myocardium before the first excitation RF pulse is a negative value. We can repeat the exercise for M_z/M_0 immediately after the readout (i.e. t = 62+682 ms). Let's assume free inversion recovery through readout (i.e. ignoring excitation pulses on magnetization recovery), then M_z/M_0 at t = 744 ms is equal to 0.7.

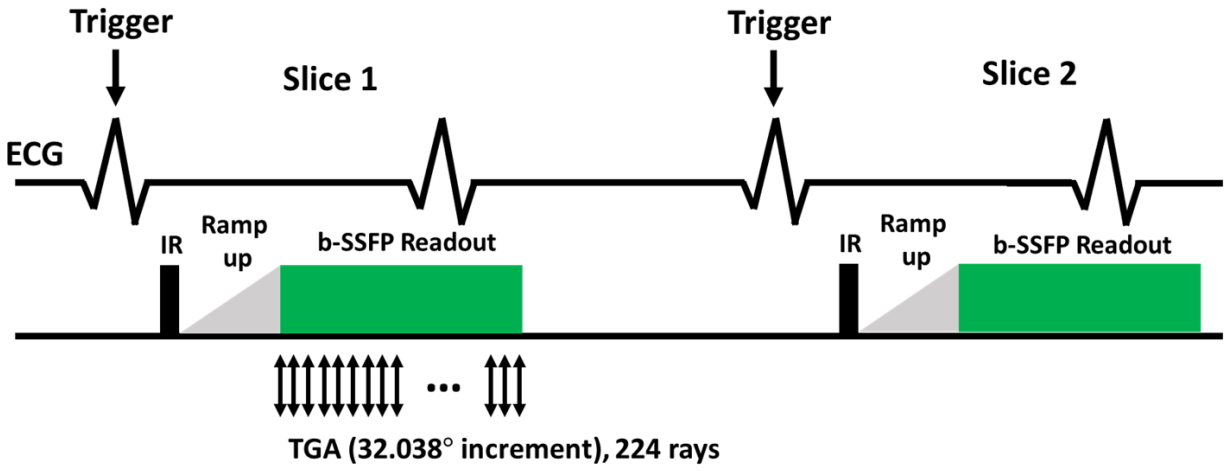

Figure 5.1. Pulse sequence diagram for the proposed multi-TI LGE. Each slice data acquisition takes two heartbeats, where 224 radial spokes of k-space data were acquired continuously (694ms) from end-diastole of the first heartbeat to early systole of the second heartbeat. The effective TI ranges from 85 to 733 ms. IR: inversion pulse; ramp-up: 20 RF pulses; b-SSFP: balanced steady state free precession.

5.2.4) Image Reconstruction

We used the GRASP-Pro (golden-angle radial sparse parallel imaging with improved performance) framework described by Feng, L et al.(111). Image reconstruction was performed off-line using a GPU workstation (Tesla V100 32GB memory, NVIDIA, Santa Carla, California, USA; 32 Xeon E5-2620 v4 128 GB memory, Intel, Santa Clara, California, USA) equipped with MATLAB (R2017b, The Mathworks Inc, Natick, MA, USA) running on a Linux operating system (Ubuntu16.04).

As shown in Figure 5.2, we applied coil compression on raw k-space data using principal component analysis (PCA)(112) to produce 8 virtual coils and used GPU-based Non-Uniform Fast Fourier Transform (NUFFT)(113) to accelerate the computation throughout. During the pre-

processing step, we used NUFFT to reconstruct time-averaged (i.e. using all 224 radial spokes) images for each coil to derive auto-calibrated coil sensitivity profiles using the method described by Walsh et al. (89). We applied self-calibrated gradient delay correction on radial k-space data using the RING method (114) and rebinned the "single-shot" data into 20 time frames (i.e. 11 radial spokes per frame). KWIC filter (106, 115) was applied to the rebinned radial k-space data to filter out the center of k-space for all but the central radial spoke per frame, which in turn enables a unique TI per frame.

For the GRASP-Pro reconstruction steps, the center 1/4 k-space (112 out of 448 readout points) was used to reconstruct the low resolution images to estimate K (=10) dominant basis components. The estimated basis, full-resolution k-space data and self-calibrated coil sensitivity profiles were combined to reconstruct the zero-filled images in the subspace. Iterative CS reconstruction was performed in the subspace by enforcing sparsity along the time dimension. The basis was applied to the CS reconstructed images in the subspace to get the final full-resolution images.

In the iterative CS process, temporal total variation (TTV) and temporal PCA (TPCA) were used as two orthogonal sparsifying transforms and nonlinear conjugate gradient with back-tracking line search as the optimization algorithm with 30 iterations. The normalized regularization weight was determined empirically to achieve a good balance between artifact suppression and temporal blurring based on visual inspection on training data. We established 0.005 (or 0.5% of maximum value of the time-averaged image) as an optimal regularization weight for TTV and 0.0025 for TPCA by sweeping over a range from 0.001 to 0.005 (0.0005 steps) and identifying the highest regularization weight that minimizes temporal blurring of voxels in the heart.

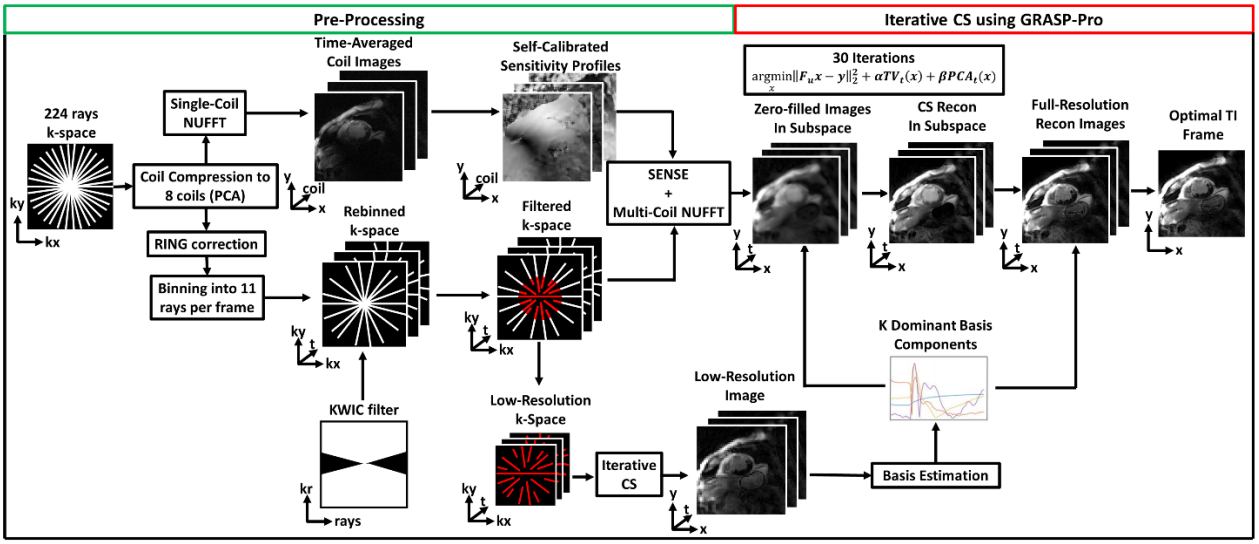

Figure 5.2. The image reconstruction pipeline of multi-TI LGE for a single slice. All 224 k-space radial spokes were used to generate self-calibrated coil sensitivity profiles and rebinned into 20 time frames (11 rays per frame). In the pre-processing step, SENSE is used to combine multi-coil zero-filled images derived after NUFFT. KWIC filter was applied to the sorted k-space to further reduce the contrast contamination. GRASP-Pro framework was used to de-aliasing zero-filled images. TV: total variation; PCA: principal component analysis; KWIC: k-space weighted image contrast; α: regularization weight for TV; β: regularization weight for PCA.

5.2.5) Quantitative Metrics of Image Quality

Only the optimal TI frame that nulls the remote myocardium was evaluated. For evaluation of image blurring of the CS reconstructed LGE images versus clinical standard LGE images, we calculated the reference-image-free blur metric, as previously described (116). For a fair comparison, we cropped the FOV of CS and clinical standard LGE images to be the same size, and interpolated the clinical images to have the same matrix size of CS by zero-filling the k-space (i.e. sinc interpolation).

5.2.6) Myocardial Scar Quantification

In eight patients with visibly detectable scars, one rater (AP) quantified myocardial scar volume using thresholding by four standard deviations above the mean of remote myocardium with manual correction to remove spurious voxels (117). This rater was blinded to patient identity and pulse sequence type.

5.2.7) Visual Metrics of Image Quality

To evaluate the diagnostic confidence of the CS reconstructed LGE images, a total of 40 multi-slice LGE data sets (20 each for clinical standard and CS) were randomized and de-identified for visual analysis by two cardiothoracic radiology attendings (BDA and LMG, both with 3 years of experience, respectively) and one non-invasive cardiology attending (DCL with 20 years of experience) who read cardiovascular MRI as part of their clinical practice graded the image quality of LGE images. The three raters were given training images to calibrate their scores in consensus prior to independent grading. The three raters were blinded to patient identity, pulse sequence type, and each other's scores. Each multi-slice set was graded on a 5-point Likert scale for: conspicuity of myocardium or scar (if visible)(1 = nondiagnostic, 2 = poor, 3 = clinically acceptable, 4 = good, 5 = excellent), any visible artifact on the heart (1 = nondiagnostic, 2 = poor, 3 = clinically acceptable, 4 = mild, 5 = minimal), and noise (1 = nondiagnostic, 2 = severe, 3 = clinically acceptable, 4 = mild, 5 = minimal). Summed visual score (SVS) was calculated as the sum of conspicuity, artifact, and noise scores (SVS $\geq$ 9 defined as diagnostically interpretable).

5.2.8) Statistical Analysis

The statistical analyses were conducted by one investigator (DS) using MATLAB. We tested for normality of variables using the Shapiro-Wilk test. Continuous data were reported as mean ± standard deviation; ordinal data were reported as median and interquartile range (IQR);

25^{th} percentile, 75^{th} percentile. Normally distributed variables were compared using a two-tailed, paired t-test for two groups and ANOVA for three groups, whereas the corresponding non-parametric variables were compared using the Wilcoxon signed rank test and Kruskal-Wallis test, respectively. For comparison with three groups, Bonferroni correction was applied. Inter-rater reliability was calculated using the Fleiss kappa test. A $p < 0.05$ was considered significant for each statistical test.

5.3) Results

According to Shapiro-Wilk test, all variables were normally distributed, except for the visual scores (statistic =0.976, p=0.87 for clinic standard; statistic = 0.974, p = 0.83 for CS). The mean offline image reconstruction time for CS LGE was 134s per slice (pre-processing step = 36s, iterative CS reconstruction = 98s). The blur metric (0: sharpest, 1: blurriest) for clinical LGE (0.325 ± 0.031) and CS LGE (0.289 ± 0.032) was significantly different ($p < 0.001$) between the two groups.

Figure 5.3 shows representative multi-TI LGE images for a single slice with different time frames, where each time frame corresponding to a different TI showing different tissue contrasts, similar to a TI scout. The TIs were calculated as the acquisition time of the central radial spoke per frame. The best TI frame was visually selected (i.e. time frame 6 in Figure 5.3). Compared to conventional LGE images, multi-TI LGE provides extra information for identifying borders of scar. As shown in Figure 5.3, the regions pointed by the yellow arrows in frames 3 and 5 are helpful in determining the boundaries of remote myocardium and scar. Figure 5.4 shows representative clinical single-shot LGE images and CS LGE images for 4 patients, where the yellow arrows point

to scar regions. For average rater, the median scores for all three categories were significantly different ($p<0.05$) between the two groups, but all scores were greater than clinically acceptable (3.0) cut point for both clinical standard and CS LGE.

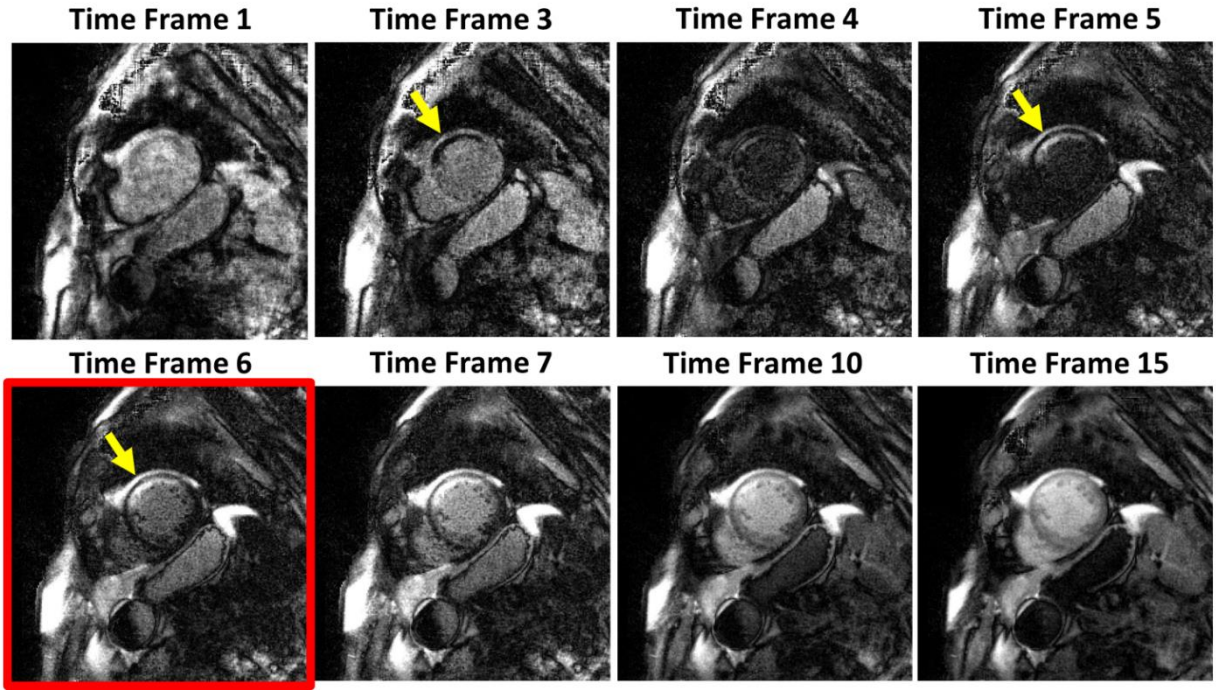

Figure 5.3. An example of different TI frames for a single slice. This time series appearance is like that in a TI scout but with a better temporal resolution. For this case, time frame 6 had the best nulling of normal myocardium.

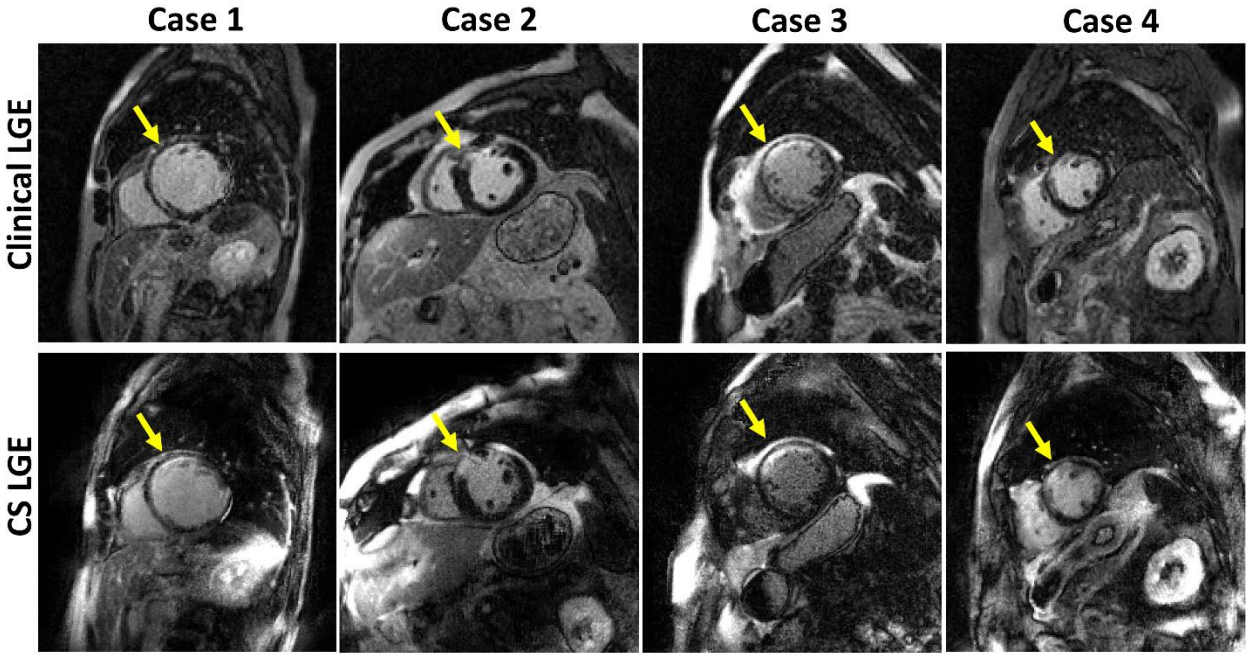

Figure 5.4. Four representative cases of with myocardial scarring: clinical single-shot LGE (top row) versus CS LGE at the optimal TI (bottom row). Arrows point to scars.

According to weighted Fleiss's kappa coefficient, inter-rater reliability in grading CS LGE was poor for conspicuity (κ=-0.108; 95% CI, -0.153 to -0.062), artifact (κ=-0.175; 95% CI, -0.218 to -0.132) and noise (κ=-0.148; 95% CI, -0.198 to -0.097) scores. Inter-rater reliability in grading clinical standard LGE was poor for both conspicuity (κ=-0.048; 95% CI, -0.096 to 0.0003) and noise (κ=-0.126; 95% CI, -0.177 to -0.076) scores and slight for artifact (κ=0.099; 95% CI, 0.050 to 0.149) scores.

The remaining visual analysis results represent average rater scores. According to the Wilcoxon signed rank test (see Table 5.2), conspicuity was significantly higher for clinical standard LGE (median: 4.7, IQR: 0.7) than CS LGE (median: 4.0, IQR: 0.67); artifact was significantly lower (i.e. better score) for clinical standard (median: 4.7, IQR: 0.67) than CS LGE (median: 4.0, IQR: 0.67); noise was significantly lower for clinical standard (median: 4.3, IQR:

0.42) than CS LGE (median: 3.7, IQR: 0.67); SVS was significantly higher for clinical standard LGE (median: 13.3, IQR: 1.83) than CS LGE (median: 12.0, IQR: 0.75).

Myocardial scar volume measured from clinical standard LGE (18.3 ± 7.3 %) and CS LGE (17.6 ± 6.6 %) was not significantly different ($p > 0.4$); scar volume was strongly correlated (coefficient of determination [R^2] =0.91) and in good agreement (mean difference = -0.7 % [3.9% of mean], lower limit of agreement = -5.11% [28.4% of mean], and upper limits of agreement = 3.71% [20.6% of mean]), shown in Figure 5.5.

Category	Clinical LGE	CS LGE	p-Value
Conspicuity	4.7 (0.75)	4.0 (0.67)	< 0.001
Artifacts	4.7 (0.67)	4.0 (0.67)	< 0.001
Noise	4.3 (0.42)	3.7 (0.67)	< 0.001
SVS	13.3 (1.83)	12.0 (0.75)	< 0.001

Table 5.2: Summary of visual scores. Reported values represent median and interquartile range (parenthesis) of average rater scores. While all scores were significantly different ($p < 0.05$) between the two groups, all were above the clinically acceptable cut point (3 for individual category; 9 for SVS). SVS: summed visual scores.

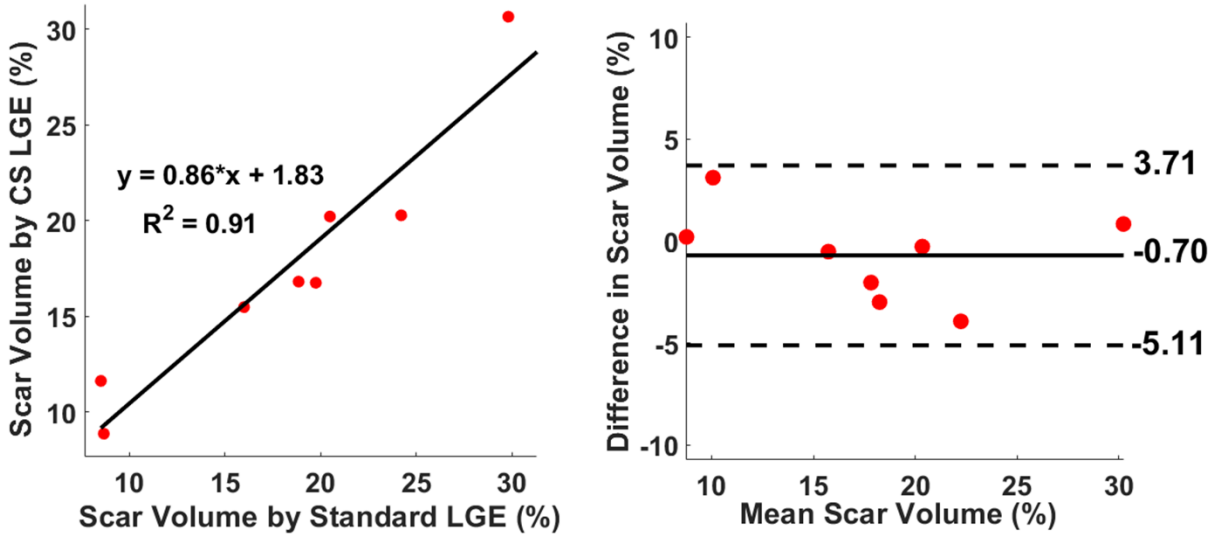

Figure 5.5. Linear regression plot illustrating strong correlation (R^2=0.91) in scar volume measurements between clinical standard and CS LGEs (left). Bland-Altman plot illustrating good agreement in scar volume measurements between the two methods.

5.4) Discussion

This study demonstrates a novel free-breathing, single-shot LGE sequence with high nominal spatial resolution and multi-TI reconstruction using GRASP-Pro. Our approach allows for direct free-breathing scans without a TI scout and provides clinically acceptable image quality. Myocardial scar volume measurement made from our CS LGE images was as accurate as measurement made from clinical standard LGE images.

Our approach has several differences compared with free-breathing LGE with MOCO (105). The method developed by Kellman et al. (105) is based on averaging repeated single-shot LGE with MOCO to increase spatial resolution and/or signal-to-noise ratio. One advantage of this

approach is that it is compatible with phase-sensitive (PSIR) reconstruction, thereby providing some wiggle room with respect to TI selection by a technologist. Two disadvantages of this approach are that it is sensitive to irregular heart rhythm and/or bulk motion and that it requires longer scan (increases with averaging factor). While our multi-TI approach does not perform PSIR reconstruction, it is designed to generate multiple TI images without relying on a TI scout. Our approach does not rely on averaging; thus it is faster than PSIR LGE MOCO in terms of scanning efficiency. Our approach does not rely on MOCO; thus it is not subject to image deformation errors inherent with MOCO.

This study has several interesting points that warrant further discussion. First, as the technique does not require a TI scout, it improves clinical workflow and has the potential to avoid poor image contrast due to incorrect TI selection, similar to PSIR. Second, we acquired near Nyquist number of radial spokes (i.e. 224 rays), which produced better self-calibrated coil sensitivity map than traditional 2D undersampled reconstruction method. Sorting the k-space data in the time dimension increased the temporal resolution, thus minimizing motion blurring, as well as improved CS reconstruction performance. Third, the multi-TI information can potentially increase the accuracy in identifying myocardial scar borders, which may increase accuracy in scar quantification. Fourth, the multi-TI contrast may be helpful for automated segmentation tools. Finally, the multi-TI information (longest TI = 733 ms) can provide a means to detect thrombus without performing another LGE scan with a longer TI (~600 ms).

This study has several limitations that warrant further discussion. First, only eight patients in this study had visible scars, which may have influenced the definition of conspicuity. Second, several factors may have led to differences between clinical standard LGE and CS LGE: a) pulse

sequence order, where CS LGE (slightly less gadolinium) was acquired after the clinical LGE; b) slice thickness (6 mm for clinical vs. 8 mm for CS LGE) and c) the effect of different window leveling in the DICOM viewer. Third, the optimal TI frame was retrospectively selected manually. Future study includes automated TI selection using a deep learning approach, as previously described (118). Finally, we did not incorporate the value of multi-TI information for visual scores, since such analysis will reveal which pulse sequence is which and bias raters; we anticipate that multi-TI reconstruction will increase diagnostic confidence for identifying scar borders and small infarcts and peri-infarct zones (see Figure 5.3).

In summary, this study describes development and evaluation of a high resolution, free-breathing LGE pulse sequence using radial k-space sampling, CS, and KWIC filtering, without significant loss in image quality and myocardial scar quantification, thereby verifying clinical potential.

Chapter 6: Perceptual Complex Neural Network for reconstructing radial cine k-space data

6.1) Introduction

While electrocardiogram-gated, breath-hold cine MRI with balanced steady-state free precession readout is the reference test for evaluation of cardiac function (119, 120), its diagnostic yield may be limited in patients with arrhythmia and/or dyspnea due to severe image artifacts. One approach to overcome this limitation is to perform highly-accelerated real-time cine MRI using compressed sensing (CS)(37) with Cartesian (16, 121) or radial k-space sampling (40, 107). The three key components of CS are sparsity, incoherent aliasing artifacts, and nonlinear optimization with L1-norm. Despite promising results using CS-accelerated real-time cine MRI, its lengthy image reconstruction time may hinder its clinical translation, including interventional or stress testing MRI where real-time support is critical. Thus, there is an unmet need to develop highly-accelerated image reconstruction methods that support accelerated, real-time cine MRI acquisitions.

One solution to accelerating CS reconstruction is using graphics processing unit (GPU), however the acceleration is limited since CS remains iterative and nonlinear. To circumvent the problem of computation-intensive iterations, feed-forward deep learning (DL)(45) has emerged as a promising alternative for solving inverse problems compared to iterative approaches (122-124). DL-based image reconstruction is roughly categorized into agnostic, decoupled physics-based and post-processing learners. Agnostic solvers learn a direct mapping from input to output domain without any knowledge of the forward model at any point in training nor testing (125). Agnostic

solvers require huge amount of training data and are hard to optimize. Decoupled approaches first learn a comprehensive representation of the image space independent of the imaging problem at hand, e.g. from a large set of reconstructed MRI images. This knowledge is then used to guide the image reconstruction (126). Physics-based learners incorporate a differentiable version of the imaging operator (e.g. the Fourier transform in MRI imaging) into the training process and reduce the amount of required training data drastically (127, 128).

Last there remain learners that focus on post-processing to remove possible artifacts that arise in non-iterative algorithms (129, 130). The key advantage of this approach is that it is simpler to implement. The basic strategy is to train a network to learn the weights (convolutional kernels) for de-aliasing undersampled MR images from a large dataset containing pairs of aliased and de-aliased images. In the testing phase, the network applies the "learned" model to de-alias images from a separate testing dataset. While the training phase is computationally intensive due to backpropagation of gradients and often requires GPU computing, the testing phase is significantly faster than CS, could even be transferred with CPU computing, thereby making it a good vehicle to reduce the processing time of reconstructing accelerated real-time cine MRI.

To date, two proof-of-concept studies have used DL to reconstruct real-time cine MR data, with each study having advantages and disadvantages (54, 61). In this study, we sought to develop a novel DL approach that goes beyond two prior studies (54, 61). Our main contributions are:

(a) Implementing a complex neural network that is capable of learning correlated and uncorrelated (i.e. noise) information contained in real and imaginary components of complex MRI signal detected in quadrature (i.e. 90° phase offset between real and imaginary components, as shown in Figure 6.1);

(b) Incorporating a perceptual loss term to maintain high-level features better than per pixel loss, as previously described (131);

(c) Training and testing the proposed network with multi-slice data from a larger group (40 in total; 20 for training, 20 for testing) of patients with atrial fibrillation (AF), which has not been addressed by previous DL-based image reconstruction studies;

(d) Handle highly-accelerated (15-fold) cine data. Our approach to handling complex data in the image domain is different than prior studies which handled complex data, either in the image domain as magnitude and phase (132) or in the k-space domain (125, 133). The key advantage of the proposed approach over previous approaches is that it does not require extensive GPU memory (i.e. fast processing), because it handles coil-combined complex data without requiring fully connected layers or fidelity layers.

The purpose of this study was to implement a perceptual complex neural network (PCNN) for faster (< 1 min per slice with 80 frames) reconstruction of non-Cartesian real-time cine MRI k-space data than GPU-accelerated CS reconstruction, without significant loss in image quality or accuracy in left ventricular (LV) functional parameters. We compare the proposed PCNN to previously proposed CNN network architecture (61) for completeness.

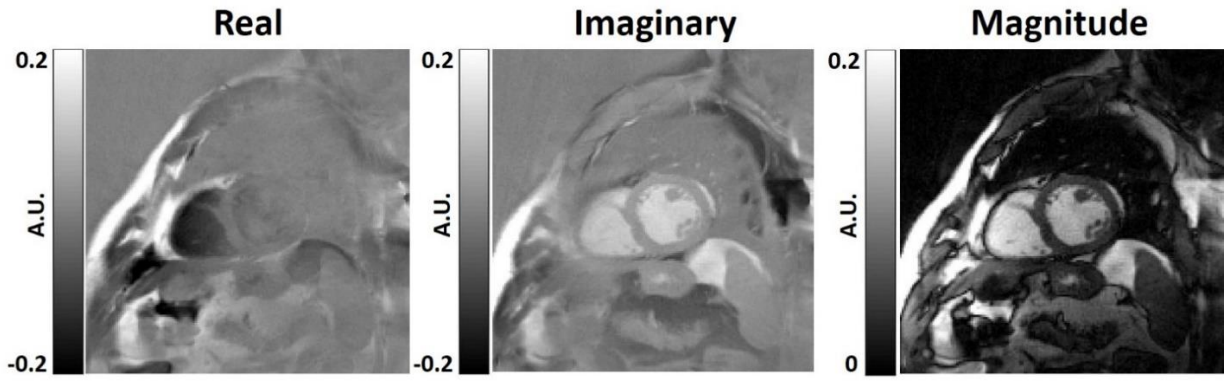

Figure 6.1. Real (left), imaginary (middle), and magnitude (right) parts of a real-time cine complex MR image, illustrating correlated and uncorrelated (noise) information detected using a quadrature radio-frequency receiver system.

6.2) Materials and Methods

6.2.1) Patient Demographics

This study was conducted in accordance with protocols approved by our institutional review board and was Health Insurance Portability and Accountability Act (HIPAA) compliant. All subjects provided informed consent in writing. We prospectively enrolled forty patients with prior history of AF (mean age = 68.1 ± 9.6 years; 31 males; 9 females). In eight out of twenty patients (mean age = 68.6 ± 10.6 years; 16 males; 4 females) used for training, MRI was repeated within two weeks to evaluate test-retest reproducibility for a separate study, such that twenty-eight sets of multi-slice, multi-phase cine k-space datasets were used for training. Multi-slice, multi-phase datasets from the remaining twenty patients (mean age = 67.6 ± 8.7 years; 15 males; 5 females) were used for testing the trained neural networks. We elected to reserve data from twenty patients for testing, in order to achieve high power for our statistical analysis. For basic

demographics information of our patients including age, sex, AF type, and resting heart rate, see Table 6.1. Other clinical characteristics were considered irrelevant for this study and thus omitted due to space constraint. To estimate the arrhythmia burden during MRI, we calculated the coefficient of variation (CV) of heartbeat duration, which was extracted from the raw data header of real-time cine running continuously for multiple heartbeats per slice, for multiple slices (total scan time was ~60s).

	Total	Training	Testing
Age (years)	68.1 ± 9.6	68.6 ± 10.6	67.6 ± 8.7
Sex	31M/9F	16M/4F	15M/5F
Resting Heart Rate (bpm)	66.7 ± 12.0	68.2 ± 12.9	65.3 ± 11.1
AF type	32 Paroxysmal / 8 Persistent	15 Paroxysmal / 5 Persistent	17 Paroxysmal / 3 Persistent
Arrhythmia burden (%)	24.6 ± 9.3	26.5 ± 9.8	22.8 ± 8.6

Table 6.1. Summary of baseline patient characteristics (N=40). M: males; F: females; AF: Atrial Fibrillation.

6.2.2) MRI Hardware

Real-time cine scans were conducted on one 1.5T whole-body MRI scanner (MAGNETOM Aera, Siemens Healthcare, Erlangen, Germany). The scanner was equipped with a gradient system capable of achieving a maximum gradient strength of 45 mT/m and maximum

slew rate of 200 T/m/s. Body coil was used for radio-frequency excitation. Both body matrix and spine coil arrays (30-34 elements in total) were used for signal reception.

6.2.3) Pulse Sequence

Relevant imaging parameters of real-time cine MRI using radial k-space sampling included: field of view (FOV) = 288 × 288 mm, matrix size = 160 × 160, spatial resolution = 1.8 mm x 1.8 mm, slice thickness = 8 mm, TE = 1.4 ms, TR = 2.7 ms, receiver bandwidth = 975 Hz/pixel, 11 radial spokes per cardiac frame, tiny golden angle sequence = 23.62814° (30), effective acceleration factor = 15 (with respect to Cartesian equivalent), temporal resolution = 29.7 ms, 12-17 short-axis planes, and flip angle 50°. Although each 2D plane was scanned for 5 seconds during free-breathing, only the first 80 out of 166 cardiac frames were used from each patient due to GPU memory limitation.

6.2.4) Computer Hardware

For training and testing on undersampled raw k-space data, we used a GPU workstation (Tesla V100 32GB memory, NVIDIA, Santa Carla, California, USA; 32 Xeon E5-2620 v4 128 GB memory, Intel, Santa Clara, California, USA) equipped with Python (Version 3.7, Python Software Foundation), Pytorch (Version 1.4, Berkeley Software Distribution), and MATLAB (R2017b, The Mathworks Inc, Natick, MA, USA) running on a Linux operating system (Ubuntu16.04).

6.2.5) GPU-Accelerated CS Reconstruction as Ground Truth

In patients with AF, standard electrocardigram-gated breath-hold cine MRI produces poor image quality with considerable ghosting and blurring artifacts. Thus, it was not feasible to obtain

fully sampled reference for this study. Instead, we used CS reconstruction as obtainable ground truth.

For reference, the same undersampled k-space data were reconstructed using the same GPU workstation. We adapted our previously described radial CS reconstruction code implemented in MATLAB (107) with two modifications: (a) GPU based Non-Uniform Fast Fourier Transform (NUFFT)(113) and (b) coil compression using principal component analysis (PCA)(112) to produce 8 virtual coils. In the preprocessing step (gradient delay correction + gridding + coil combination), we performed self-calibrated gradient delay correction using the Radial Intersections (RING) method (114), GPU based NUFFT to convert the radial k-space data to zero-filled images in Cartesian space, and additional processing on time average image to derive auto-calibrated coil sensitivity profiles using the method described by Walsh et al. (89), followed by weighted sum over the coil elements. Coil-combined, zero-filled cine images (initial solution), multi-coil raw k-space data, k-space sampling masks, and coil sensitivity maps were used as inputs to previously described iterative CS algorithm (107), which enforced sparsity along the time dimension using temporal finite difference (temporal total variation) as the sparsifying transform and nonlinear conjugate gradient with back-tracking line search as the optimization algorithm with 30 iterations. The cost function used is described in Eq. 6.1:

$$\hat{x} = argmin_x \|FSx - y\|_2^2 + \lambda |Tx|_1 \qquad \textbf{Eq. 6.1}$$

where, F is the undersampled FFT operator, S is the estimated coil sensitivities in *x-y* space, x is the image series to be reconstructed in *x-y-t* space, y is the acquired multi-coil k-space data, T is temporal finite difference operator, and λ is the normalized regularization weight that controls the tradeoff between data consistency and sparsity terms. We incorporated back-tracking

line search to ensure high data fidelity, at the expense of computational efficiency. Normalized regularization weight was set as 0.1 of the maximum signal of time average image. We established 0.1 (relative to maximum value) as optimal regularization weight by sweeping over a range from 0.001 to 0.1 (0.05 steps) and identifying an optimal regularization weight that achieves a good balance between suppression of aliasing artifacts and temporal blurring of myocardial wall motion. We determined this optimal regularization weight based on visual inspection of six training datasets.

6.2.6) Network Architecture

We implemented a reconstruction pipeline that performs pre-processing in Matlab and dealiases coil-combined images in Pytorch. We elected to work with coil-combined images due to GPU memory limitation. After the same pre-processing step described for CS, coil-combined, zero-filled, complex images used as input. Our network was trained on 398 2D+time sets of zero-filled, real-time cine images obtained from twenty patients (eight in whom we obtained another set of cine data), corresponding to 31,840 2D images in total. The trained network was tested on 275 2D+time sets of zero-filled, real-time cine images obtained from the remaining twenty patients, corresponding to 22,000 2D images in total.

By modifying the network and loss function, we explored three different ways of processing the complex data to achieve optimal image quality, as shown in Figure 6.2. Three different residual 3D (2D + time) U-Nets (50, 52, 134, 135) with identical architecture but different loss function were tested: 1) magnitude network with mean squared error (MSE) loss alone, which uses traditional operations (convolution, rectified linear unit (ReLU), etc.) to process absolute value of the complex data; 2) complex network with MSE loss alone, which uses complex

operations to process the complex data (see below and Figure 6.3 for more details); 3) PCNN using both complex operations and MSE and perceptual loss terms. For complex networks (2 and 3), the batch normalization and ReLU layers had separate weights for the real and imaginary feature maps, while the pooling layers were the same. For PCNN, instead of using MSE loss alone (62, 136, 137), we added a perceptual loss (50, 138) using the first 15 layers of a pre-trained Visual Geometry Group (VGG)-16 network (139) to maintain high-level features better than pixel-wise MSE loss. Only the first 15 layers of VGG-16 network were used to extract features, since the last layer is used for classifying features. The total loss function can be described by Eq. 6.2:

$$Loss_{total} = \frac{1}{N}\|\varphi(x) - y\|_2^2 + \frac{1}{N}\left\|f_{vgg}(x) - f_{vgg}(y)\right\|_2^2 \quad \textbf{Eq. 6.2}$$

where φ is the U-Net, f_{vgg} is the VGG network, N is the total number of voxels, x is the zero-filled images (either real or imaginary), and y is the reference images (either real or imaginary) reconstructed with CS. For visual display of the outcome of VGG network for CS and DL, see Figure 6.4. The following training parameters were used: batch size = 1, ADAM optimizer, 50 epochs, learning rate = 0.0001 with a decay rate 0.95 for each epoch. Training for the magnitude network took approximately 8 hours, whereas training for the complex network and PCNN took approximately 20 hours and 24 hours, respectively.

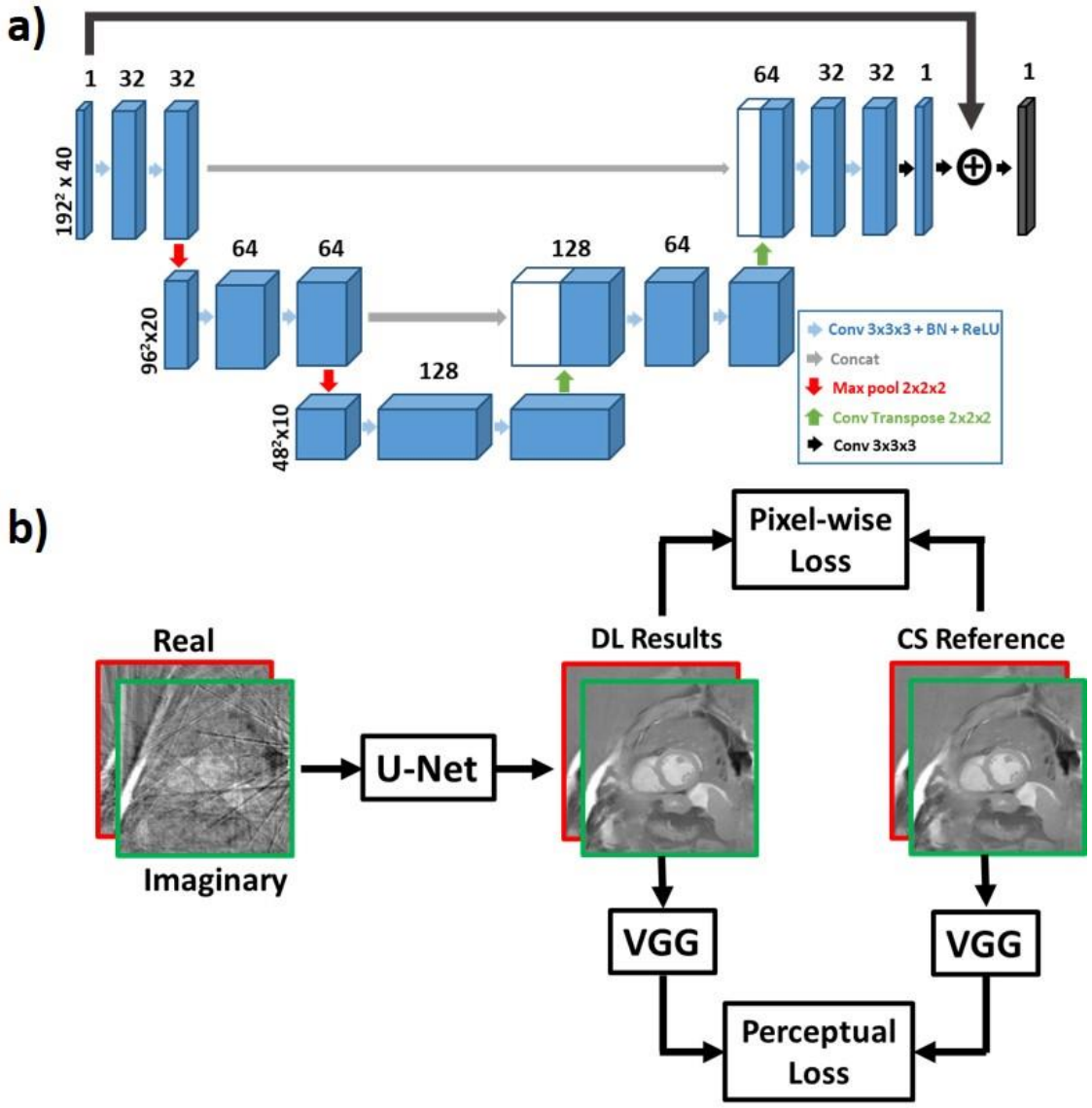

Figure 6.2. a) The U-Net architecture used for all three networks; b) the pipeline for PCNN training. The complex U-Net and PCNN used the same complex convolution operations shown in Figure 6.3. While PCNN uses both perceptual loss and pixel-wise MSE loss functions, conventional magnitude and complex U-Net used only the pixel-wise MSE loss function. For visual display of the outcome of VGG network for CS and DL, see Figure 6.4.

As shown in Figure 6.3, we performed complex convolution (140) on the complex data. To support this complex operation, we created one additional dimension for the feature maps to

carry both the real (M_R) and imaginary (M_I) parts and used two separate kernels (K_R and K_I) to perform the complex convolution as described by Eq. 6.3:

$$(M_R + iM_I) * (K_R + iK_I) = (M_R * K_R - M_I * K_I) + i(M_R * K_I + M_I * K_R) \quad \textbf{Eq. 6.3}$$

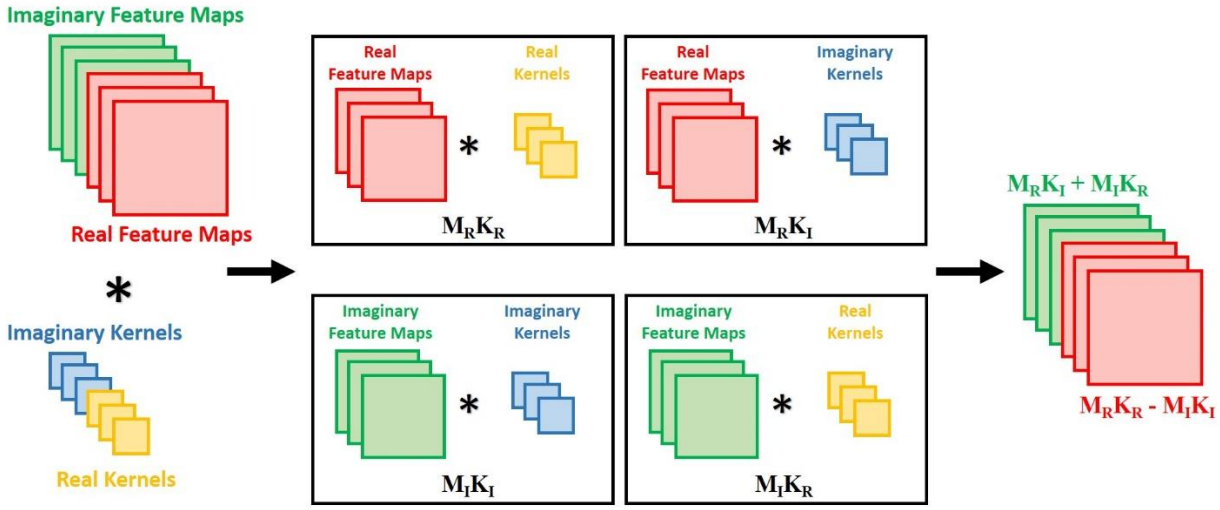

Figure 6.3. Complex convolution operation used in complex U-Net and PCNN. The real (M_R) and imaginary (M_I) feature maps are separated by creating an extra dimension and convolved with real (K_R) and imaginary (K_I) kernels as shown. The results are sorted and separated in the next layer with (M_RK_R - M_IK_I) as the real part and (M_RK_I + M_IK_R) as the imaginary part.

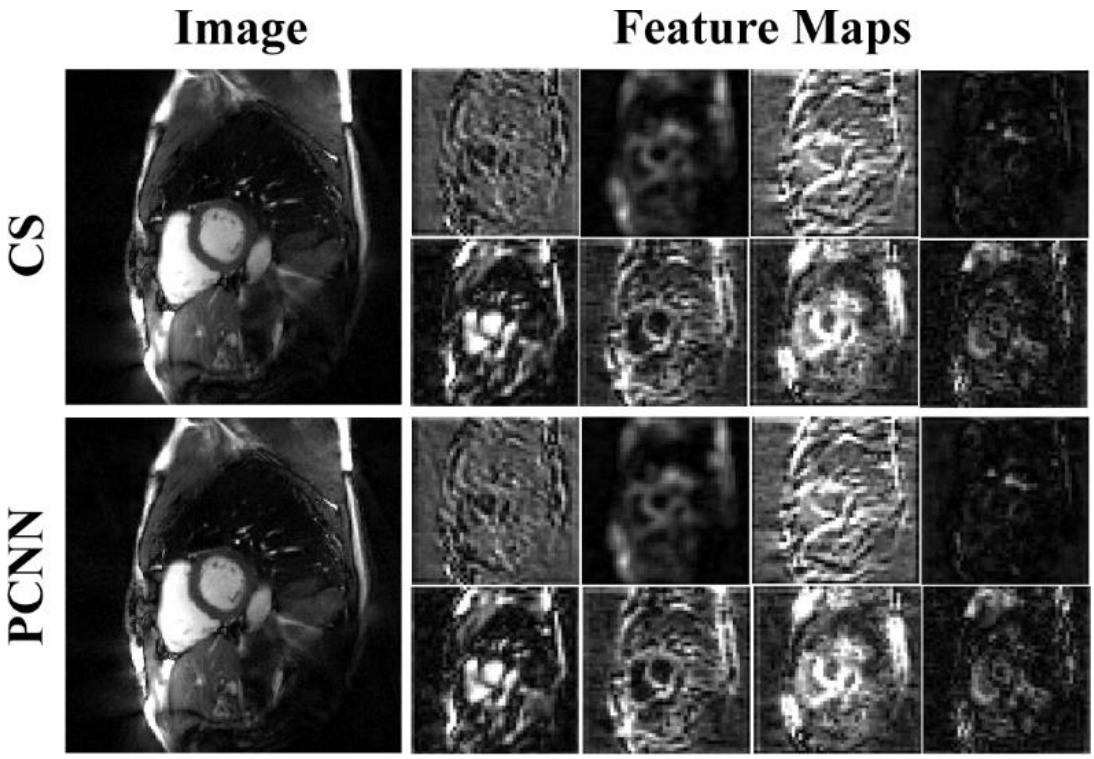

Figure 6.4. Visual display of features extracted from VGG-16 network for CS and DL. 8 out of 256 feature maps were randomly selected and shown on the right.

6.2.7) Quantitative Metrics of Image Quality

Given that images reconstructed with different methods are perfectly registered, we calculated the structural similarity index (SSIM)(141) and normalized root mean square error (NRMSE) to infer image quality with respect to reference images reconstructed with CS. For both SSIM and NRMSE calculations, we focused on a smaller region of interest (central FOV with 80x80 voxels) that encapsulates the heart region. To evaluate image blurring, we calculated the blurring metric (116) on a 0 to 1 continuous scale, where 0 is defined as sharp and 1 is defined as blurred.

6.2.8) Visual Metrics of Image Quality

To evaluate the diagnostic confidence produced by the proposed PCNN, two non-invasive cardiology attendings (DCL and BHF with 17 and 8 years of experience, respectively) graded the CS reconstructed images (reference) and best DL reconstructed images, where best among magnitude, complex, and PCNN was determined by quantitative metrics (SSIM, NRMSE, blur metric). For efficient analysis, evaluation was limited to 3 short-axis planes (base, mid, apex) only. In total, forty cine data sets (twenty sets for DL and CS each), grouped as a set of three short-axis planes, were randomized and de-identified for dynamic display. Prior to visual evaluation, the two readers were given training data sets to calibrating their scores together, where a score of three is defined as clinically acceptable. Following training, each reader was blinded to image acquisition type (CS and DL), each other, and clinical history. Each set of three short-axis planes was graded on a 5-point Likert scale: conspicuity of endocardial border at end diastole (1 = nondiagnostic, 2 = poor, 3 = adequate, 4 = good, 5 = excellent), temporal fidelity (blurring or ghosting or lack thereof) of wall motion (1 = nondiagnostic, 2 = poor, 3 = adequate, 4 = good, 5 = excellent), any visible artifact on the heart (1 = nondiagnostic, 2 = severe, 3 = moderate, 4 = mild, 5 = minimal), and apparent noise throughout (1 = nondiagnostic, 2 = severe, 3 = moderate, 4 = mild, 5 = minimal). The summed visual score (SVS) was calculated as the sum of conspicuity, temporal fidelity, artifact, and noise scores, with 12 defined as clinically acceptable.

6.2.9) LV Function Assessment

In total, forty cine data sets (20 patients x 2 [CS and best DL] sets per patient) were analyzed by another reader (AP) with 2 years of experience as a medical research fellow, using standard methods on a workstation equipped with commercial software (CVi42, Cardiovascular Imaging, Calgary, Canada). Functional parameters included LV ejection fraction (LVEF), LV end-

systolic volume (LVESV), LV end-diastolic volume (LVEDV), and LV stroke volume (LVSV). For consistency, the most basal slice was defined as the plane which has ≥ 50% of the blood pool surrounded by myocardium, and the most apical slice was defined as the plane showing blood pool at end diastole. The reader repeated the analysis with a 2-weeks gap between analyses to determine whether inter-reconstruction variability is similar to intra-observer variability.

6.2.10) Statistical Analysis

The statistical analyses were conducted by one investigator (DS) using Matlab. Using average reader scores, we used the Wilcoxon signed-rank test to detect differences between two groups. For continuous variables (SSIM, NRMSE, blur metric), we used analysis of variance to detect differences between multiple groups, with Bonferroni correction to compare each DL reconstruction to CS as reference. For cardiac functional parameters, we performed Pearson's correlation and Bland-Altman analysis to examine association and agreement. Reported continuous variables represent mean ± standard deviation. A P-value < 0.05 was considered significant for all statistical tests.

6.3) Results

The mean CV of R-R interval for the entire cohort was 24.6 ± 9.3%, while the corresponding R-R intervals for the training and testing cohorts were 26.5 ± 9.8% and 22.8 ± 8.6%, respectively, indicating moderate levels of arrhythmia. The mean processing time per slice with 80 frames along the proposed pipeline for PCNN was 23.7 ± 1.9 s for pre-processing (step 1) and 0.822 ± 0.004 s for dealiasing (step 2). The corresponding processing time along the GPU-accelerated CS pipeline was 23.7 ± 1.9 s for pre-processing (step 1) and 136.4 ± 2.4 s for dealiasing

(step 2). The reconstruction time including the identical pre-processing step for DL was 6.5 times faster than CS, whereas the dealiasing processing time (excluding the pre-processing step) for DL was 166 times faster than CS.

Figure 6.5 shows representative real-time cine reconstructed MR images obtained with the following methods: 1) CS as reference; 2) zero-filled image immediately after NUFFT; 3) magnitude network with MSE alone; 4) complex network with MSE loss alone; and 5) PCNN. The corresponding difference images with respect to CS are also shown, where the PCNN showed the least amount of residual artifacts.

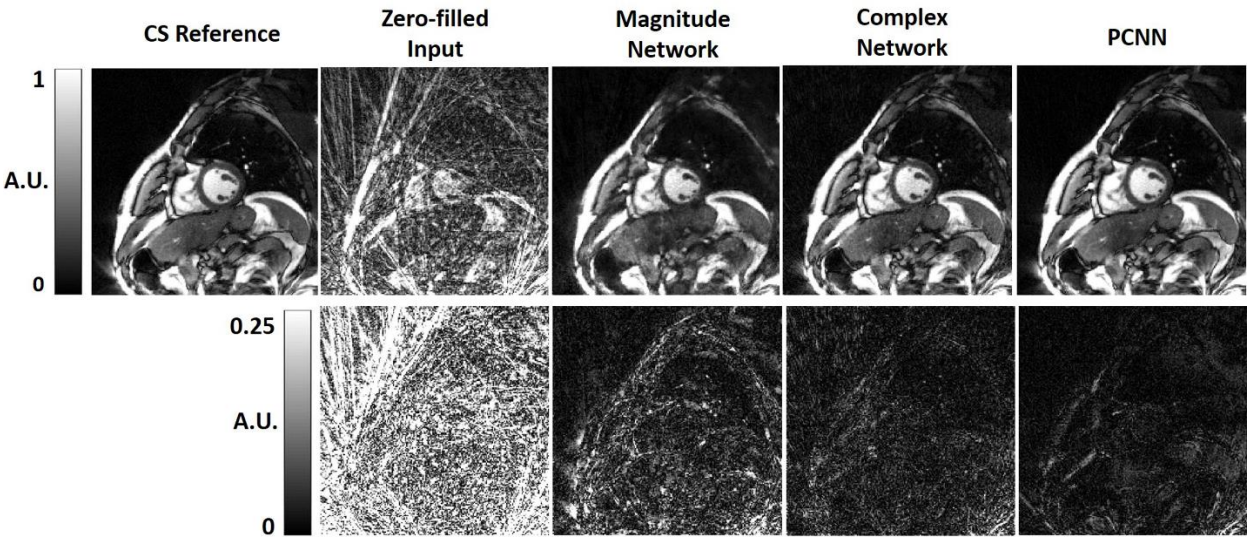

Figure 6.5. (Top row) Representative images of CS reference (first column), zero-filled image immediately after NUFFT (second column) and reconstruction results by three different networks: magnitude network (third column), complex network with MSE loss term only (fourth column), and PCNN (fifth column), displayed in 0-1.0 arbitrary units (A.U.). (Bottom row) The corresponding difference images with respect to CS reference, displayed in 0-0.25 arbitrary units to bring out differences.

Summarizing the result over twenty patients (see Table 6.2), compared with CS, the PCNN produced the best image quality metrics (SSIM = 0.88 ± 0.02, NRMSE = 0.014 ± 0.004), significantly ($P<0.05$) better than the magnitude and complex networks (SSIM < 0.75, NRMSE > 0.020). Relative to CS, the blur metrics were not significantly ($P>0.05$) different for the magnitude network and PCNN, whereas they were significantly ($P<0.05$) lower for the zero-filled and complex network. Given that PCNN produce the best results in two out of three categories, we elected to use PCNN throughout.

	CS Reference	Zero-filled	Magnitude	Complex	PCNN
NRMSE		0.082 ± 0.011	0.025 ± 0.005*	0.020 ± 0.006*	0.014 ± 0.004
SSIM		0.232 ± 0.025	0.663 ± 0.056	0.742 ± 0.069	0.884 ± 0.023
Blur Metric	$0.338 \pm 0.015^{+\in}$	0.188 ± 0.008	$0.340 \pm 0.017^{+\#}$	0.314 ± 0.019	$0.337 \pm 0.013^{\in\#}$

Table 6.2. Summary of quantitative metrics (N=20). NRMSE and SSIM for zero-filled input images and reconstruction results by three different networks compared to CS reference. For NRMSE and SSIM, $^{*}P > 0.05$ corresponds to non-significant difference in pair. For blur metric, $^{+\in\#}P > 0.05$ corresponds to non-significant difference in pair. Note, the blur metric scores for the zero-filled and complex network with MSE loss term only reconstructions are artificially better, because they contained substantial amount of streaking artifacts which have sharp edges.

Figure 6.6 shows representative images of three patients reconstructed with PCNN and CS, highlighting similar image quality. Table 6.3 summarizes average reader scores for CS and PCNN. While all the scores were significantly different ($P<0.05$) between the two groups, all individual

visual scores and SVS were well above the clinically acceptable cut points 3.0 and 12.0, respectively.

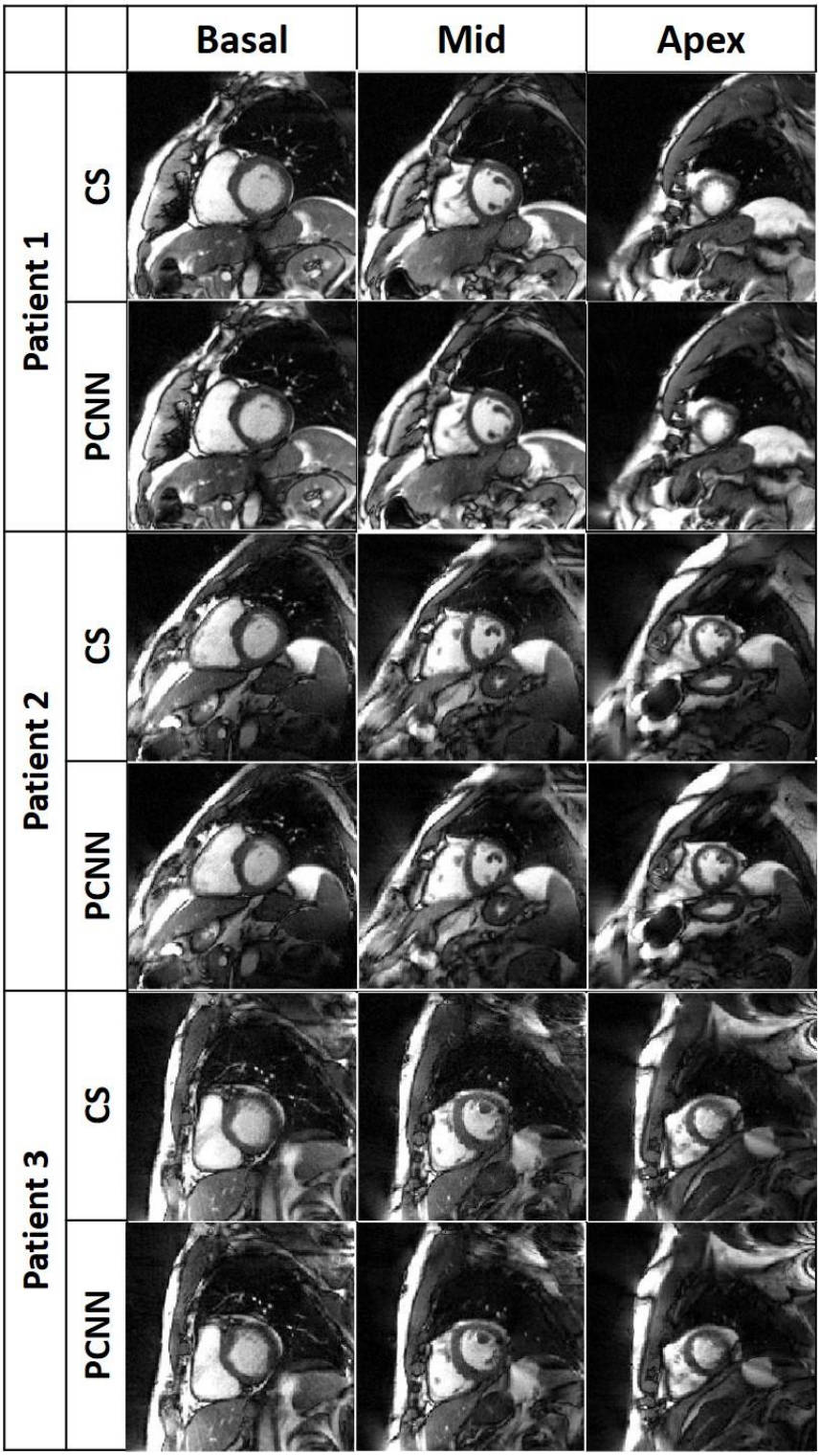

Figure 6.6. Representative images of three different patients reconstructed with CS (top row per patient), PCNN (middle row per patient), and difference image (bottom row per patient) displayed

with 4-times narrow grayscale to bring out differences: basal plane (left column), mid-ventricular plane (middle column), and apical plane (right column).

	CS	PCNN
Myocardial Edge Definition	5.0* (4.5-5.0)	4.5* (4.0-4.5)
Temporal Fidelity	4.75* (4.5-5.0)	4.0* (3.5-4.5)
Artifacts Level	4.5* (4.0-5.0)	4.25* (4.0-4.5)
Noise Level	4.5* (4.5-5.0)	4.5* (4.0-4.5)
SVS	18.75* (17.5-19.5)	17.0* (16.0-18.0)

Table 6.3. Summary of average reader visual scores. Reported values represent median and 25th to 75th percentiles (parenthesis). $^{*}P < 0.05$ corresponds to significant difference.

Figure 6.7 shows scatter plots resulting from linear regression analysis illustrating strong correlation between CS and DL analyses ($R^2 \geq 0.92$) and between repeated DL analyses ($R^2 \geq 0.93$) for all four LV functional categories. Figure 6.8 shows Bland-Altman plots illustrating good agreement between CS and DL analyses for LVEDV (mean =98.0mL; mean difference = -0.54 mL [0.5% relative to mean], the limits of agreement [LOA] = 14.5 mL [14.8% relative to mean]), LVESV (mean = 38.6 mL; mean difference =1.0 mL [2.6% relative to mean]; LOA = 11.3 mL [29.3% relative to mean]), LVSV (mean = 59.4 mL; mean difference = -1.6 mL [2.6% relative to mean]; LOA = 14.9 mL [25.0% relative to mean]), and LVEF (mean = 61.6%; mean difference =

-1.4 % [2.3% relative to mean]; LOA = 10.9% [17.6% relative to mean]). Figure 6.8 also shows good agreement between repeated DL analyses for LVEDV (mean difference = -0.9 mL [0.9% relative to mean]; LOA = 8.7 mL [8.9% relative to mean]), LVESV (mean difference = 0.9 mL [2.4% relative to mean]; LOA = 10.3 mL [26.0% relative to mean]), LVSV (mean difference = -1.8 mL [3.2% relative to mean]; LOA = 9.3 mL [16.0% relative to mean]), and LVEF (mean difference = -1.4 % [2.3% relative to mean]; LOA =10.0% [16.7% relative to mean].

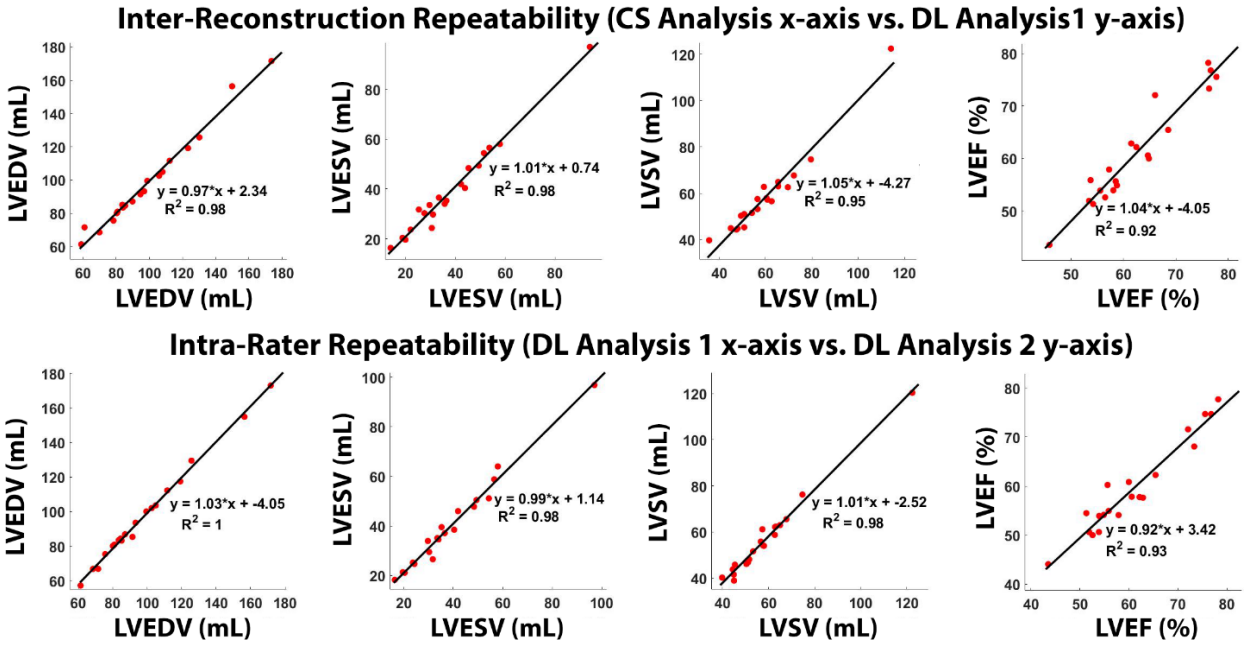

Figure 6.7. Linear regression plots illustrating strong correlation between reconstruction methods (top row, CS vs. DL, $R^2 \geq 0.92$) and between repeated DL analyses (bottom row, $R^2 \geq 0.93$) for all four LV functional parameters.

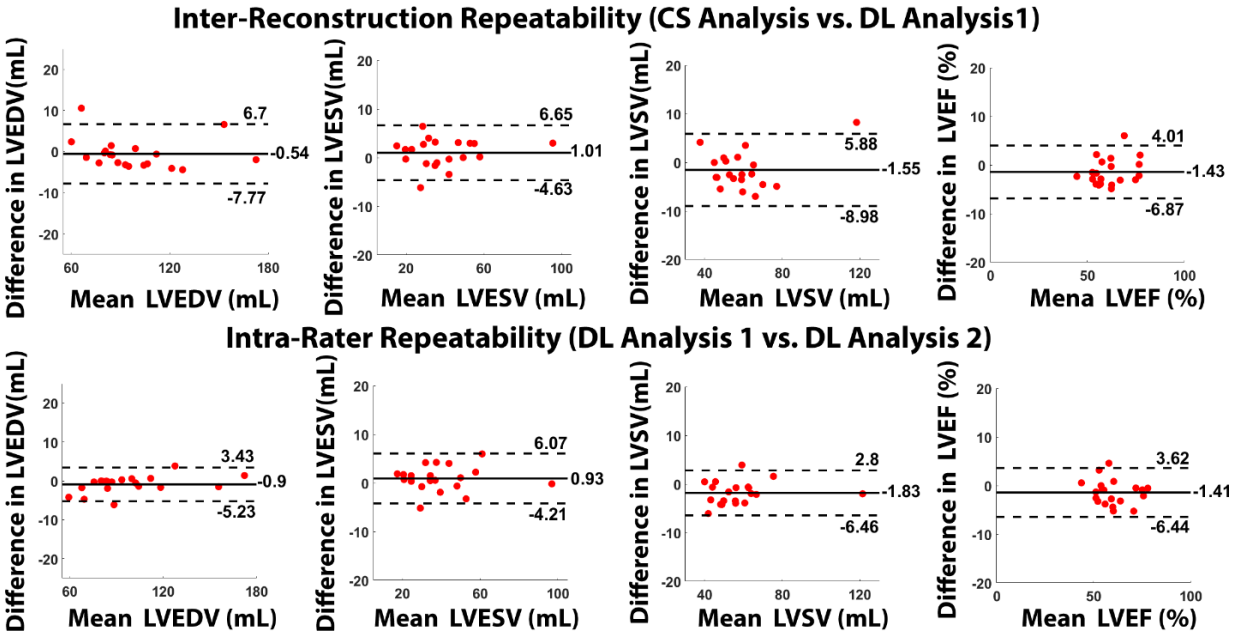

Figure 6.8. Bland-Altman plots illustrating good agreement between reconstruction methods (top row, CS vs. DL) and between repeated DL analyses (bottom row) for all four LV functional parameters.

6.4) Discussion

This study describes the implementation of a rapid DL reconstruction pipeline for faster (25 s per slice with 80 frames) reconstruction of non-Cartesian real-time cine complex data than GPU-accelerated CS (2:40 min per slice with 80 frames), without significant loss in image quality metrics (SSIM = 0. 88 ± 0.02, NRMSE = 0.014 ± 0.004), SVS, or LV functional parameters. By optimally learning different information contained in the real and imaginary parts of complex data and adding a perceptual loss term to suppress incoherent image features, the proposed PCNN outperformed other two architectures (magnitude with MSE loss term alone, complex network with MSE loss term alone) and successfully produced clinically acceptable image quality. Our engineering approach is based on MR physics, where the real and imaginary components contain

correlated and uncorrelated (noise) information detected using a quadrature radio-frequency receiver system. Therefore, learning image features in both real and imaginary components enables more faithful image reconstruction than magnitude learning only. While the MSE loss is commonly used in DL image reconstruction, it may produce perceptually incoherent image details. By taking the perceptual loss into account, our PCNN produced better image quality compared to complex network with MSE loss term alone.

This study compares and contrasts with prior proof-of-concept DL studies for reconstructing real-time cine MR data (54, 61) as follows. The study by Schlemper et al. (54) used a cascade of convolutional neural networks (CNN)s to train on retrospectively undersampled Cartesian k-space cine data derived from fully sampled raw k-space acquired during breath-holding. The strengths of this study are that it incorporated a k-space data fidelity term and maintained multi-coil information to ensure faithful reconstruction. This study, however, had the following limitations: (a) data from only 10 patients in total (5 for training and 5 for testing); (b) did not evaluate performance on non-Cartesian k-space data; (c) the network did not learn respiratory motion because training data were acquired during breath-holding; (d) achieved good results up to 9-fold acceleration. The study by Hauptmann et al. (61) used a residual U-Net to train on synthetically undersampled non-Cartesian k-space data derived from magnitude (i.e. Digital Imaging and Communications in Medicine [DICOM]) images acquired during breath-holding. The strength of this study is that testing was evaluated on zero-filled images derived from prospectively acquired 13-fold accelerated radial k-space data. This study, however, had the following limitations: (a) deriving synthetic radial undersampled k-space data from DICOM (magnitude) files is analytically incorrect, since the signal phase information is lost following the magnitude

operation; (b) the network did not learn respiratory motion because training data were obtained during breath-holding; (c) testing data from only 10 patients; (d) dealiasing performed on coil-combined, zero-filled magnitude images.

This study has several interesting points worth emphasizing. First, the proposed PCNN avoids complex value calculation that is not officially supported by Pytorch and minimizes loss of information when performing a magnitude operation to complex images. Our method provides an engineering solution to the current challenge of complex value optimization with CNNs. Second, both complex networks outperformed the magnitude network. This may be because of the fact that real and imaging components contain both correlated and uncorrelated (noise) image contents (Figure 1). Third, we used a GPU-based NUFFT in the pre-processing step to accelerate the gridding process. Despite best efforts, the pre-processing steps including gradient delay correction, gridding, and coil combination (23.7 s) was 29 times longer than the CNN filtering time (0.82 s). A future study is warranted to implement a more efficient NUFFT in Pytorch (https://github.com/mmuckley/torchkbnufft) to further reduce the pre-processing time. Fourth, the proposed PCNN pipeline produced clinically acceptable image quality, despite not having a k-space data fidelity term, by optimally learning both imaginary and real components and incorporating both MSE and perceptual loss terms. This is an efficient strategy for faithfully reconstructing non-Cartesian data, because performing NUFFT would undoubtedly slow down the processing. Fifth, while the blur metric appears to be better for zero-filled and complex network with MSE loss term only reconstructions, those scores were artificially boosted by substantial amount of streaking artifacts. Thus, the blur metric values for those two reconstructions need to be interpreted with caution. Sixth, we used the industry standard L2-loss to train our network. Several

studies have shown that L-1 loss may produce better results than L2-loss (142-144). A future study is warranted to compare the performance between L-1 vs. L-2 loss functions for training our data with PCNN. Seventh, PCNN was trained on CS as reference. As such, it was not designed to outperform CS in terms image quality, but to outperform CS in terms of computational speed.

This study has several limitations that warrant further discussion. First, we used CS reconstructed real-time cine images as practical ground truth, because it was not possible to obtain fully sampled data in patients with AF. On one hand, we do not have access to ground truth, so the best we can do is treat CS reconstructions as ground truth. On the other hand we have demonstrated a NN implementation that we can confidently say has successfully learned the CS algorithm, as verified by the results and analysis presented in this paper. Second, we did not incorporate a k-space data consistency term into our model because NUFFT and inverse-NUFFT are time consuming operations for non-Cartesian data. Another practical reason for not including a data consistency layer is GPU memory requirement, since such an operation would also necessitate multi-coil information. A future study is warranted to incorporate a data consistency layer for non-Cartesian data using a GPU server with very high memory capacity. Third, our training (multi-slice 2D+time) data were obtained from twenty patients. While the total number of patients may appear to be small, we used 31,840 2D images (or 1,173,749,760 voxels) and 2,547,072 parameters for PCNN for paired supervised learning with 3 x 3 x 3 kernels. Note, our training data size (twenty patients) is at least 4 times larger than the training data size (5 patients) used by Schlemper et al. (54). Fourth, while PCNN produced clinically acceptable visual scores for all four individual categories, its lowest score was temporal fidelity of myocardial wall motion. Subtle blurring of myocardial wall motion was visible in some slices, which may have contributed to small (1.4%)

underestimation in LVEF. Fifth, we designed PCNN based on a U-Net. It may be possible to achieve better results using more sophisticated unrolled network architectures (144, 145) with more powerful GPU and more training data, at the expense of greater computational demand and processing time. From a practical point of view, fast processing is essential for our clinical application, and access to a high-end GPU server with very high memory may be limited at most centers. Nonetheless, a future study is warranted to compare the performance between the proposed PCNN and more sophisticated networks.

In summary, this study describes implementation, training, and testing of an image reconstruction pipeline including a PCNN architecture for faster reconstruction of non-Cartesian real-time cine complex MR data than GPU-accelerated CS reconstruction, without significant loss in quantitative metrics of image quality, SVS, or LV functional parameters, thereby verifying clinical translatability.

Chapter 7: Deep Learning Based Automated Segmentation for Biventricular Tissue Phase Mapping

7.1) Introduction

While endomyocardial biopsy (EMB) is the gold standard method for monitoring patients after heart transplantations (HTx)(146), it is limited by invasiveness, operator dependency, sampling errors, high cost and difficulty in sampling the right ventricle (RV) free wall(147-149). In addition, EMB may cause serious side effects such as tricuspid regurgitation, cardiac perforation, pericardial tamponade, arrhythmias, heart block, and pneumothorax(147). A potential alternative to monitor grafts post HTx is tissue phase mapping (TPM), a 2D cine phase contrast MRI technique with three-directional velocity encoding which can quantify regional biventricular myocardial velocities(150). Recently, several studies have demonstrated significant differences in biventricular global and regional velocities in HTx patients (adult and pediatric) with and without transplant rejection (151, 152). However, most of these studies are limited to research and clinical translation is limited due to the labor-intensive manual segmentation of the myocardial contours at all the time points.

The black-blood prepared magnitude (anatomical) images derived from TPM have a relatively low contrast between the myocardium and the blood pool, especially in patients with HTx, due to interference from surgery-related artifacts. In addition, the low signal-to-noise-ratios (SNR) in TPM images makes it challenging to apply automated segmentation methods, especially for the RV which is much thinner when compared to the left ventricle (LV). Previously, several

attempts to automatically/semi-automatically segment the myocardium in TPM images were done (153-156).

In this study, we sought to develop a fully automated segmentation method for TPM images using deep learning (DL) and access its accuracy compared with manual analysis.

7.2) Methods

7.2.1) Patient Demographics

This study was conducted in accordance with protocols approved by our institutional review board and was Health Insurance Portability and Accountability Act (HIPAA) compliant. All subjects provided informed consent in writing. We retrospectively enrolled 99 patients with heart transplant (mean age = 50 ± 15 years; 55 males; 44 females). Each patient underwent 1-4 CMR scans for post HTx cardiac monitoring (median duration post HTx: 4.4 years; range: 6 days to 30 years), such that in total 150 scans were included. We used 114 scans (342 slices, 20-42 time frames per slice, 10,096 2D images) for training and 36 scans (108 slices, 23-36 time frames per slice, 3,288 2D images) for testing. A second independent observer (IO) manually analyzed 12 scans randomly selected from the 36 testing scans to evaluate inter-observer variability.

7.2.2) MRI Hardware

TPM scans were conducted on a 1.5T whole-body MRI scanner (MAGNETOM Aera or Avanto, Siemens Healthcare, Erlangen, Germany). The scanners were equipped with a gradient system capable of achieving a maximum gradient strength of 45 mT/m and maximum slew rate of 200 T/m/s. Body coil was used for radio-frequency excitation. Both body matrix and spine coil arrays (30-34 elements in total) were used for signal reception.

7.2.3) Pulse Sequence

TPM data were acquired for three short-axis slices at basal, mid-ventricular, and apical locations using a prospectively ECG-gated, black-blood prepared 2D phase-contrast sequence with three-directional velocity encoding (157-160) (VENC = 25 cm/s). Spatiotemporal imaging acceleration using Parallel MRI with Extended and Averaged GRAPPA Kernels (PEAK-GRAPPA) (161) with an undersampling factor of R = 5 permitted data acquisitions during breath-holding (breath-hold time = 24–28 heart beats per slice). Other relevant imaging parameters included: temporal resolution = 19-24 ms, in-plane spatial resolution = 2.0-2.3 mm^2, slice thickness = 8 mm, TE = 3.2-3.8 ms, TR = 4.8-6.1 ms, receiver bandwidth = 460-840 Hz/pixel, flip angle 10° or 15°.

7.2.4) Computer Hardware

For training and testing of the DL network, we used a GPU workstation (Tesla V100 32GB memory, NVIDIA, Santa Carla, California, USA; 32 Xeon E5-2620 v4 128 GB memory, Intel, Santa Clara, California, USA) equipped with Python (Version 3.7, Python Software Foundation), Pytorch (Version 1.4, Berkeley Software Distribution), and MATLAB (R2020b, The Mathworks Inc, Natick, MA, USA) running on a Linux operating system (Ubuntu16.04).

7.2.5) Image Processing

As shown in Figure 7.1, the manual contours from 3 clinic readers were transformed into multi-layer masks (i.e. labelled 0-3 for each pixel, 0: background, 1: blood pool, 2: RV myocardium, and 3: LV myocardium). We used the magnitude and three dimensional velocity (V_x, V_y, V_z) images as independent input channels (i.e. stacked in the channel dimension) and the multi-class masks as the reference. A 3D (2D + time) residual U-Net (Figure 7.2) was used to learn the

segmentation process, while 2D max pooling (2x2x1) was used to allow arbitrary number of time frames. Cross-entropy loss, multi-class dice loss (162) and Hausdorff distance (163) were used as the loss terms for training. For the dice loss, each class was calculated separately by Equation 7.1.

$$L_{DSC} = 1 - \frac{2\sum_i s_i r_i}{\sum_i s_i + \sum_i r_i} \quad \text{Eq. 7.1}$$

Where s_i is the DL segmentation result and r_i is the ground truth at each voxel i. The dice losses of all three classes (i.e. blood pool, LV myocardium and RV myocardium) are weighted equally. The Hausdorff distance is calculated for the boundary of the entire segmentation (i.e. three classes combined). The total loss for the training is described by Equation 7.2, where K is the total number of classes (i.e. 3) and L_{DSC_k} is the dice loss for class k.

$$L_{total} = L_{CE} + \frac{1}{K}\sum_{k=1}^{K} L_{DSC_k} + L_{HD} \quad \text{Eq. 7.2}$$

The network was trained on 342 2D+time sets of TPM images (114 scans, 342 slices, 20-42 time frames per slice), corresponding to 10,096 2D images in total. The trained network was then tested on the remaining 108 2D+time sets of TPM images, corresponding to 3,288 2D images in total.

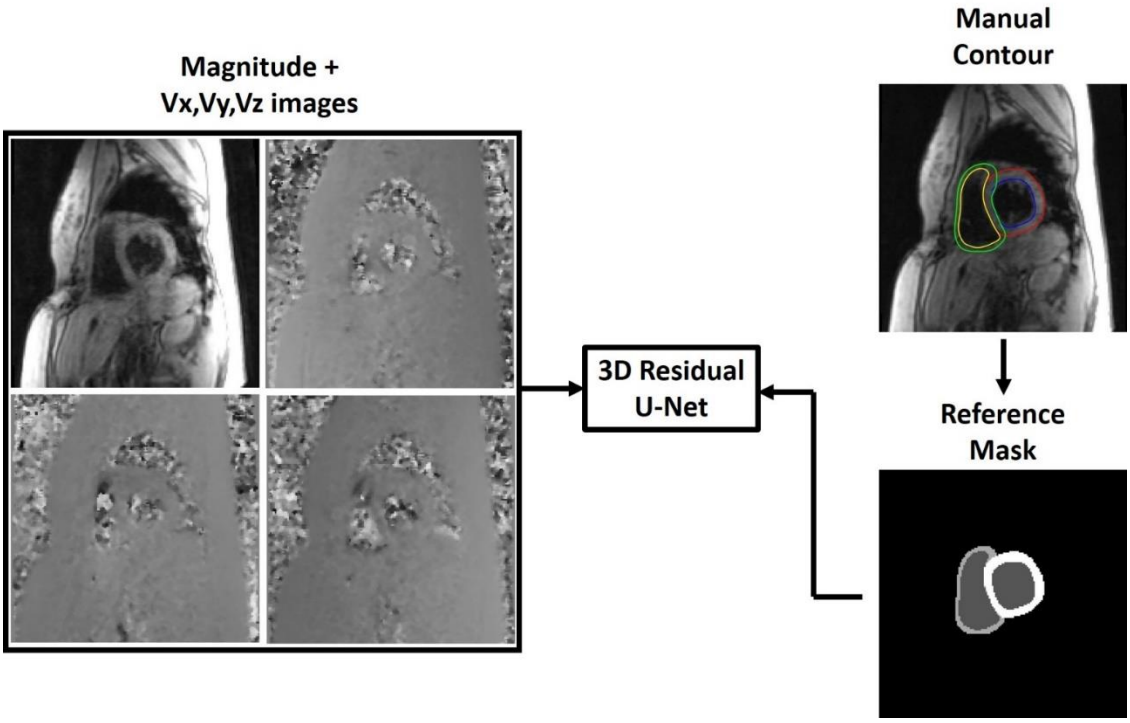

Figure 7.1. The manual contours were transformed into multi-layer masks (i.e. 0 for background, 1 for blood pool, 2 for RV myocardium and 3 for LV myocardium). We used the magnitude image and three dimensional velocity (V_x, V_y, V_z) images as independent input channels and the multi-class masks as the reference to train a 3D residual U-Net.

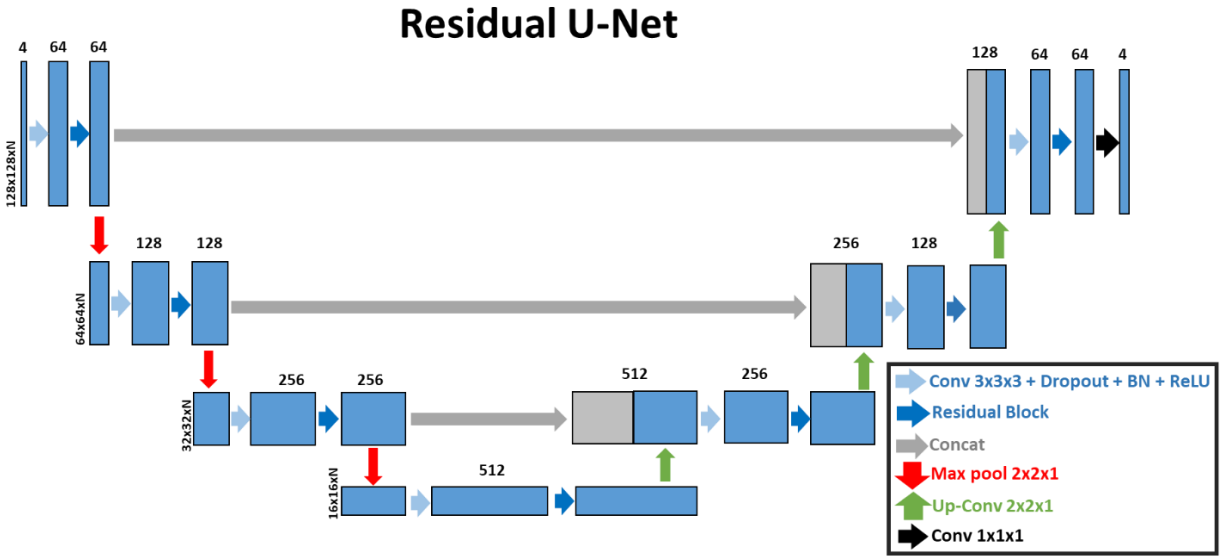

Figure 7.2. A 3D (2D + time) residual U-Net was used to learn the segmentation process, while max pooling (2x2x1) was used to allow arbitrary number (N) of time frames. Cross-entropy loss, multi-class dice-loss and Hausdorff distance were used as the loss terms for training.

7.2.6) Quantitative Analysis

To access segmentation accuracy of DL, we calculated the dice scores of LV and RV myocardium with manual contoured masks as reference. The Hausdorff distance is calculated for the entire heart segmentation to access the offsets of the boundaries. To get better understanding of the dice scores, we randomly selected 12 scans from the testing sets to evaluate inter-observer (IO) variability.

Myocardial velocity estimations were done using a custom home-developed software package (programmed in MATLAB, The Mathworks Inc, Natick, Mass). Manual segmentation involved using the magnitude images to set nodes at the epicardial and endocardial LV and RV borders at all time frames for all three short-axis slices. In a semi-automatic procedure, the manually set nodes were interpolated by splines to obtain smooth segmentation contours, which encloses the LV and RV myocardial tissue. The anterior and inferior LV-RV intersections were

automatically detected for all time frames and used to remove the septum from the RV masks. The DL-generated contours were converted into node coordinates and loaded onto the software. Using the same semi-automatic procedure, splines were generated and LV-RV intersection points were identified.

The velocity data was corrected for eddy currents(164) and bulk-motion(158, 159, 165) before velocity estimation. The Cartesian velocity (V_x and V_y) within the segmented LV and RV masks were converted into velocities along the three principal motion directions of the heart - radial shortening (V_r), tangential/circumferential shortening (V_ϕ), and longitudinal shortening (V_z). For simplicity, only the V_r and V_z are considered for further statistical analyses. End-systole was detected automatically as the time frame with the smallest endocardial LV volume and end-diastole as the time frame with the largest LV volume (summed over all three slices). The expanded 16+10 American Heart Association (AHA) model (Fig. Xc)(166) was used to report segmental end-systolic and end-diastolic peak velocities. Global LV and RV peak velocities were obtained by averaging the segmental values for each ventricle.

7.3) Results

The mean segmentation time was ~2 hours for manual and 1.9 ± 0.3 seconds per case for DL segmentation. As summarized in Table 7.1, the mean dice score for the LV and RV DL segmentations were 0.83 ± 0.07 and 0.59 ± 0.16, respectively for the entire testing set. The mean Hausdorff distance of the testing set is 3.84 ± 1.56. As shown in Table 7.2, for the 12 scans with manual IO analysis, the dice score of DL was significantly better than manual IO for LV (DL: 0.84 ± 0.07; manual IO: 0.78 ± 0.07; $p<0.001$), but was not significant different for RV (DL: 0.57 ±

0.16; manual IO: 0.56 ± 0.19; p=0.70). The Hausdorff distance was not significantly different between manual IO and DL (DL: 4.14 ± 1.75; manual IO: 3.95 ± 1.75; p=0.53).

	LV Dice Score	RV Dice Score	Hausdorff Distance
Basal	0.84 ± 0.08	0.66 ± 0.10	3.75 ± 1.35
Mid	0.84 ± 0.06	0.63 ± 0.14	3.61 ± 1.65
Apex	0.82 ± 0.08	0.46 ± 0.18	4.14 ± 1.65
Combined	0.83 ± 0.07	0.59 ± 0.17	3.84 ± 1.56

Table 7.1. Summary of quantitative metrics of 36 testing cases comparing deep learning segmentation versus manual references.

	LV Dice Score		RV Dice Score		Hausdorff Distance	
	DL	Manual IO	DL	Manual IO	DL	Manual IO
Basal	0.86 ± 0.06	0.80 ± 0.07	0.68 ± 0.11	0.67 ± 0.09	3.87 ± 1.71	3.48 ± 0.95
Mid	0.83 ± 0.08	0.78 ± 0.07	0.63 ± 0.12	0.62 ± 0.12	3.95 ± 1.97	3.48 ± 0.94
Apex	0.83 ± 0.06	0.76 ± 0.08	0.41 ± 0.12	0.40 ± 0.22	4.60 ± 1.61	4.88 ± 2.56
Combined	0.84 ± 0.07	0.78 ± 0.07	0.57 ± 0.16	0.56 ± 0.19	4.14 ± 1.75	3.95 ± 1.75
P-value	<0.001		0.70		0.53	

Table 7.2. Summary of quantitative metrics of 12 testing cases for manual independent observer (IO) comparison. Deep learning segmentation is compared with manual IO results, both using the same manual contour as reference.

Figure 7.3 shows four representative cases of TPM segmentation using manual contouring and deep learning. 2nd and 4th column from the left show the manual and DL contours, including:

LV epicardium (red), LV endocardium (blue), RV epicardium (green) and RV endocardium (yellow). 3rd and 5th column from the left show the multi-layer masks that are the reference (manual masks) and output (DL masks) of DL network.

Figure 7.4 shows scatter plots resulting from linear regression analysis illustrating strong correlation between manual and DL segmentation methods ($R \geq 0.88$) and between independent observers ($R \geq 0.89$) for peak radial (V_r) and longitudinal (V_z) myocardial velocities (LV and RV, systole and diastole). All 26 segments (AHA model) are plotted with the basal, mid-ventricular, and apical segments color-coded as red, blue and green, respectively. Figure 7.5 shows Bland-Altman plots illustrating good agreement between manual and DL segmentation for LV V_z (mean difference and limits of agreement [LOA] = -0.05 ± 0.98 cm/s); LV V_r (mean difference and LOA = -0.06 ± 1.18 cm/s); RV V_z (mean difference and LOA = -0.21 ± 2.33 cm/s); RV V_r (mean difference and LOA = 0.46 ± 4.00 cm/s). Figure 5 also shows good agreement between independent observers for LV V_z (mean difference and LOA = -0.07 ± 1.10 cm/s); LV V_r (mean difference and LOA = -0.13 ± 1.21 cm/s); RV V_z (mean difference and LOA = -0.32 ± 2.92 cm/s); RV V_r (mean difference and LOA = 0.47 ± 4.06 cm/s).

Figure 7.6 shows an example of time resolved radial (V_r) and longitudinal (V_z) velocity curves of LV and RV for manual and DL contours on the right and the corresponding velocity maps at systole and diastole time frame on the left. The red and blue vertical lines mark the time frames shown on the left, while the black and blue curves with dots represent manual and DL contours, respectively.

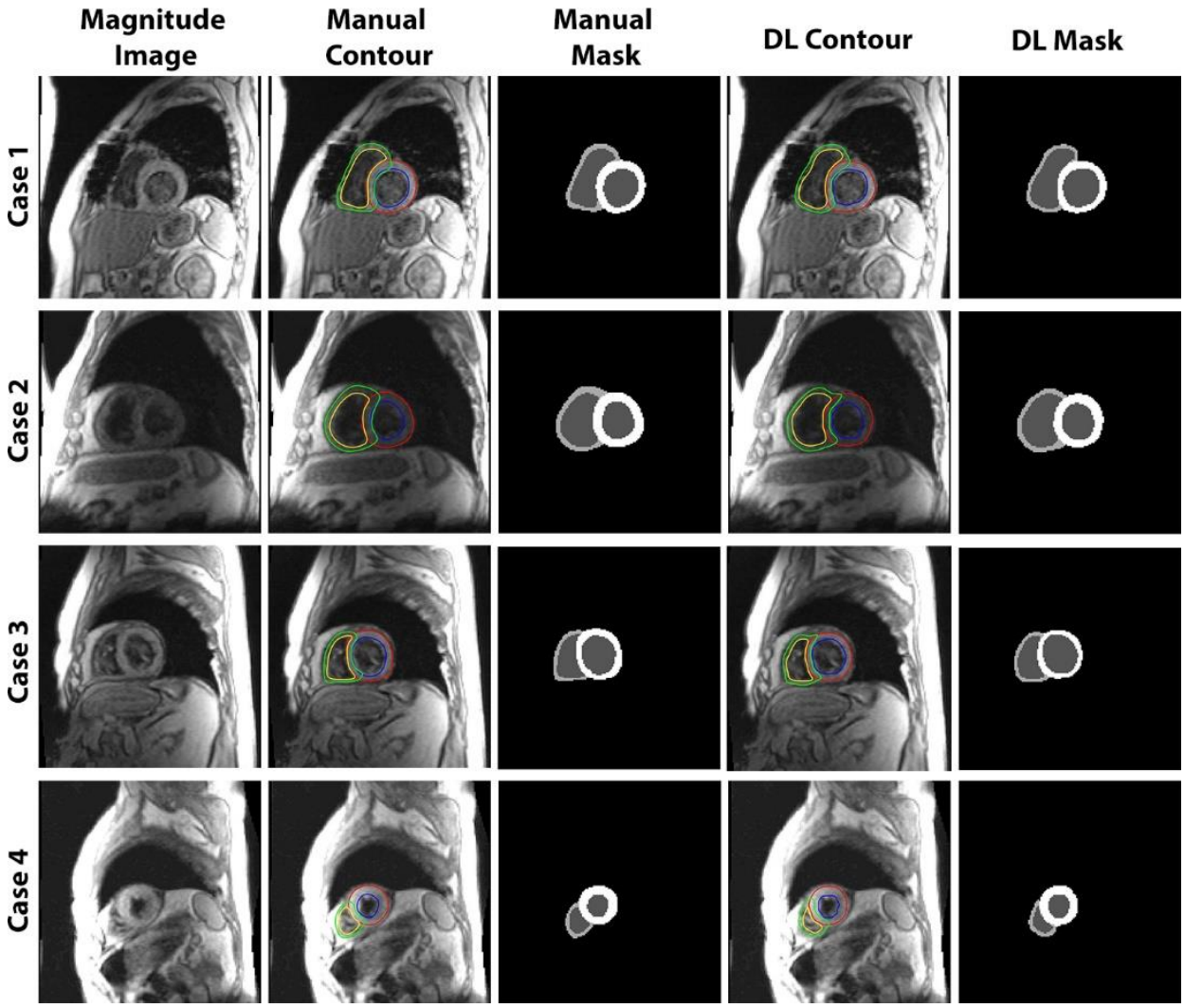

Figure 7.3. Four representative cases of TPM segmentation, manual versus deep learning. (Left column) Magnitude image as a part of the input to the network. (2^{nd} and 4^{th} column from the left) Manual and DL contours, including: LV epicardium (red), LV endocardium (blue), RV epicardium (green) and RV endocardium (yellow). (3^{rd} and 5^{th} column from the left) Multi-layer masks that are the reference (manual masks) and output (DL masks) of DL network.

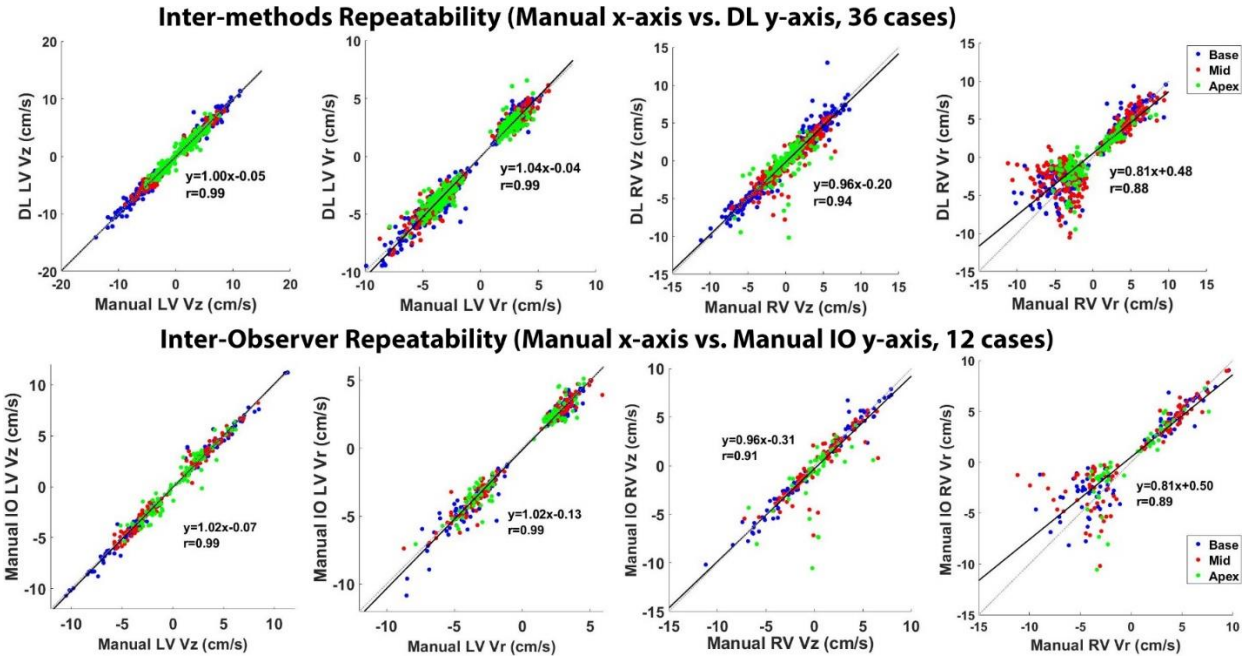

Figure 7.4. Linear regression plots illustrating strong correlation between segmentation methods (top row, manual vs. DL, 36 testing cases, $R \geq 0.88$) and between independent observers (bottom row, 12 manual IO cases, $R \geq 0.88$) for peak radial (Vr) and longitudinal (Vz) myocardial velocities (LV and RV, systole and diastole). All 26 segments are plotted with the basal, mid-ventricular, and apical segments color-coded as red, blue and green, respectively.

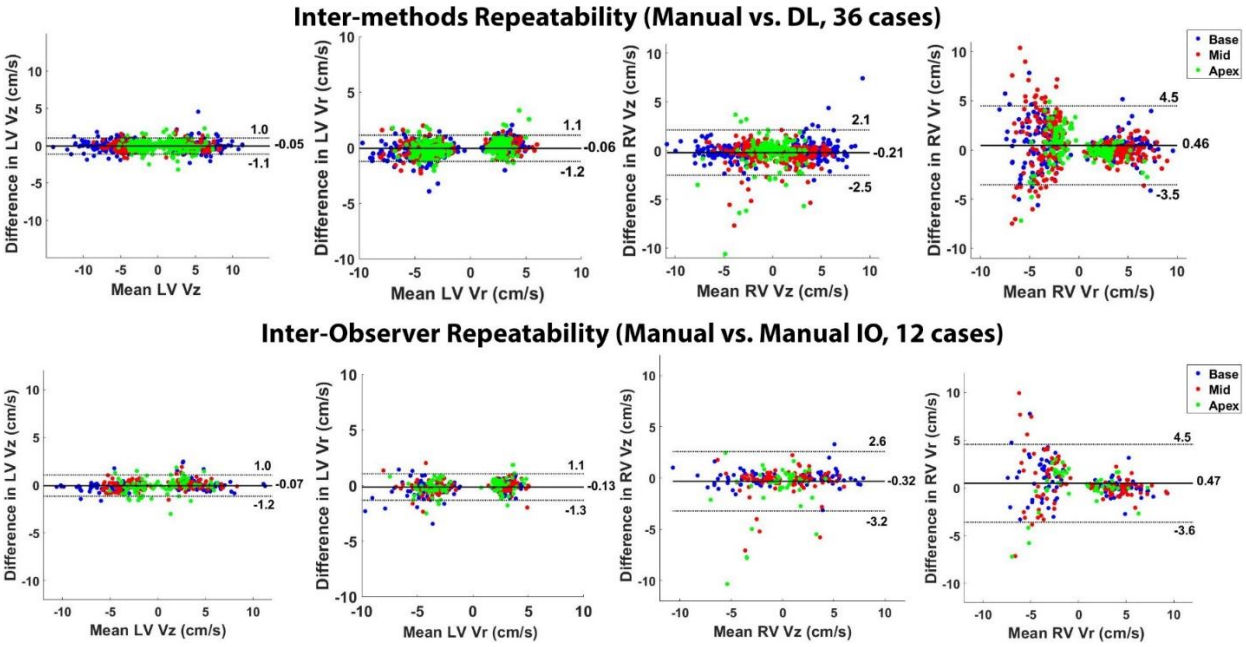

Figure 7.5. Bland-Altman plots illustrating good agreement between segmentation methods (top row, manual vs. DL, 36 testing cases) and between independent observers (bottom row, 12 manual IO cases) for peak radial (V_r) and longitudinal (V_z) myocardial velocities (LV and RV, systole and diastole). All 26 segments are plotted with the basal, mid-ventricular, and apical segments color-coded as red, blue and green, respectively.

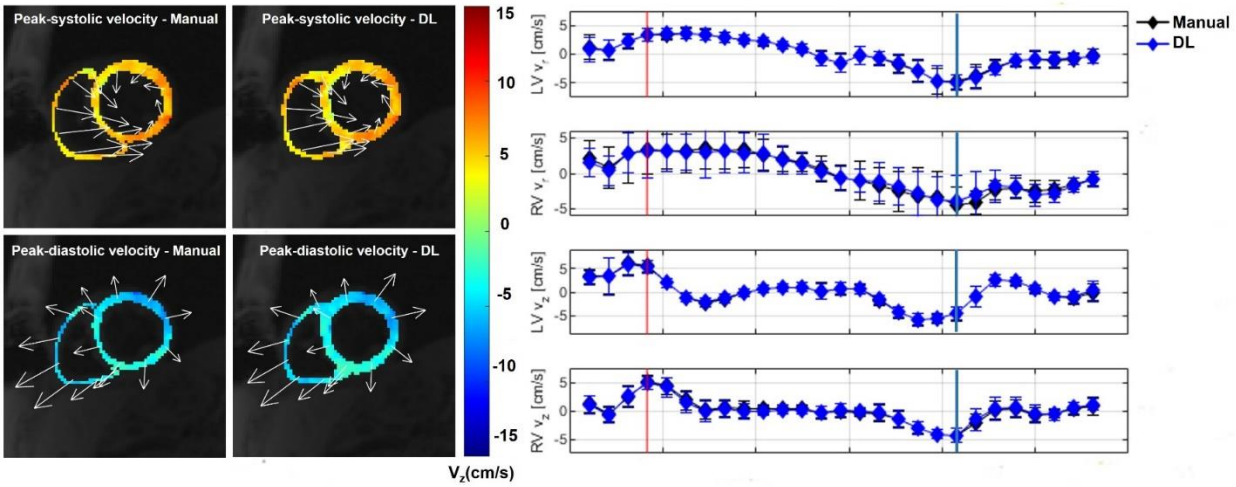

Figure 7.6. (Left) Biventricular velocity maps of manual and DL contours at systole and diastole time frame. Myocardial long-axis velocities are color-coded and in-plane velocities are depicted by regionally averaged velocity vectors. (Right) Time resolved radial (V_r) and longitudinal (V_z) velocity curves of LV and RV. The red and blue vertical lines represent the time frames shown on the left, while the black and blue curves with dots represent manual and DL contours, respectively.

7.4) Discussion

This study describes the implementation of an automated image segmentation method for TPM images using deep learning, which is significantly faster than manual segmentation, without significant loss in image segmentation accuracy (LV dice = 0.83 ± 0.07, RV dice = 0.59 ± 0.16, Hausdorff distance = 4.14 ± 1.75) or myocardial functional parameters (V_r and V_z). By utilizing magnitude and phase (V_x, V_y, V_z) images together, as well as incorporating cross-entropy loss, dice loss and Hausdorff distance into the loss function, the network was able to produce accurate segmentation comparable to manual contouring.

This study uses a subset of testing data for inter-observer comparison, which gives a better way of understanding the quantitative results. Note that the dice scores of DL segmentation is significantly better than manual IO for LV (DL: 0.84 ± 0.07; manual IO: 0.78 ± 0.07; $p<0.001$),

but is not significant different for RV (DL: 0.57 ± 0.16; manual IO: 0.56 ± 0.19; p=0.70). Even though higher dice scores don't necessarily indicate better segmentation (i.e. smooth edges, reasonable shapes), the DL segmentation results are still comparable to manual segmentation in general. For more accurate segmentation, DL results can be used as an initial guess, which can be further improved with minor manual adjustments. This semi-automated method can still largely reduce the amount of work for TPM segmentation.

This study has several limitations that warrant further discussion. First, the manual contours were drawn on images with higher spatial resolution (i.e. based on 1920x1080 screen resolution), while DL segmentation was done based on the DICOM image resolution (i.e. 2.0-2.3 mm^2). Therefore, the manual contours were smooth curves and DL contours had zigzagging curves. The intermedium steps of transferring contours to masks and transferring DL masks back to contours are limited by current CNN segmentation technique that performs image segmentation by labeling each voxel with certain class instead of drawing contour lines directly on image. Second, the DL segmentation results can be largely affected by the image quality (i.e. poor performance on cases with strong breathing motion artifacts), while manual contours always have reasonable LV and RV shapes. This is due to the fact that our DL method is purely image driven, while clinic attendees have the knowledge of how the heart should look like. It could be improved by incorporating model based learning in the future. Third, the performance of DL and manual IO is significantly worse on RV than LV, which could be due to: 1) RV myocardium is thinner than LV, which leads to lower SNR for RV; 2) susceptibility artifact caused by the heart transplant that is closer to RV; 3) epicardial fat signal makes it harder to determine RV boundary. A future study is warranted to improve the DL performance on RV.

In summary, this study describes an automated image segmentation method for biventricular tissue phase mapping images with deep learning that is significantly faster than manual contouring, without significant loss in quantitative metrics of segmentation accuracy and functional parameters, thereby verifying clinical translatability.

Chapter 8: Conclusion and Future Direction

8.1) Conclusion

While CMR is a promising non-invasive, versatile imaging modality capable of assessing cardiovascular function and anatomy without ionizing radiation, its utility in clinic is limited (~1%) due to long scan times. This dissertation describes the development and validation of several acceleration techniques that can potentially overcome this problem, thereby increase the utilization of CMR and lower the cost.

With current MRI scanner hardware, undersampling the k-space is a very effective way to accelerate CMR scans and enable real-time, free-breathing acquisitions. However, to undersample the data without losing image quality, advanced acceleration techniques such as compressed sensing and deep learning are needed. CS overcomes the Nyquist limit by exploring the sparsity in transform domains, which is essentially utilizing the knowledge about the data (i.e. we know it should be sparse). DL, on the other hand, is promising to overcome the long reconstruction time of CS, while CS images can be the practical ground truth reference for DL training. DL leverages the "common features" learned from large databases to predict the potential outcomes for new data, while the dependency on large amount of "ground truth" training data could limit its application.

This dissertation illustrated several studies that developed and validated acceleration methods using CS and DL on clinic data, including: 1) accelerate coronary QISS MRA with CS (Chapter 4); 2) explore the time dimension of LGE CMR with CS (Chapter 5); 3) accelerate image reconstruction of real-time cine MRI with DL (Chapter 6); 4) enable rapid, automated image

segmentation of TPM MRI with DL (Chapter 7). These studies showed the potential of accelerating CMR workflow with these techniques, which can potentially increase the overall CMR utility in clinic.

8.2) Future Directions

While this dissertation introduced the application of the acceleration techniques for clinic data, all the processes were done off-line. Future work must be done to further improve these methods and use in clinic. For instance, the CS reconstruction time of single-shot QISS MRA and multi-TI LGE CMR was too long for inline reconstruction (1~2 min per slice). Deep learning approach could be used to reduce the reconstruction time without significantly losing image quality. While it's challenging to acquire fully sampled reference images for DL training, transfer learning can be used to train the initial network and use the actual data to fine tuning the network. It can potentially reduce the amount of data needed for training to get reasonable outcomes.

The works presented in this dissertation covered accelerated acquisition, reconstruction and post-processing, but these methods are separated into different projects. Future works will include combining these methods into an inline pipeline that includes rapid pre-processing, image reconstruction and post-processing. Integrating these algorithms on platforms, such as Yarra and FIRE, will largely accelerate the overall processing time and help their clinic translation.

References

1. Virani SS, Alonso A, Benjamin EJ, Bittencourt MS, Callaway CW, Carson AP, et al. Heart Disease and Stroke Statistics-2020 Update: A Report From the American Heart Association. Circulation. 2020;141(9):e139-e596.
2. Dobrucki LW, Sinusas AJ. PET and SPECT in cardiovascular molecular imaging. Nature Reviews Cardiology. 2010;7(1):38.
3. Khalil MM, Tremoleda JL, Bayomy TB, Gsell W. Molecular SPECT imaging: an overview. International journal of molecular imaging. 2011;2011.
4. Verani MS, Taillefer R, Iskandrian AE, Mahmarian JJ, He ZX, Orlandi C. 123I-IPPA SPECT for the prediction of enhanced left ventricular function after coronary bypass graft surgery. Multicenter IPPA Viability Trial Investigators. 123I-iodophenylpentadecanoic acid. Journal of nuclear medicine : official publication, Society of Nuclear Medicine. 2000;41(8):1299-307.
5. Dilsizian V, Bateman TM, Bergmann SR, Des Prez R, Magram MY, Goodbody AE, et al. Metabolic imaging with beta-methyl-p-[(123)I]-iodophenyl-pentadecanoic acid identifies ischemic memory after demand ischemia. Circulation. 2005;112(14):2169-74.
6. Steeds RP. Echocardiography: frontier imaging in cardiology. The British journal of radiology. 2011;84 Spec No 3(Spec Iss 3):S237-45.
7. Poelma C. Ultrasound imaging velocimetry: a review. Experiments in Fluids. 2017;58(1):3.
8. Kadappu KK, Thomas L. Tissue Doppler imaging in echocardiography: value and limitations. Heart Lung Circ. 2015;24(3):224-33.
9. Oglat AA, Matjafri MZ, Suardi N, Oqlat MA, Abdelrahman MA, Oqlat AA. A Review of Medical Doppler Ultrasonography of Blood Flow in General and Especially in Common Carotid Artery. J Med Ultrasound. 2018;26(1):3-13.
10. Omoto R, YOKOTE Y, TAKAMOTO S, KYO S, UEDA K, ASANO H, et al. The development of real-time two-dimensional Doppler echocardiography and its clinical significance in acquired valvular diseases. Japanese heart journal. 1984;25(3):325-40.
11. Meinel FG, Nance JW, Jr., Harris BS, De Cecco CN, Costello P, Schoepf UJ. Radiation risks from cardiovascular imaging tests. Circulation. 2014;130(5):442-5.
12. Bonow RO. What's past is prologue: advances in cardiovascular imaging. The Lancet. 2012;379(9814):393-5.
13. Haji-Valizadeh H, Rahsepar AA, Collins JD, Bassett E, Isakova T, Block T, et al. Validation of highly accelerated real-time cardiac cine MRI with radial k-space sampling and compressed sensing in patients at 1.5 T and 3T. Magnetic resonance in medicine. 2018;79(5):2745-51.
14. Shen D, Edelman RR, Robinson JD, Haji-Valizadeh H, Messina M, Giri S, et al. Single-Shot Coronary Quiescent-Interval Slice-Selective Magnetic Resonance Angiography Using Compressed Sensing: A Feasibility Study in Patients With Congenital Heart Disease. Journal of computer assisted tomography. 2018;42(5):739-46.
15. Feng L, Otazo R, Jung H, Jensen JH, Ye JC, Sodickson DK, et al. Accelerated cardiac T2 mapping using breath-hold multiecho fast spin-echo pulse sequence with k-t FOCUSS. Magn Reson Med. 2011;65(6):1661-9.
16. Feng L, Srichai MB, Lim RP, Harrison A, King W, Adluru G, et al. Highly accelerated real-time cardiac cine MRI using k-t SPARSE-SENSE. Magn Reson Med. 2013;70(1):64-74.
17. Kim D, Dyvorne HA, Otazo R, Feng L, Sodickson DK, Lee VS. Accelerated phase-contrast cine MRI using k-t SPARSE-SENSE. Magn Reson Med. 2012;67(4):1054-64.
18. Otazo R, Kim D, Axel L, Sodickson DK. Combination of compressed sensing and parallel imaging for highly accelerated first-pass cardiac perfusion MRI. Magn Reson Med. 2010;64(3):767-76.
19. Bloch F. Nuclear Induction. Physical Review. 1946;70(7-8):460-74.

20. Purcell EM, Torrey HC, Pound RV. Resonance absorption by nuclear magnetic moments in a solid. Physical review. 1946;69(1-2):37.
21. Hahn EL. Nuclear Induction Due to Free Larmor Precession. Physical Review. 1950;77(2):297-8.
22. Hahn EL. Free nuclear induction. Physics Today. 1953;6(11):4-9.
23. Giri S, Chung Y-C, Merchant A, Mihai G, Rajagopalan S, Raman SV, et al. T2 quantification for improved detection of myocardial edema. Journal of cardiovascular magnetic resonance. 2009;11(1):56.
24. Abdul J. The Shannon Sampling Theorem—lts Various Extensions and Applications: A. Proceedings of the IEEE. 1977;65(11):1565.
25. Wright KL, Hamilton JI, Griswold MA, Gulani V, Seiberlich N. Non-Cartesian parallel imaging reconstruction. Journal of Magnetic Resonance Imaging. 2014;40(5):1022-40.
26. Glover GH, Pauly JM. Projection reconstruction techniques for reduction of motion effects in MRI. Magn Reson Med. 1992;28(2):275-89.
27. Fessler JA. On NUFFT-based gridding for non-Cartesian MRI. Journal of magnetic resonance (San Diego, Calif : 1997). 2007;188(2):191-5.
28. Qureshi M, Junaid M, Najam A, Bashir D, Ullah I, Kaleem M, et al. Image reconstruction using compressed sensing for individual and collective coil methods. 2016.
29. Peters DC, Derbyshire JA, McVeigh ER. Centering the projection reconstruction trajectory: reducing gradient delay errors. Magn Reson Med. 2003;50(1):1-6.
30. Wundrak S, Paul J, Ulrici J, Hell E, Geibel MA, Bernhardt P, et al. Golden ratio sparse MRI using tiny golden angles. Magnetic resonance in medicine. 2016;75(6):2372-8.
31. Tan H, Meyer CH. Estimation of k-space trajectories in spiral MRI. Magn Reson Med. 2009;61(6):1396-404.
32. Addy NO, Wu HH, Nishimura DG. Simple method for MR gradient system characterization and k-space trajectory estimation. Magn Reson Med. 2012;68(1):120-9.
33. Campbell-Washburn AE, Xue H, Lederman RJ, Faranesh AZ, Hansen MS. Real-time distortion correction of spiral and echo planar images using the gradient system impulse response function. Magn Reson Med. 2016;75(6):2278-85.
34. Deshmane A, Gulani V, Griswold MA, Seiberlich N. Parallel MR imaging. 2012;36(1):55-72.
35. Pruessmann KP, Weiger M, Scheidegger MB, Boesiger PJMrim. SENSE: sensitivity encoding for fast MRI. 1999;42(5):952-62.
36. Griswold MA, Jakob PM, Heidemann RM, Nittka M, Jellus V, Wang J, et al. Generalized autocalibrating partially parallel acquisitions (GRAPPA). Magn Reson Med. 2002;47(6):1202-10.
37. Lustig M, Donoho D, Pauly JM. Sparse MRI: The application of compressed sensing for rapid MR imaging. Magn Reson Med. 2007;58(6):1182-95.
38. Vasanawala S, Murphy M, Alley MT, Lai P, Keutzer K, Pauly JM, et al., editors. Practical parallel imaging compressed sensing MRI: Summary of two years of experience in accelerating body MRI of pediatric patients. 2011 ieee international symposium on biomedical imaging: From nano to macro; 2011: IEEE.
39. Block KT, Uecker M, Frahm J. Undersampled radial MRI with multiple coils. Iterative image reconstruction using a total variation constraint. Magnetic Resonance in Medicine: An Official Journal of the International Society for Magnetic Resonance in Medicine. 2007;57(6):1086-98.
40. Feng L, Grimm R, Block KT, Chandarana H, Kim S, Xu J, et al. Golden-angle radial sparse parallel MRI: combination of compressed sensing, parallel imaging, and golden-angle radial sampling for fast and flexible dynamic volumetric MRI. Magn Reson Med. 2014;72(3):707-17.
41. Adluru G, Awate SP, Tasdizen T, Whitaker RT, DiBella EV. Temporally constrained reconstruction of dynamic cardiac perfusion MRI. Magnetic Resonance in Medicine: An Official Journal of the International Society for Magnetic Resonance in Medicine. 2007;57(6):1027-36.

42. Haji-Valizadeh H, Collins JD, Aouad PJ, Serhal AM, Lindley MD, Pang J, et al. Accelerated, free-breathing, noncontrast, electrocardiograph-triggered, thoracic MR angiography with stack-of-stars k-space sampling and GRASP reconstruction. Magnetic resonance in medicine. 2019;81(1):524-32.
43. Bengio Y, Courville A, Vincent P. Representation learning: a review and new perspectives. IEEE transactions on pattern analysis and machine intelligence. 2013;35(8):1798-828.
44. Schmidhuber J. Deep learning in neural networks: an overview. Neural networks : the official journal of the International Neural Network Society. 2015;61:85-117.
45. LeCun Y, Bengio Y, Hinton G. Deep learning. Nature. 2015;521(7553):436-44.
46. Ngo TA, Lu Z, Carneiro G. Combining deep learning and level set for the automated segmentation of the left ventricle of the heart from cardiac cine magnetic resonance. Med Image Anal. 2017;35:159-71.
47. Suk HI, Lee SW, Shen D, Alzheimer's Disease Neuroimaging I. Hierarchical feature representation and multimodal fusion with deep learning for AD/MCI diagnosis. Neuroimage. 2014;101:569-82.
48. Doherty JU, Kort S, Mehran R, Schoenhagen P, Soman P, Dehmer GJ, et al. ACC/AATS/AHA/ASE/ASNC/HRS/SCAI/SCCT/SCMR/STS 2019 Appropriate Use Criteria for Multimodality Imaging in the Assessment of Cardiac Structure and Function in Nonvalvular Heart Disease: A Report of the American College of Cardiology Appropriate Use Criteria Task Force, American Association for Thoracic Surgery, American Heart Association, American Society of Echocardiography, American Society of Nuclear Cardiology, Heart Rhythm Society, Society for Cardiovascular Angiography and Interventions, Society of Cardiovascular Computed Tomography, Society for Cardiovascular Magnetic Resonance, and the Society of Thoracic Surgeons. Journal of the American College of Cardiology. 2019;73(4):488-516.
49. Benkert T, Tian Y, Huang C, DiBella EVR, Chandarana H, Feng L. Optimization and validation of accelerated golden-angle radial sparse MRI reconstruction with self-calibrating GRAPPA operator gridding. Magnetic resonance in medicine. 2018;80(1):286-93.
50. Yang G, Yu S, Dong H, Slabaugh G, Dragotti PL, Ye X, et al. DAGAN: Deep De-Aliasing Generative Adversarial Networks for Fast Compressed Sensing MRI Reconstruction. IEEE Trans Med Imaging. 2018;37(6):1310-21.
51. Guo Y, Liu Y, Oerlemans A, Lao S, Wu S, Lew MS. Deep learning for visual understanding: A review. Neurocomputing. 2016;187:27-48.
52. Ronneberger O, Fischer P, Brox T, editors. U-net: Convolutional networks for biomedical image segmentation. International Conference on Medical image computing and computer-assisted intervention; 2015: Springer.
53. Goodfellow I, Pouget-Abadie J, Mirza M, Xu B, Warde-Farley D, Ozair S, et al., editors. Generative adversarial nets. Advances in neural information processing systems; 2014.
54. Schlemper J, Caballero J, Hajnal JV, Price AN, Rueckert D. A Deep Cascade of Convolutional Neural Networks for Dynamic MR Image Reconstruction. IEEE Trans Med Imaging. 2018;37(2):491-503.
55. Glockner JF, Vrtiska TJJAi. Renal MR and CT angiography: current concepts. 2007;32(3):407-20.
56. Lustig M, Pauly JM. SPIRiT: Iterative self-consistent parallel imaging reconstruction from arbitrary k-space. Magnetic resonance in medicine. 2010;64(2):457-71.
57. Ma LE, Markl M, Chow K, Huh H, Forman C, Vali A, et al. Aortic 4D flow MRI in 2 minutes using compressed sensing, respiratory controlled adaptive k-space reordering, and inline reconstruction. Magnetic resonance in medicine. 2019;81(6):3675-90.
58. Feng L, Axel L, Chandarana H, Block KT, Sodickson DK, Otazo R. XD-GRASP: Golden-angle radial MRI with reconstruction of extra motion-state dimensions using compressed sensing. Magnetic resonance in medicine. 2016;75(2):775-88.
59. Bassett EC, Kholmovski EG, Wilson BD, DiBella EV, Dosdall DJ, Ranjan R, et al. Evaluation of highly accelerated real-time cardiac cine MRI in tachycardia. NMR in biomedicine. 2014;27(2):175-82.

60. Nam S, Basha T, Stehning M, Manning W, Tarokh V, Nezafat R. A GPU implementation of compressed sensing reconstruction of 3D radial (kooshball) acquisition for high-resolution cardiac MRI. Proc of the ISMRM, May 2011. 2011:2548.
61. Hauptmann A, Arridge S, Lucka F, Muthurangu V, Steeden JA. Real-time cardiovascular MR with spatio-temporal artifact suppression using deep learning-proof of concept in congenital heart disease. Magn Reson Med. 2019;81(2):1143-56.
62. Han Y, Yoo J, Kim HH, Shin HJ, Sung K, Ye JC. Deep learning with domain adaptation for accelerated projection-reconstruction MR. Magn Reson Med. 2018;80(3):1189-205.
63. Hoffman JI, Kaplan S. The incidence of congenital heart disease. J Am Coll Cardiol. 2002;39(12):1890-900.
64. Reller MD, Strickland MJ, Riehle-Colarusso T, Mahle WT, Correa A. Prevalence of congenital heart defects in metropolitan Atlanta, 1998-2005. The Journal of pediatrics. 2008;153(6):807-13.
65. Wernovsky G, Mayer JE, Jr., Jonas RA, Hanley FL, Blackstone EH, Kirklin JW, et al. Factors influencing early and late outcome of the arterial switch operation for transposition of the great arteries. The Journal of thoracic and cardiovascular surgery. 1995;109(2):289-301; discussion -2.
66. Turley K, Verrier ED. Intermediate results from the period of the Congenital Heart Surgeons Transposition Study: 1985 to 1989. Congenital Heart Surgeons Society Database. The Annals of thoracic surgery. 1995;60(3):505-10.
67. Geva T KJ. Diagnostic pathways for evaluation of congenital heart disease. In: Crawford MH DJ, editor. Cardiology. London, England: Mosby; 2001. p. 7-41.
68. Meinel FG, Nance JW, Harris BS, De Cecco CN, Costello P, Schoepf UJ. Radiation Risks From Cardiovascular Imaging Tests. Circulation. 2014;130(5):442-5.
69. Hasebroock KM, Serkova NJ. Toxicity of MRI and CT contrast agents. Expert opinion on drug metabolism & toxicology. 2009;5(4):403-16.
70. McDonald RJ, McDonald JS, Kallmes DF, Jentoft ME, Murray DL, Thielen KR, et al. Intracranial Gadolinium Deposition after Contrast-enhanced MR Imaging. Radiology. 2015;275(3):772-82.
71. Kanal E, Tweedle MF. Residual or retained gadolinium: practical implications for radiologists and our patients. Radiology. 2015;275(3):630-4.
72. Kanda T, Ishii K, Kawaguchi H, Kitajima K, Takenaka D. High signal intensity in the dentate nucleus and globus pallidus on unenhanced T1-weighted MR images: relationship with increasing cumulative dose of a gadolinium-based contrast material. Radiology. 2014;270(3):834-41.
73. Malayeri AA, Brooks KM, Bryant LH, Evers R, Kumar P, Reich DS, et al. National Institutes of Health Perspective on Reports of Gadolinium Deposition in the Brain. J Am Coll Radiol. 2016.
74. Marckmann P, Skov L, Rossen K, Dupont A, Damholt MB, Heaf JG, et al. Nephrogenic systemic fibrosis: suspected causative role of gadodiamide used for contrast-enhanced magnetic resonance imaging. Journal of the American Society of Nephrology : JASN. 2006;17(9):2359-62.
75. Miller JH, Hu HH, Pokorney A, Cornejo P, Towbin R. MRI Brain Signal Intensity Changes of a Child During the Course of 35 Gadolinium Contrast Examinations. Pediatrics. 2015;136(6):e1637-40.
76. Roberts DR, Holden KR. Progressive increase of T1 signal intensity in the dentate nucleus and globus pallidus on unenhanced T1-weighted MR images in the pediatric brain exposed to multiple doses of gadolinium contrast. Brain & development. 2016;38(3):331-6.
77. Gulani V, Calamante F, Shellock FG, Kanal E, Reeder SB. Gadolinium deposition in the brain: summary of evidence and recommendations. The Lancet Neurology.16(7):564-70.
78. Miyazaki M, Lee VS. Nonenhanced MR angiography. Radiology. 2008;248(1):20-43.
79. Kim WY, Danias PG, Stuber M, Flamm SD, Plein S, Nagel E, et al. Coronary Magnetic Resonance Angiography for the Detection of Coronary Stenoses. New England Journal of Medicine. 2001;345(26):1863-9.

80. Srichai MB, Kim S, Axel L, Babb J, Hecht EM. Non-gadolinium-enhanced 3-dimensional magnetic resonance angiography for the evaluation of thoracic aortic disease: a preliminary experience. Tex Heart Inst J. 2010;37(1):58.
81. François CJ, Tuite D, Deshpande V, Jerecic R, Weale P, Carr JC. Unenhanced MR angiography of the thoracic aorta: initial clinical evaluation. American Journal of Roentgenology. 2008;190(4):902-6.
82. Amano Y, Takahama K, Kumita S. Non–contrast-enhanced MR angiography of the thoracic aorta using cardiac and navigator-gated magnetization-prepared three-dimensional steady-state free precession. Journal of Magnetic Resonance Imaging. 2008;27(3):504-9.
83. Okada T, Kanao S, Kuhara S, Ninomiya A, Fujimoto K, Kido A, et al. Whole-heart coronary MR angiography under a single breath-hold: a comparative study with respiratory-gated acquisition using a multi-element phased-array coil. Clinical radiology. 2011;66(11):1060-3.
84. Edelman RR, Giri S, Pursnani A, Botelho MPF, Li W, Koktzoglou I. Breath-hold imaging of the coronary arteries using Quiescent-Interval Slice-Selective (QISS) magnetic resonance angiography: pilot study at 1.5 Tesla and 3 Tesla. Journal of Cardiovascular Magnetic Resonance. 2015;17:101.
85. Lustig M, Donoho D, Pauly JM. Sparse MRI: The application of compressed sensing for rapid MR imaging. Magnetic Resonance in Medicine. 2007;58(6):1182-95.
86. Payne GS, Leach MO. Implementation and evaluation of frequency offset corrected inversion (FOCI) pulses on a clinical MR system. Magn Reson Med. 1997;38(5):828-33.
87. Dutt A, Rokhlin V. Fast Fourier-Transforms for Nonequispaced Data. Siam Journal on Scientific Computing. 1993;14(6):1368-93.
88. Griswold MA WD, Heidemann RM, Haase A, Jakob PM. The use of an adaptive reconstruction for array coil sensitivity mapping and intensity normalization. In Proceedings of the 10th Annual Meeting of ISMRM, Honolulu, Hawaii, USA,. 2002:2410.
89. Walsh DO, Gmitro AF, Marcellin MW. Adaptive reconstruction of phased array MR imagery. Magn Reson Med. 2000;43(5):682-90.
90. Zhou W, Bovik AC, Sheikh HR, Simoncelli EP. Image quality assessment: from error visibility to structural similarity. IEEE Transactions on Image Processing. 2004;13(4):600-12.
91. Dietrich O, Raya JG, Reeder SB, Reiser MF, Schoenberg SO. Measurement of signal-to-noise ratios in MR images: influence of multichannel coils, parallel imaging, and reconstruction filters. Journal of magnetic resonance imaging : JMRI. 2007;26(2):375-85.
92. Adluru G, DiBella E. Compression2: compressed sensing with compressed coil arrays. Journal of cardiovascular magnetic resonance : official journal of the Society for Cardiovascular Magnetic Resonance. 2012;14(Suppl 1):P242.
93. Goldstein T, Osher S. The Split Bregman Method for L1-Regularized Problems. SIAM J Img Sci. 2009;2(2):323-43.
94. Adluru G, Tasdizen T, Whitaker R, DiBella E, editors. Improving Undersampled MRI Reconstruction Using Non-Local Means. Internat Conf on Pattern Recognition (ICPR); 2010; Istanbul, Turkey
95. Akcakaya M, Basha TA, Goddu B, Goepfert LA, Kissinger KV, Tarokh V, et al. Low-dimensional-structure self-learning and thresholding: regularization beyond compressed sensing for MRI reconstruction. Magn Reson Med. 2011;66(3):756-67.
96. Akcakaya M, Rayatzadeh H, Basha TA, Hong SN, Chan RH, Kissinger KV, et al. Accelerated late gadolinium enhancement cardiac MR imaging with isotropic spatial resolution using compressed sensing: initial experience. Radiology. 2012;264(3):691-9.
97. Jevtovic-Todorovic V, Absalom AR, Blomgren K, Brambrink A, Crosby G, Culley DJ, et al. Anaesthetic neurotoxicity and neuroplasticity: an expert group report and statement based on the BJA Salzburg Seminar. British journal of anaesthesia. 2013;111(2):143-51.
98. FDA. US Food & Drug Administration 2016 [

99. Moussavi A, Untenberger M, Uecker M, Frahm J. Correction of gradient-induced phase errors in radial MRI. Magnetic resonance in medicine : official journal of the Society of Magnetic Resonance in Medicine / Society of Magnetic Resonance in Medicine. 2014;71(1):308-12.
100. Deshmane A, Blaimer M, Breuer F, Jakob P, Duerk J, Seiberlich N, et al. Self-calibrated trajectory estimation and signal correction method for robust radial imaging using GRAPPA operator gridding. Magnetic resonance in medicine : official journal of the Society of Magnetic Resonance in Medicine / Society of Magnetic Resonance in Medicine. 2016;75(2):883-96.
101. Etienne A, Botnar RM, Van Muiswinkel AM, Boesiger P, Manning WJ, Stuber M. "Soap-Bubble" visualization and quantitative analysis of 3D coronary magnetic resonance angiograms. Magnetic resonance in medicine : official journal of the Society of Magnetic Resonance in Medicine / Society of Magnetic Resonance in Medicine. 2002;48(4):658-66.
102. Kim RJ, Fieno DS, Parrish TB, Harris K, Chen EL, Simonetti O, et al. Relationship of MRI delayed contrast enhancement to irreversible injury, infarct age, and contractile function. Circulation. 1999;100(19):1992-2002.
103. Kim RJ, Wu E, Rafael A, Chen EL, Parker MA, Simonetti O, et al. The use of contrast-enhanced magnetic resonance imaging to identify reversible myocardial dysfunction. N Engl J Med. 2000;343(20):1445-53.
104. Simonetti OP, Kim RJ, Fieno DS, Hillenbrand HB, Wu E, Bundy JM, et al. An improved MR imaging technique for the visualization of myocardial infarction. Radiology. 2001;218(1):215-23.
105. Kellman P, Larson AC, Hsu LY, Chung YC, Simonetti OP, McVeigh ER, et al. Motion-corrected free-breathing delayed enhancement imaging of myocardial infarction. Magn Reson Med. 2005;53(1):194-200.
106. Song HK, Dougherty L. k-space weighted image contrast (KWIC) for contrast manipulation in projection reconstruction MRI. Magn Reson Med. 2000;44(6):825-32.
107. Haji-Valizadeh H, Rahsepar AA, Collins JD, Bassett E, Isakova T, Block T, et al. Validation of highly accelerated real-time cardiac cine MRI with radial k-space sampling and compressed sensing in patients at 1.5T and 3T. Magnetic resonance in medicine : official journal of the Society of Magnetic Resonance in Medicine / Society of Magnetic Resonance in Medicine. 2018;79(5):2745-51.
108. Messroghli DR, Moon JC, Ferreira VM, Grosse-Wortmann L, He T, Kellman P, et al. Clinical recommendations for cardiovascular magnetic resonance mapping of T1, T2, T2* and extracellular volume: A consensus statement by the Society for Cardiovascular Magnetic Resonance (SCMR) endorsed by the European Association for Cardiovascular Imaging (EACVI). Journal of cardiovascular magnetic resonance : official journal of the Society for Cardiovascular Magnetic Resonance. 2017;19(1):75.
109. Wundrak S, Paul J, Ulrici J, Hell E, Rasche V. A Small Surrogate for the Golden Angle in Time-Resolved Radial MRI Based on Generalized Fibonacci Sequences. IEEE transactions on medical imaging. 2015;34(6):1262-9.
110. Nacif MS, Turkbey EB, Gai N, Nazarian S, van der Geest RJ, Noureldin RA, et al. Myocardial T1 mapping with MRI: comparison of look-locker and MOLLI sequences. Journal of magnetic resonance imaging : JMRI. 2011;34(6):1367-73.
111. Feng L, Wen Q, Huang C, Tong A, Liu F, Chandarana H. GRASP-Pro: imProving GRASP DCE-MRI through self-calibrating subspace-modeling and contrast phase automation. Magn Reson Med. 2020;83(1):94-108.
112. Huang F, Vijayakumar S, Li Y, Hertel S, Duensing GR. A software channel compression technique for faster reconstruction with many channels. Magnetic resonance imaging. 2008;26(1):133-41.
113. Knoll F, Schwarzl A, Diwoky C, Sodickson DK. gpuNUFFT-an open source GPU library for 3D regridding with direct Matlab interface. In: Proceedings of the 22rd Annual Meeting of ISMRM, Melbourne, Australia 2014. Abstract No. 4297.
114. Rosenzweig S, Holme HCM, Uecker M. Simple auto-calibrated gradient delay estimation from few spokes using Radial Intersections (RING). Magn Reson Med. 2019;81(3):1898-906.

115. Neumann D, Breuer FA, Völker M, Brandt T, Griswold MA, Jakob PM, et al. Reducing contrast contamination in radial turbo-spin-echo acquisitions by combining a narrow-band KWIC filter with parallel imaging. Magn Reson Med. 2014;72(6):1680-6.
116. Crete F, Dolmiere T, Ladret P, Nicolas M. The blur effect: perception and estimation with a new no-reference perceptual blur metric: SPIE; 2007.
117. Flett AS, Hasleton J, Cook C, Hausenloy D, Quarta G, Ariti C, et al. Evaluation of techniques for the quantification of myocardial scar of differing etiology using cardiac magnetic resonance. JACC Cardiovascular imaging. 2011;4(2):150-6.
118. Bahrami N, Retson T, Blansit K, Wang K, Hsiao A. Automated selection of myocardial inversion time with a convolutional neural network: Spatial temporal ensemble myocardium inversion network (STEMI-NET). Magn Reson Med. 2019;81(5):3283-91.
119. American College of Cardiology Foundation Task Force on Expert Consensus D, Hundley WG, Bluemke DA, Finn JP, Flamm SD, Fogel MA, et al. ACCF/ACR/AHA/NASCI/SCMR 2010 expert consensus document on cardiovascular magnetic resonance: a report of the American College of Cardiology Foundation Task Force on Expert Consensus Documents. J Am Coll Cardiol. 2010;55(23):2614-62.
120. Grothues F, Smith GC, Moon JC, Bellenger NG, Collins P, Klein HU, et al. Comparison of interstudy reproducibility of cardiovascular magnetic resonance with two-dimensional echocardiography in normal subjects and in patients with heart failure or left ventricular hypertrophy. The American journal of cardiology. 2002;90(1):29-34.
121. Voit D, Zhang S, Unterberg-Buchwald C, Sohns JM, Lotz J, Frahm J. Real-time cardiovascular magnetic resonance at 1.5 T using balanced SSFP and 40 ms resolution. Journal of cardiovascular magnetic resonance : official journal of the Society for Cardiovascular Magnetic Resonance. 2013;15:79.
122. Adler J, Oktem O. Solving ill-posed inverse problems using iterative deep neural networks. Inverse Problems. 2017;33(12).
123. Lucas A, Iliadis M, Molina R, Katsaggelos AK. Using Deep Neural Networks for Inverse Problems in Imaging Beyond analytical methods. Ieee Signal Processing Magazine. 2018;35(1):20-36.
124. Ongie G, Jalal A, Metzler CA, Baraniuk RG, Dimakis AG, Willett R. Deep Learning Techniques for Inverse Problems in Imaging. IEEE Journal on Selected Areas in Information Theory. 2020;1(1):39-56.
125. Zhu B, Liu JZ, Cauley SF, Rosen BR, Rosen MS. Image reconstruction by domain-transform manifold learning. Nature. 2018;555(7697):487-92.
126. Bora A, Jalal A, Price E, Dimakis AG. Compressed sensing using generative models. Proceedings of the 34th International Conference on Machine Learning - Volume 70; Sydney, NSW, Australia: JMLR.org; 2017. p. 537–46.
127. Maier AK, Syben C, Stimpel B, Wurfl T, Hoffmann M, Schebesch F, et al. Learning with Known Operators reduces Maximum Training Error Bounds. Nat Mach Intell. 2019;1(8):373-80.
128. Gilton D, Ongie G, Willett R. Neumann Networks for Linear Inverse Problems in Imaging. Ieee T Comput Imag. 2020;6:328-43.
129. Haji-Valizadeh H, Shen D, Avery RJ, Serhal AM, Schiffers FA, Katsaggelos AK, et al. Rapid Reconstruction of Four-dimensional MR Angiography of the Thoracic Aorta Using a Convolutional Neural Network. Radiol Cardiothorac Imaging. 2020;2(3):e190205.
130. Fan L, Shen D, Haji-Valizadeh H, Naresh NK, Carr JC, Freed BH, et al. Rapid dealiasing of undersampled, non-Cartesian cardiac perfusion images using U-net. NMR in biomedicine. 2020;n/a(n/a):e4239.
131. Johnson J, Alahi A, Fei-Fei L, editors. Perceptual Losses for Real-Time Style Transfer and Super-Resolution2016; Cham: Springer International Publishing.
132. Lee D, Yoo J, Tak S, Ye JC. Deep Residual Learning for Accelerated MRI Using Magnitude and Phase Networks. IEEE transactions on bio-medical engineering. 2018;65(9):1985-95.
133. Han Y, Sunwoo L, Ye JC. k-Space Deep Learning for Accelerated MRI. IEEE transactions on medical imaging. 2019.

134. Hyun CM, Kim HP, Lee SM, Lee S, Seo JK. Deep learning for undersampled MRI reconstruction. Physics in medicine and biology. 2018;63(13):135007.
135. Kyong Hwan J, McCann MT, Froustey E, Unser M. Deep Convolutional Neural Network for Inverse Problems in Imaging. IEEE transactions on image processing : a publication of the IEEE Signal Processing Society. 2017;26(9):4509-22.
136. Eo T, Jun Y, Kim T, Jang J, Lee HJ, Hwang D. KIKI-net: cross-domain convolutional neural networks for reconstructing undersampled magnetic resonance images. Magnetic resonance in medicine : official journal of the Society of Magnetic Resonance in Medicine / Society of Magnetic Resonance in Medicine. 2018;80(5):2188-201.
137. Chaudhari AS, Fang Z, Kogan F, Wood J, Stevens KJ, Gibbons EK, et al. Super-resolution musculoskeletal MRI using deep learning. Magnetic resonance in medicine : official journal of the Society of Magnetic Resonance in Medicine / Society of Magnetic Resonance in Medicine. 2018;80(5):2139-54.
138. Johnson J, Alahi A, Fei-Fei L, editors. Perceptual losses for real-time style transfer and super-resolution. European conference on computer vision; 2016: Springer.
139. Simonyan K, Zisserman A. Very Deep Convolutional Networks for Large-Scale Image Recognition. CoRR. 2015;abs/1409.1556.
140. Trabelsi C, Bilaniuk O, Zhang Y, Serdyuk D, Subramanian S, Santos JF, et al. Deep complex networks. arXiv preprint arXiv:170509792. 2017.
141. Wang Z, Bovik AC, Sheikh HR, Simoncelli EP. Image quality assessment: from error visibility to structural similarity. IEEE transactions on image processing : a publication of the IEEE Signal Processing Society. 2004;13(4):600-12.
142. Zhao H, Gallo O, Frosio I, Kautz J. Loss Functions for Image Restoration With Neural Networks. Ieee T Comput Imag. 2017;3(1):47-57.
143. Lim B, Son S, Kim H, Nah S, Lee KM, editors. Enhanced Deep Residual Networks for Single Image Super-Resolution. 2017 IEEE Conference on Computer Vision and Pattern Recognition Workshops (CVPRW); 2017 21-26 July 2017.
144. Mardani M, Gong E, Cheng JY, Vasanawala SS, Zaharchuk G, Xing L, et al. Deep Generative Adversarial Neural Networks for Compressive Sensing MRI. IEEE transactions on medical imaging. 2019;38(1):167-79.
145. Lonning K, Putzky P, Sonke JJ, Reneman L, Caan MWA, Welling M. Recurrent inference machines for reconstructing heterogeneous MRI data. Medical image analysis. 2019;53:64-78.
146. Costanzo MR, Dipchand A, Starling R, Anderson A, Chan M, Desai S, et al. The International Society of Heart and Lung Transplantation Guidelines for the care of heart transplant recipients. The Journal of heart and lung transplantation : the official publication of the International Society for Heart Transplantation. 2010;29(8):914-56.
147. From AM, Maleszewski JJ, Rihal CS. Current status of endomyocardial biopsy. Mayo Clinic proceedings. 2011;86(11):1095-102.
148. Lampert BC, Teuteberg JJ, Shullo MA, Holtz J, Smith KJ. Cost-effectiveness of routine surveillance endomyocardial biopsy after 12 months post-heart transplantation. Circulation Heart failure. 2014;7(5):807-13.
149. Shah KB, Flattery MP, Smallfield MC, Merinar G, Tang DG, Sheldon EH, et al. Surveillance Endomyocardial Biopsy in the Modern Era Produces Low Diagnostic Yield for Cardiac Allograft Rejection. Transplantation. 2015;99(8):e75-80.
150. Menza M, Föll D, Hennig J, Jung B. Segmental biventricular analysis of myocardial function using high temporal and spatial resolution tissue phase mapping. Magnetic Resonance Materials in Physics, Biology and Medicine. 2018;31(1):61-73.
151. Sarnari R, Blake AM, Ruh A, Abbasi MA, Pathrose A, Blaisdell J, et al. Evaluating Biventricular Myocardial Velocity and Interventricular Dyssynchrony in Adult Patients During the First Year After Heart Transplantation. J Magn Reson Imaging. 2020.

152. Berhane H, Ruh A, Husain N, Robinson JD, Rigsby CK, Markl M. Myocardial velocity, intra-, and interventricular dyssynchrony evaluated by tissue phase mapping in pediatric heart transplant recipients. Journal of Magnetic Resonance Imaging. 2020;51(4):1212-22.
153. Zhu Y, Pelc NJ. A spatiotemporal model of cyclic kinematics and its application to analyzing nonrigid motion with MR velocity images. IEEE Trans Med Imaging. 1999;18(7):557-69.
154. Bergvall E, Cain P, Arheden H, Sparr G. A fast and highly automated approach to myocardial motion analysis using phase contrast magnetic resonance imaging. J Magn Reson Imaging. 2006;23(5):652-61.
155. Cho J, Benkeser PJ. Cardiac segmentation by a velocity-aided active contour model. Computerized Medical Imaging and Graphics. 2006;30(1):31-41.
156. Meyer FG, Constable RT, Sinusas AJ, Duncan JS. Tracking myocardial deformation using phase contrast MR velocity fields: a stochastic approach. IEEE Transactions on Medical Imaging. 1996;15(4):453-65.
157. Ruh A, Sarnari R, Berhane H, Sidoryk K, Lin K, Dolan R, et al. Impact of age and cardiac disease on regional left and right ventricular myocardial motion in healthy controls and patients with repaired tetralogy of fallot. Int J Cardiovasc Imaging. 2019;35(6):1119-32.
158. Hennig J, Schneider B, Peschl S, Markl M, Krause T, Laubenberger J. Analysis of myocardial motion based on velocity measurements with a black blood prepared segmented gradient-echo sequence: methodology and applications to normal volunteers and patients. J Magn Reson Imaging. 1998;8(4):868-77.
159. Jung B, Föll D, Böttler P, Petersen S, Hennig J, Markl M. Detailed analysis of myocardial motion in volunteers and patients using high-temporal-resolution MR tissue phase mapping. Journal of Magnetic Resonance Imaging: An Official Journal of the International Society for Magnetic Resonance in Medicine. 2006;24(5):1033-9.
160. Markl M, Rustogi R, Galizia M, Goyal A, Collins J, Usman A, et al. Myocardial T2-mapping and velocity mapping: changes in regional left ventricular structure and function after heart transplantation. Magn Reson Med. 2013;70(2):517-26.
161. Bauer S, Markl M, Föll D, Russe M, Stankovic Z, Jung B. K-t GRAPPA accelerated phase contrast MRI: Improved assessment of blood flow and 3-directional myocardial motion during breath-hold. J Magn Reson Imaging. 2013;38(5):1054-62.
162. Shen C, Roth HR, Oda H, Oda M, Hayashi Y, Misawa K, et al. On the influence of Dice loss function in multi-class organ segmentation of abdominal CT using 3D fully convolutional networks. arXiv preprint arXiv:180105912. 2018.
163. Karimi D, Salcudean SE. Reducing the Hausdorff Distance in Medical Image Segmentation With Convolutional Neural Networks. IEEE Trans Med Imaging. 2020;39(2):499-513.
164. Walker PG, Cranney GB, Scheidegger MB, Waseleski G, Pohost GM, Yoganathan AP. Semiautomated method for noise reduction and background phase error correction in MR phase velocity data. J Magn Reson Imaging. 1993;3(3):521-30.
165. Markl M, Schneider B, Hennig J. Fast phase contrast cardiac magnetic resonance imaging: Improved assessment and analysis of left ventricular wall motion. Journal of Magnetic Resonance Imaging. 2002;15(6):642-53.
166. Cerqueira MD, Weissman NJ, Dilsizian V, Jacobs AK, Kaul S, Laskey WK, et al. Standardized Myocardial Segmentation and Nomenclature for Tomographic Imaging of the Heart. Circulation. 2002;105(4):539-42.